Sigrid Wolf, BSc.

Mixed MnO_2/$NiCo_2O_4$ as Bifunctional Oxygen Catalyst for Secondary Zinc/Air Batteries

MASTER'S THESIS

to achieve the university degree of

Diplom-Ingenieurin

Master's degree programme: Technical Chemistry

submitted to

Graz University of Technology

Supervisor

Ass. Prof. Dipl.-Ing. Dr. techn. Waltraud Taucher-Mautner

Institute for Chemistry and Technology of Materials

Graz, November 2018

AFFIDAVIT

I declare that I have authored this thesis independently, that I have not used other than the declared sources/resources, and that I have explicitly indicated all material which has been quoted either literally or by content from the sources used. The text document uploaded to TUGRAZonline is identical to the present master‘s thesis.

11th November 2018

Date

Sigrid Wolf

Signature

Acknowledgements

Firstly, I would like to express my sincere gratitude to my advisor Waltraud Taucher-Mautner for all the support and encouragement she gave me during my master's thesis. She consistently allowed this work to be my own work, but whenever I ran into a trouble spot or had a question about my research or writing, the door of her office was open and she steered me in the right direction. Thank you for this great experience!

Furthermore, I would like to thank Bernhard Gollas for his help. Extended discussions and valuable suggestions have contributed greatly to the improvement of my thesis. Also, I like to thank Brigitte Bitschnau and Franz Mautner for the XRD measurements and data analysis. My sincere thanks also go to Birgit Krenn, Sandra Steiner, Verena Theußl, Verena Maier-Mohamed, Christian Zelger, Daniel Schloffer, Richard Hueber, Wei Yang and David Moser. Thank you for your great support, your constant advice and for all the fun we have had in the last year!

Special thanks are due to my family and my boyfriend Sebastian, who supported me throughout all ups and downs during my whole studies. Thank you for giving me the opportunity to go my way. I will be grateful forever for your love.

Last but not least, thanks to my friends and everyone, who made this section of my life so great!

Zusammenfassung

Zink-Luft Batterien haben aufgrund ihrer geringen Toxizität, geringen Kosten und Umweltfreundlichkeit in den letzten Jahren großes Interesse geweckt. Im Hinblick auf ihre kurze Lebensdauer muss an ihrer Entwicklung jedoch noch gearbeitet werden. Ein Grund dafür ist die hohe Überspannung zwischen der Sauerstoffentwicklungs- (OER) und Sauerstoffreduktionsreaktion (ORR) der bifunktionellen Luftelektrode. Manganoxide zeigen eine vielversprechende elektrokatalytische Aktivität für die ORR in alkalischen Medien, aber die Aktivität für die OER ist gering. Unter den mehr als dreißig verschiedenen MnO_2-Kristallstrukturen gilt die α-Phase als die aktivste. Im Gegensatz zum Manganoxid gilt der $NiCo_2O_4$-Spinell als effektiver Katalysator für die Sauerstoffentwicklung. Für die Entwicklung eines vielversprechenden, bifunktionellen Katalysators wurde in dieser Masterarbeit erstmals α-MnO_2 und $NiCo_2O_4$ in verschiedenen Verhältnissen kombiniert.

Als $NiCo_2O_4$ wurde eine Probe aus früheren Arbeiten verwendet. Für die Synthese von α-MnO_2 wurde elektrolytisches Mangandioxid (EMD) erhitzt, um Mn_2O_3 zu erzeugen. Zwei unterschiedliche Mengen an Mn_2O_3 wurden für einen Säureaufschluss (6 M H_2SO_4) verwendet, wobei eine bestimmte Temperatur und Säurekonzentration für die Bildung der α-MnO_2 Phase wichtig sind. Die physikalisch-chemischen Eigenschaften der Manganoxide wurden anhand von XRD, REM/EDX und BET-Messungen analysiert. Die elektrochemische Charakterisierung der reinen und gemischten Katalysatoren in 0.1 M und 8 M Kalilauge erfolgte mittels zyklischer Voltammetrie, OER und ORR Experimenten. Die Messungen wurden mit Hilfe einer rotierenden Scheibenelektrode, welche mit einer Katalysatorschicht bedeckt ist, durchgeführt.

Die XRD-Analyse zeigt phasenreine Mn_2O_3 und α-MnO_2 Produkte und eine Mischung aus γ-MnO_2 und ε-MnO_2 für EMD. Die REM-Bilder des EMD zeigen viel feinere Partikel nach dem Mahlen. Im Vergleich zum porösen EMD, hat Mn_2O_3 eine riffartige Morphologie. Die α-MnO_2 Pulver werden als Nanostäbchen charakterisiert. Die EDX-Messungen bestätigen das Vorhandensein von Mangan und Sauerstoff und zeigen einen kleinen Anteil an Schwefel, welcher auf die Katalysatorherstellung zurückzuführen ist. Die spezifische Oberfläche der α-MnO_2 Proben ist größer als die von Mn_2O_3 und EMD und stimmt gut mit der Literatur überein. Anhand der zyklischen Voltammogramme konnten verschiedene Oxidations- und Reduktionspeaks von

Mangan, Nickel und Kobalt festgestellt werden. Die Ergebnisse der OER zeigen eine geringere Überspannung in 8 M als in 0.1 M Kalilauge. Außerdem zeigen die gemischten Katalysatoren eine verbesserte Aktivität im Vergleich zu den einzelnen Katalysatoren. Die Grenzstromdichten für die ORR in 0.1 M KOH sind aufgrund der höheren Sauerstofflöslichkeit höher als in 8 M KOH. Auch wenn die Kombination von α-MnO_2 mit $NiCo_2O_4$ in 0.1 M Kalilauge zu leicht niedrigeren Grenzstromdichten und etwas höheren Überspannungen als das reine α-MnO_2 führt, wird die elektrokatalytische Aktivität im Vergleich zum reinen $NiCo_2O_4$ stark erhöht. In 8 M Kalilauge sind die α-MnO_2 Katalysatoren sehr unstabil und zeigen somit leicht niedrigere Grenzstromdichten und eine viel höhere Überspannung als der $NiCo_2O_4$-Spinell. Durch das Mischen von α-MnO_2 und $NiCo_2O_4$ entstehen stabilere Katalysatoren. Die Überspannung ist zwar fast gleich hoch als jene des reinen α-MnO_2, die Grenzstromdichte ist jedoch viel höher im Vergleich zu den reinen Katalysatoren.

Abstract

Zinc-air batteries gained a lot of interest in the last few years due to their low toxicity, low cost and environmental friendliness. However, they still need a lot of development due to their short cycle life. One reason for this is the large overpotential between the oxygen evolution reaction (OER) and the oxygen reduction reaction (ORR) of the bifunctional air electrode. Manganese oxides show promising electrocatalytic performance for ORR in alkaline media, but the activity for OER is moderate. Among over thirty different MnO_2 crystal structures, the α-phase is the most active one. In contrast to manganese oxide, the $NiCo_2O_4$ spinel is considered to be an effective catalyst for OER. In this master`s thesis α-MnO_2 and $NiCo_2O_4$ were combined for the first time in different ratios to develop a promising bifunctional catalyst.

A $NiCo_2O_4$ sample synthesized in a prior work was used. For the preparation of α-MnO_2, electrolytic manganese dioxide (EMD) was heat-treated to obtain Mn_2O_3. Two different amounts of Mn_2O_3 were used for acid digestion (6 M H_2SO_4) at a certain temperature. The physicochemical properties of the manganese oxides were analysed by XRD, SEM/EDX and BET measurements. For the electrochemical characterisation of the pure and mixed catalysts, cyclic voltammetry, OER and ORR experiments were

carried out. The measurements were performed in 0.1 M and 8 M KOH using a rotating disc working electrode (RDE) that is covered with the catalyst.

XRD analysis shows phase-pure Mn_2O_3 and α-MnO_2 samples and a mixture of γ-MnO_2 and ε-MnO_2 for EMD. The SEM images of EMD demonstrate much smaller particles after milling. Mn_2O_3 has a reef-like morphology compared to the porous EMD. The α-MnO_2 powders can be categorized as nanorods. EDX measurements confirmed the presence of manganese and oxygen and a small amount of sulphur that is due to sample synthesis. The specific surface area of the α-MnO_2 samples is higher than that of Mn_2O_3 and EMD and is in good agreement with literature. The cyclic voltammograms show various oxidation and reduction peaks of manganese, nickel and cobalt. Considering the OER results, the catalysts exhibit lower overpotential in 8 M KOH than in 0.1 M KOH. The mixed samples show improved performances compared to the individual catalysts. For the ORR, the catalysts indicate higher current densities in 0.1 M than in 8 M KOH due to higher solubility of oxygen in diluted electrolyte. Even though the combination of α-MnO_2 with $NiCo_2O_4$ in 0.1 M KOH leads to slightly decreased current densities and higher overpotentials compared to the pure α-MnO_2, it significantly increases the electrocatalytic activity in comparison to the pure $NiCo_2O_4$. In 8 M KOH, the α-MnO_2 catalysts are quite unstable resulting in a slightly lower limiting current density and a significantly higher overpotential compared to $NiCo_2O_4$. Mixing α-MnO_2 and $NiCo_2O_4$ leads to more stable catalysts. The overpotential is nearly as high as that of α-MnO_2, but the limiting current density is significantly enhanced compared to both individual catalysts.

Table of contents

1 Introduction

The growth in world population and the change of the consumer habits in the twenty-first century are the two most important reasons for a dramatic increase in energy demand projected to be even doubled in the following fifteen years. Energy is needed in quite all situations of life and therefore, it is currently one of the most important topics. The outcome of this is drastic pollution of the environment and a dramatic increase of greenhouse emissions in the atmosphere, due to usage of fossil fuels like coal, oil or natural gas, which are quite limited. The substitution of such energy sources by renewables like wind or solar radiation will be needed. However, this alternative “green” electricity is heavily influenced by the variety of weather conditions and the need of energy consistently fluctuates. In order to save extra power and to release a high amount in a short time when it is required, a reliable, efficient, safe and inexpensive energy storage system will be needed for a stable energy grid [1–9].

In general, four different types of energy storage systems are known: mechanical, electrical, electrochemical and chemical. They show variable advantages and disadvantages adjusted according to the application [3]. Electrochemical energy storage brings advantages of high efficiency, versatility and its ability to be scaled down to small sizes [4][8]. Metal-air batteries, especially zinc-air batteries, have numerous advantages in comparison to common rechargeable batteries such as lead-acid and lithium-ion batteries. They have less battery weight, because the positive reactant can be taken from the air and present a relatively high theoretical energy density [3][5][10]. In addition, zinc is a safe material, can be fully recycled, features low pollution and is available throughout the world, what makes this battery system very cheap and environmentally friendly [1][2]. Zinc-air batteries normally consist of four main parts, the positive air electrode with a bifunctional catalyst, the negative zinc electrode, a separator and an alkaline electrolyte [8]. They can be divided into two main types, the primary and electrically rechargeable (secondary) battery. Primary batteries have been investigated for many years presenting good results [5]. Although secondary zinc-air batteries provide many advantages, they still need further development in terms of their short cycle life mainly related to dendritic growth at the zinc electrode, carbonation of the electrolyte and performance of the bifunctional air electrode [4][9]. One reason for this is the large overpotential (ΔV) between the oxygen evolution reaction (OER) and the oxygen reduction reaction (ORR) at the bifunctional air electrode [11]. These reactions are quite inhibited and therefore, it is necessary to find a bifunctional catalyst, which is able to accelerate both reactions. Platinum shows very good catalyst activities for ORR, but it is a poor catalyst for OER. Additionally, high cost and scarcity limit its application. As alternative, transition metals like cobalt oxides or manganese oxides have been investigated. Manganese oxides show promising electrocatalytic performances for OER and ORR under alkaline conditions. Additionally, they have many other advantages like abundance in natural ores, low toxicity, low cost and environmental friendliness [12]. The performance of manganese oxide catalysts depends on a lot of different factors. It has been reported that α-MnO_2 is the most active one [13].

The aim of this master's thesis is the synthesis and combination of two different α-MnO_2 samples, based on the best working catalyst for OER and ORR in literature [14], with a $NiCo_2O_4$ spinel. Manganese dioxide is combined in different ratios with a $NiCo_2O_4$ sample synthesized in prior studies via hydroxide precipitation method [15]. The electrochemical properties of the mixed samples as bifunctional catalysts for OER and ORR in secondary zinc-air batteries are examined. The precursor for the α-MnO_2 synthesis is electrolytic manganese dioxide (EMD) that is reduced to Mn_2O_3 by heating it up to 700 °C. In an acid digestion process, two different amounts of Mn_2O_3 are added to a sulphuric acid solution. The ratio of H^+ to Mn_2O_3 is varied and therefore, two different α-MnO_2 samples are prepared. For the electrochemical characterisation of the catalysts, voltammetry experiments (cyclic voltammetry, oxygen evolution reaction and oxygen reduction reaction) are carried out. They are operated in a three-electrode cell at room temperature. The working electrode is a rotating disc electrode (RDE), the counter electrode is a platinum net and an Hg/HgO reference electrode is used. The measurements were performed in 0.1 M and 8 M potassium hydroxide electrolyte solution. X-ray powder diffraction (XRD), scanning electron microscopy (SEM), energy dispersive X-ray spectroscopy (EDX) and Brunauer-Emmett-Teller (BET) method are used to analyse the structure, morphology, chemical composition and specific surface area of the different manganese oxides.

2 Theory

2.1 Metal-air battery

In general, two main battery types can be classified, the primary or non-rechargeable and the secondary or rechargeable battery. Secondary batteries can be further subcategorized as electrically or mechanically rechargeable. The electrically rechargeable battery systems are preferred due to their lower total price [2]. Nowadays, the most important and frequently used secondary batteries are lithium-ion batteries, because of their long cycle life (>5000 cycles) and high energy efficiency (>90%). However, such systems are still limited in their performance due to relatively low theoretical energy densities (410 Wh kg^{-1}) compared to ordinary gasoline (13000 Wh kg^{-1}) [3][6][16]. A comparison of the theoretical energy density of different battery types and gasoline is shown in Figure 1. Other disadvantages like high cost, low safety and limiting supply of lithium and cobalt make it urgent to find an alternative battery system [4]. In this field of research, metal-air batteries are promising candidates since they provide relatively high theoretical energy densities 3-30 times higher compared to lithium-ion batteries, because of the positive air reactant that can be stored outside until use [17]. Metal-air batteries are a combination of conventional batteries and fuel cells and generally consist of a metal anode, an air-breathing cathode, an electrolyte and a separator placed in the middle. According to the electrolyte, metal-air batteries can be divided into two main groups: aqueous and non-aqueous [18]. Electricity is generated as a result of redox processes between the anode metal and the oxygen taken from the air. In particular, the metal anode is oxidized and generates electrons that are released to the external circuit and they are further used to reduce oxygen to hydroxide ions. In an overall reaction, metal oxide is formed [19]. Many different anode metals like Mg, K, Li, Zn, Ca, Fe or Al can be used. Among these, lithium-air batteries provide the highest theoretical energy density (11700 Wh kg^{-1}) comparable to the one of gasoline (13000 Wh kg^{-1}). However, lithium brings a lot of disadvantages like the sensitivity to moisture. In comparison, magnesium- or aluminium-air batteries can be operated in aqueous electrolyte and indicate theoretical current densities comparable to lithium-air batteries but they also show disadvantages like rapid self-discharge and poor coulombic charging efficiency due to their low reduction potentials. In contrast, zinc is much more stable and shows high activity in aqueous electrolyte solution. Furthermore, zinc is a safe, inexpensive, environmentally friendly and a moisture stable material, which is available throughout the world. In addition, zinc-air batteries show a satisfactory high theoretical energy density (1350 Wh kg^{-1}) [2–4][16–18][20].

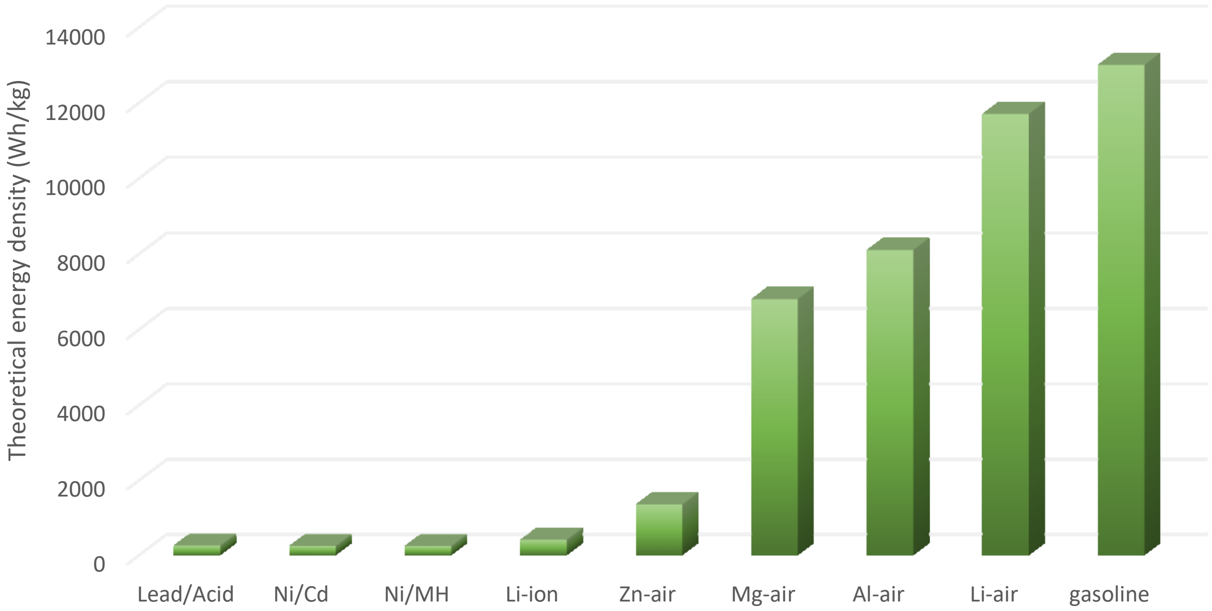

Figure 1: Comparison of theoretical energy density of different battery types and gasoline.

2.2 Zinc-air battery

Secondary zinc-air batteries consist of four main parts including the negative zinc electrode, the positive bifunctional air electrode, the electrolyte solution and a separator placed in the middle of the cell, as can be seen in Figure 2. The positive air electrode can be further divided into a gas diffusion layer (GDL) and a catalyst active layer. During the discharge process, zinc is oxidized to zinc cations at the negative electrode and electrons are generated (reaction (1)) and transferred to the positive electrode via an external circuit. Oxygen diffuses through the GDL to the catalyst active layer, where the oxygen reduction reaction (ORR) to hydroxide ions takes place at the positive electrode (reaction (4)) at a so-called three phase zone composed of the liquid electrolyte, the solid catalyst and the gaseous oxygen. Afterwards, the hydroxide ions migrate through the electrolyte and at the negative electrode they react with the zinc ions to form zincate ions ($Zn(OH)_4^{2-}$), which are decomposed to zinc oxide (ZnO) after saturation of the electrolyte (reaction (2) and (3)). The overall reaction can be summarized as the formation of zinc oxide (ZnO) by the reaction of Zn with O_2 (reaction (5)). During charging, the opposite reactions, oxygen evolution reaction (OER) and zinc deposition, occur. An overall theoretical cell voltage of $E°_{cell} = 1.66$ V is achieved where $E°_{cell} = E°_{cathode} - E°_{anode}$. However, the practical working voltage is much lower attributed to several voltage losses [3][4][9][18].

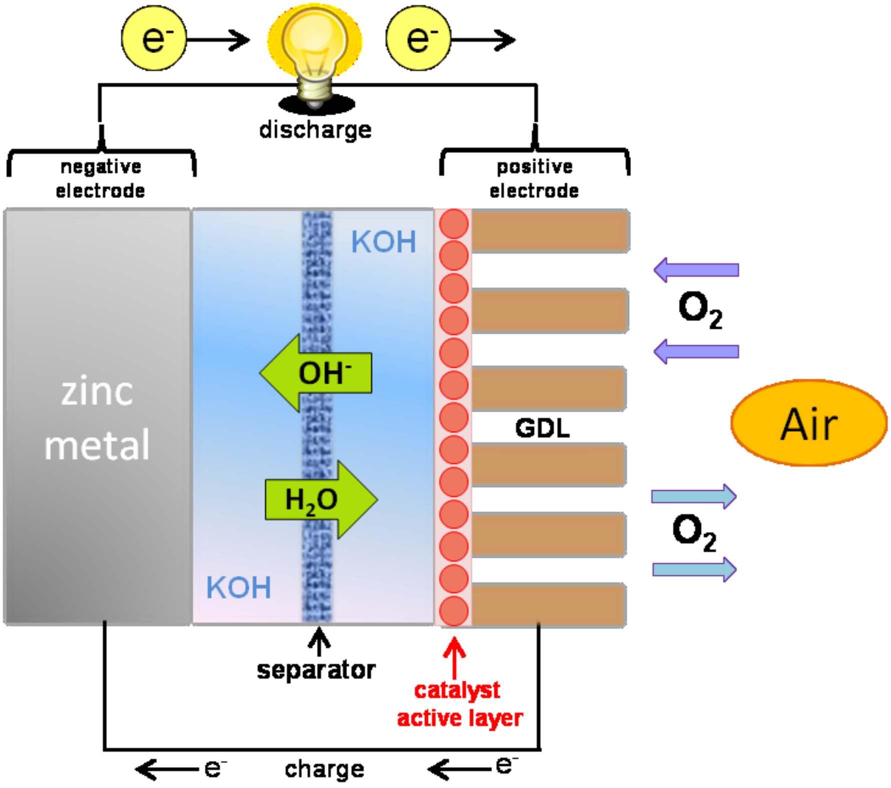

Figure 2: Schematic illustration of a secondary zinc-air battery.

Negative electrode: $Zn^{2+} \rightleftarrows Zn^{2+} + 2\ e^-$ (1)

$Zn^{2+} + 4\ OH^- \rightleftarrows Zn(OH)_4^{2-}$ $E° = -1.266$ V (2)

$Zn(OH)_4^{2-} \rightleftarrows ZnO + H_2O + 2\ OH^-$ (3)

Positive electrode: $O_2 + 2\ H_2O + 4\ e^- \rightleftarrows 4\ OH^-$ $E° = +0.401$ V (4)

Overall*:* $2\ Zn + O_2 \rightleftarrows 2\ ZnO$ $E_{cell}° = 1.667$ V (5)

2.2.1 Electrolyte

The electrolyte plays a crucial role in battery operation due to the fact that it is the medium where ionic migration takes place. Zinc-air batteries are mainly operated in aqueous alkaline electrolytes because of various advantages: low overpotential of the zinc, high ionic conductivity at low temperature and the availability of numerous well operating catalysts in alkaline media. The most used alkaline electrolytes are potassium hydroxide (KOH), sodium hydroxide (NaOH) or lithium hydroxide (LiOH). Potassium hydroxide is preferred over NaOH and LiOH due to the higher ionic conductivity at the same conditions and the fast electrochemical kinetics. In addition, the conductivity can be increased by increasing the concentration. However, higher concentrations also lead to higher viscosities thus decreasing the hydroxide ion transfer and increasing the formation of insoluble ZnO. Figure 3 shows a summary of different parameters as a function of KOH concentration. The preferred concentration applied in zinc-air batteries is approx. 7 M or 30 wt%, corresponding to the highest ionic conductivity [2][9]. Although potassium hydroxide electrolytes show many advantages, their main challenge is the high sensitivity to carbon dioxide in the atmosphere. The so-called carbonation of the electrolyte, where the reaction of CO_2 with the OH^- ions leads to capacity loss caused by precipitation of the carbonates in the pores, and blocking of the diffusion air part occurs [3][18][21]. A lot of research, for example on ionic liquids, is still done to solve this problem [9].

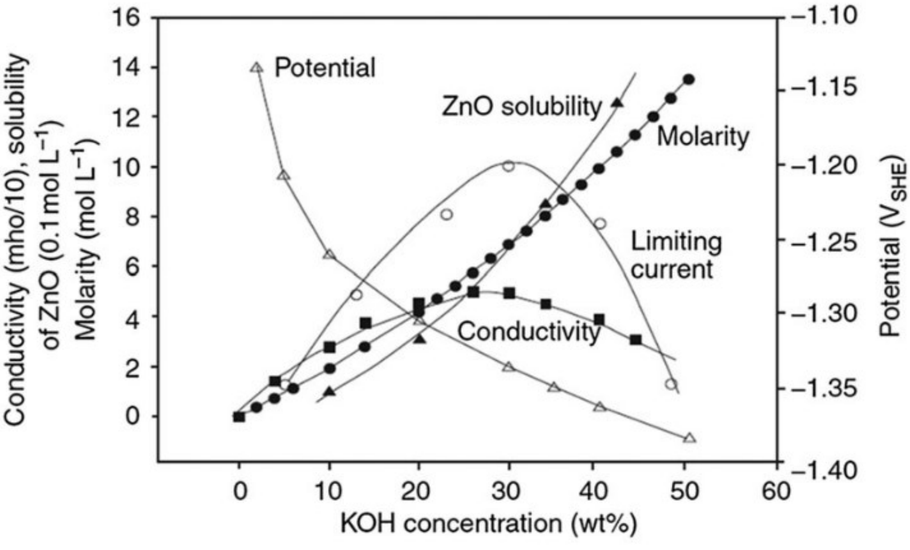

Figure 3: Summary of different parameters (● Molarity, ○ Limiting current, Δ Potential, ■ Conductivity, ▲ ZnO solubility) as a function of KOH concentration [2].

2.2.2 Separator

The main function of a separator is in general to physically isolate the positive electrode from the negative electrode and to be convenient for the transportation of ions from one to the other side. With regard to this, a separator must indicate properties like high ionic conductivity and high electric resistance, stability in alkaline media and appropriate pore size and porosity. Additionally, the separator should be inert to oxidation and retard short circuit caused by dendrite formation at the zinc electrode. Possible separator materials are different polymers like polyethylene (PE), polypropylene (PP) or polyvinylchloride (PVC) [3][9][18][21].

2.2.3 Zinc electrode

Zinc is frequently utilized as negative electrode material in secondary zinc-air batteries. Besides high specific energy density, constant discharge voltage and electrochemical reversibility, it is a metal with low equivalent weight, low cost, high abundance, low toxicity and it can be handled easily. In addition, zinc is relatively stable in terms of corrosion in aqueous alkaline media due to the fact that it is the most electropositive metal [3][9][21]. It is found out in many studies that the shape and morphology of zinc has a great influence on electrode performance. In most applications, the zinc electrode is made of granulated zinc powder mixed with some additives to reach high surface area leading to better results. Although there are many advantages, the performance of the zinc electrode is still limited by different phenomena. One of the biggest problem is the formation of dendrites during the charging process under certain conditions. These dendrites can fracture causing disconnection and thus leading to a capacity loss. Even worse, they can penetrate the separator, reach the positive electrode and cause a short circuit. The second limiting factor is related to shape change during several charge and discharge cycles, where zinc is dissolved and will be deposited again at different locations of the electrode. The result is densification of the electrode and thus capacity loss. Different approaches like the modification of the zinc electrode or doping of the electrolyte with additives are investigated to avoid such problems [21]. Further challenges arise in terms of passivation and internal resistance. When the electrolyte solution is saturated with zincate ions $Zn(OH)_4^{2-}$, insoluble ZnO is generated that precipitates on the electrode surface. An inert film is formed on the electrode surface leading to inhibited discharge reactions due to the fact that OH^- ions are not able to reach the zinc surface any more. Electrolyte additives are used as an approach to suppress the formation of such zinc oxides. Another limitation of the zinc electrode performance is attributed to hydrogen evolution leading to corrosion. Hydrogen can be produced because this reaction is favoured due to a higher standard reduction potential (-0.83 V) compared to Zn/ZnO (-1.26 V) [2][4].

2.2.4 Air electrode

In secondary zinc-air batteries, the positive air electrode plays a crucial role because the oxygen reduction (ORR) and oxygen evolution reaction (OER) still need further development in terms of their short cycle life. In addition, the power density of the battery system depends mainly on the performance of the positive electrode. It consists of two main parts, the hydrophobic gas diffusion layer (GDL) with the current collector and the hydrophilic catalyst active layer (Figure 4). The hydrophobic diffusion layer at the air-electrode interface should provide the oxygen diffusion and at the same time it should prevent the leakage of the aqueous electrolyte. Activated carbon or carbon nanotubes (CNT) can be used as a material for the GDL. In contrast, at the catalyst active layer the reactions take place at a so called three-phase zone (gaseous oxygen, liquid electrolyte, solid catalyst). Therefore, it should be able to concurrently allow the penetration of the electrolyte and the oxygen. The oxygen reduction reaction is a complicated mechanism, which can be proceeded either via a direct four-electron pathway or the two-electron hydrogen peroxide pathway (reaction (6) to (8)).

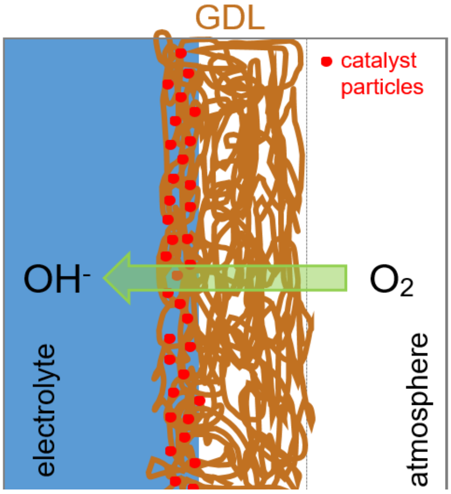

Figure 4: Schematic illustration of the bifunctional gas diffusion air electrode.

4e- pathway:

$$O_2 + 2\,H_2O + 4\,e^- \rightleftarrows 4\,OH^- \qquad (6)$$

2e- pathway:

$$O_2 + H_2O + 2\,e^- \rightleftarrows HO_2^- + OH^- \qquad (7)$$

$$H_2O + HO_2^- + 2\,e^- \rightleftarrows 3\,OH^- \qquad (8)$$

The oxygen reduction and evolution reactions are quite inhibited and therefore, it is necessary to find a catalyst which is able to accelerate both reactions. A catalyst of this kind is called bifunctional. This can be achieved only by one catalyst or by a combination of two or more. Platinum shows very good catalyst activities for ORR, but is a poor candidate for OER and additionally, noble metals are very expensive. As an alternative, transition metals like cobalt oxides or manganese oxides have been investigated because of their advantages like low cost, environmental friendliness, large abundance and high electrochemical activity [3][9][22]. Manganese oxides show promising electrocatalytic performance for ORR in alkaline media [13]. In addition, the $NiCo_2O_4$-spinel is considered to be an effective catalyst, especially for OER [23]. Therefore, manganese dioxide and $NiCo_2O_4$ were combined in this master's thesis to develop a promising bifunctional catalyst for OER and ORR (Figure 5).

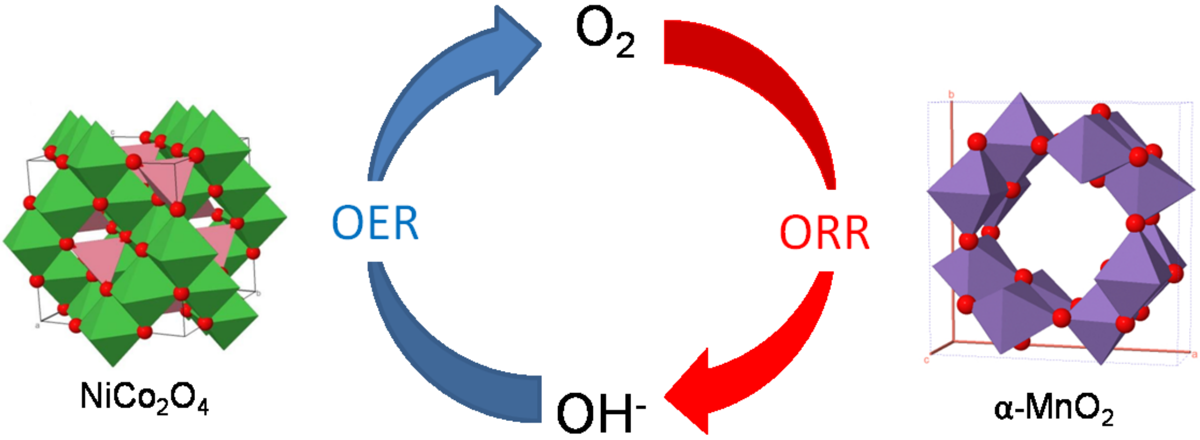

Figure 5: Oxygen evolution and oxygen reduction reaction (OER, ORR) [24].

2.3 $NiCo_2O_4$ spinel

In the crystal structure of a spinel, four primitive tetrahedral unit cells are arranged to a face centered cubic (fcc) unit cell. The general formula of the real spinel is $MgAl_2O_4$, but compounds with the same formula AB_2X_4 can also be named as a spinel, where on the one hand the postive metal ions are discribed as A and B and on the other hand X are the negative ions, mostly presenting oxygen. The primitive unit cell consists of two molecular AB_2X_4 units and consequently, the cubic unit cell consists of eight units with 32 anions and 24 cations (8 A ions and 16 B ions) resulting in a total of 56 atoms. In a spinel structure, the position of the negative ions is more or less fixed, whereas the arrengement of the positive ions A and B can vary. The cations can be arranged in two different ways forming a normal spinel like $MgAl_2O_4$ or an inverse spinel (e.g. $TiMg_2O_4$). In a normal spinel, the B atoms occupy one half of the tetrahedral sides and the A atoms are located in every eigth tetrahedral hole. In the case of an inverse spinel, the octahedral holes are occupied by the A atoms and one half of the B atoms and every eight tetrahedral interstices is also filled with the remaining B atoms [25–28]. $NiCo_2O_4$ is considered to be an inverse spinel, where the divalent nickel ions fill the octahedral holes and the trivalent cobalt ions randomly occupy octahedral and tetrahedral sides [29]. The crystal structure with different octahedral and tetrahedral interstices of $NiCo_2O_4$ can be seen in Figure 6.

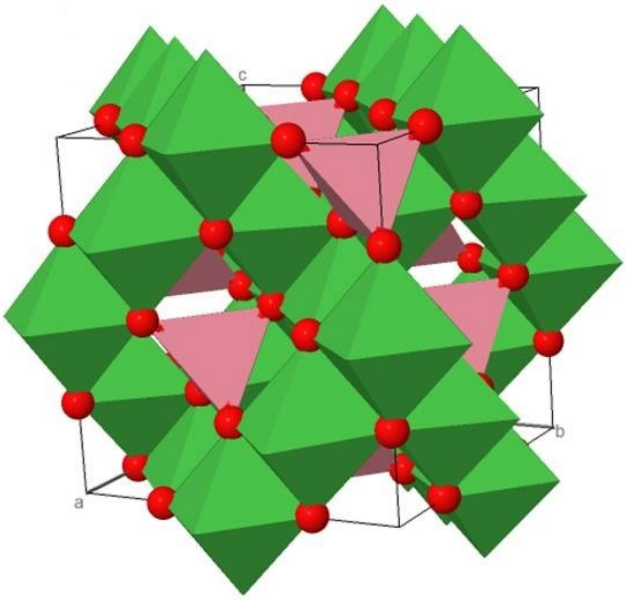

Figure 6: Crystal structure of $NiCo_2O_4$ with different octahedral and tetrahedral sides [23].

2.4 Manganese dioxide

2.4.1 Crystal structure

Manganese oxides can form over 30 different crystal structures having a great influence on the electrochemical performance. In general, the building block of all polymorphic types is an [MnO_6] octahedral, where a Mn^{4+} atom is located in the middle and is surrounded by six oxygen atoms. The octahedrons can be arranged in many different ways by edge or corner sharing forming either one dimensional (α-, β- and γ-MnO_2), two dimensional (δ-MnO_2) or three dimensional tunnels (λ-MnO_2 spinel). The crystal structures are distinguished according to the size of the different tunnels which are formed by the number of octahedral subunits (n x m). As shown in Figure 7, α-MnO_2 consists of octahedrons forming (2 x 2) tunnels and has the space-group symmetry I4/m (87) with a body-centred tetragonal lattice type. The intercalation of either water molecules or cations like K^+, Li^+ and Ca^{2+} is favoured due to its large open tunnel structure. The β-type is the most stable one consisting of single chain (1 x 1) tunnels with a simple tetragonal lattice and a $P4_2/mnm$ (136) space-group symmetry. In comparison to α-MnO_2, intercalation is not common for the β-type. The crystal structure of γ-MnO_2 displays double chained (1 x 2) and (1 x 1) tunnels. It has an orthorhombic unit cell with a space-group Pbnm (62) [30–34]. Another form known is the ε-MnO_2 showing a hexagonal close packed structure with a space-group P 63/mmc (194) comparable to γ-MnO_2, but it exhibits a higher degree of structural disorder (known as De Wolff disorder) and microtwinning [35][36].

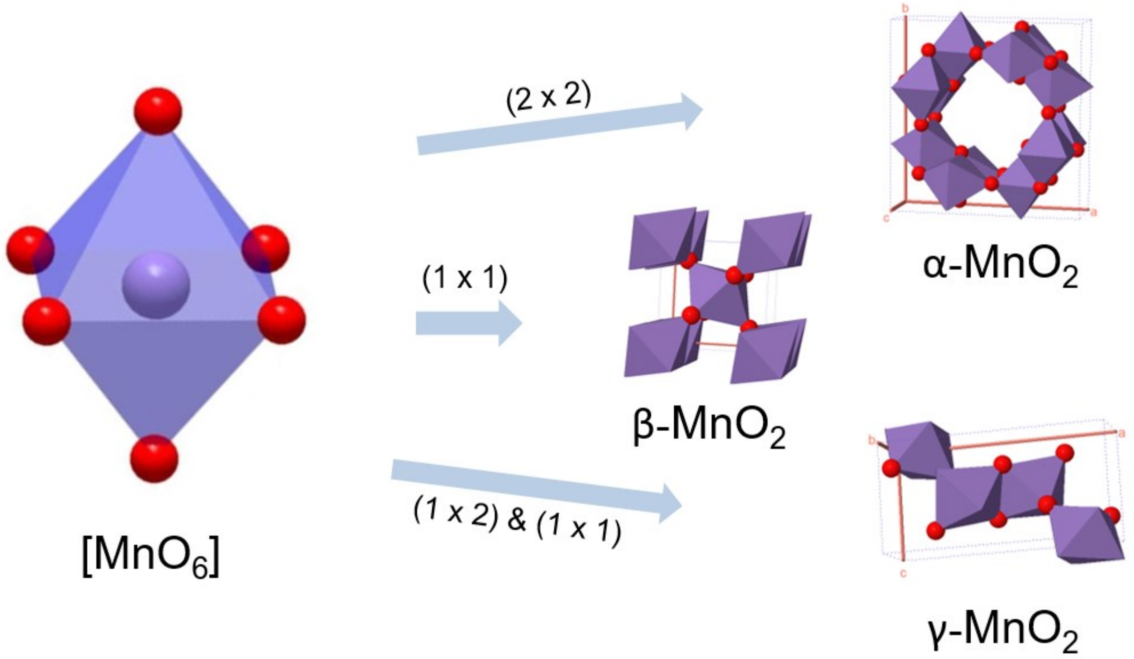

Figure 7: Crystal structure of α-, β- and γ-MnO_2 [24].

2.4.2 Synthesis of α-MnO_2

For the synthesis of α-MnO_2, a few production steps including calcination and an acid digestion process described in literature [14] are carried out. As a starting material for the acid digestion, Mn_2O_3 has to be produced. This process is based on a thermal method [37] by heating up ball-milled electrolytic manganese dioxide (EMD) to temperatures around 700°C. Manganese dioxide is converted to Mn_2O_3 and oxygen, which can be seen in the reaction below:

$$2\ MnO_2 \rightarrow Mn_2O_3 + \tfrac{1}{2}\ O_2 \qquad (9)$$

The pathway of the following acid digestion process is very complicated in terms of the reaction mechanism. A dissolution step of Mn_2O_3 (reaction (10)) is followed by precipitation of MnO_2. It also includes a disproportionation of the Mn(III) into Mn(IV) and Mn(II) (reaction (11)) as rate determining step (rds) [38][39]. The whole process is summarized in reaction (12).

dissolution: $Mn_2O_3 + 6\ H^+ \leftrightarrow 2\ Mn^{3+} + 3\ H_2O$ (10)

disproportionation-precipitation: $2\ Mn^{3+} + 2\ H_2O \leftrightarrow MnO_2\downarrow + Mn^{2+} + 4\ H^+$ (11)

overall: $Mn_2O_3 + 2H^+ \leftrightarrow MnO_2\downarrow + Mn^{2+} + H_2O$ (12)

For the formation of a defined MnO_2 phase, it is important to have a certain reaction temperature and acid concentration due to the solubility and disproportionation of Mn(III), what is described and explained by Walanda et al. [38]. The phase diagram can be seen in Figure 8.

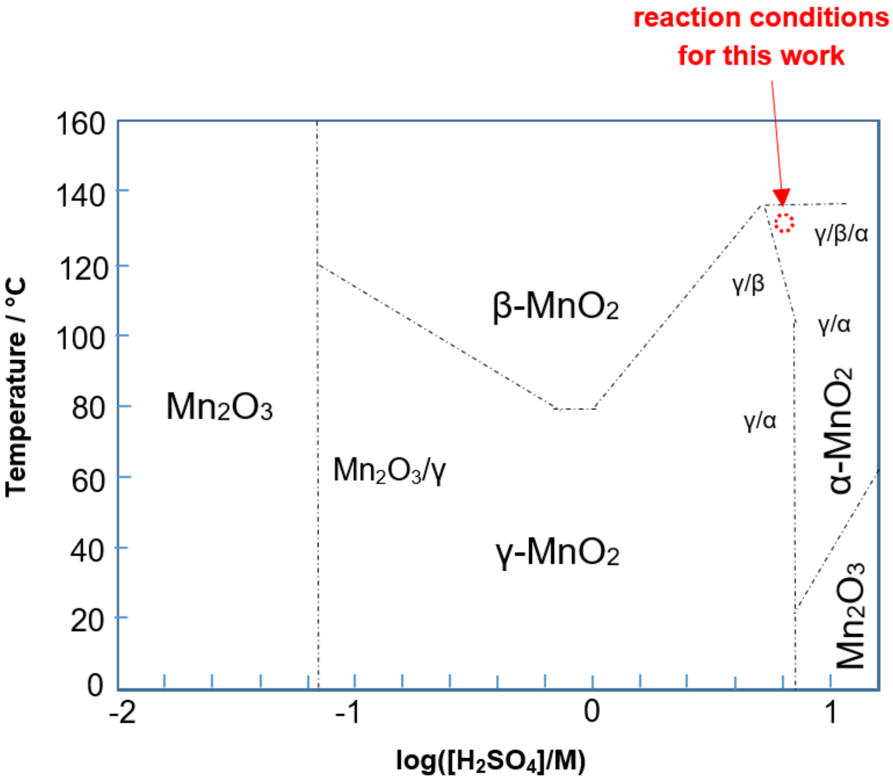

Figure 8: Phase diagram resulting from the acid digestion of Mn_2O_3 [38].

The transformation of Mn_2O_3 into MnO_2 has been regarded as an autocatalytic first order reaction with a reaction velocity *v*. As it can be seen in reaction (13), *k* indicates the rate constant and X_A and X_B are the mole fractions of Mn_2O_3 and MnO_2.

$$v = k(X_A)(X_B) \tag{13}$$

Therefore, the amount of Mn_2O_3 used for acid digestion may influence the properties of the manganese dioxide product. This effect is utilized in this work to produce two different forms of α-MnO_2 during the acid digestion process [14][40].

2.5 Physicochemical characterisation

2.5.1 X-ray diffractometry

X-ray diffraction (XRD) can be used to characterize a crystalline material. It provides information about the crystal structure, the lattice parameter and space group, chemical composition, the preferred crystal orientation as well as parameters like crystallinity or the average grain size. The atoms of a crystalline material are arranged in a regular array and the crystal structure is defined by a basic repeating unit with the lattice parameters a, b and c and the associated angles (Figure 9). The atoms form so-called mirror plates described by the Miller indices with a certain distance, which are able to diffract X-rays in a way that is specific for each material [41]. X-rays are electromagnetic waves with a wavelength in the range of 10 to 0.01 nm, much shorter compared to visible light (400 - 700 nm). They are generated in the radiation source (Figure 10), where a high voltage is applied under vacuum to a tungsten (W) filament generating electrons.

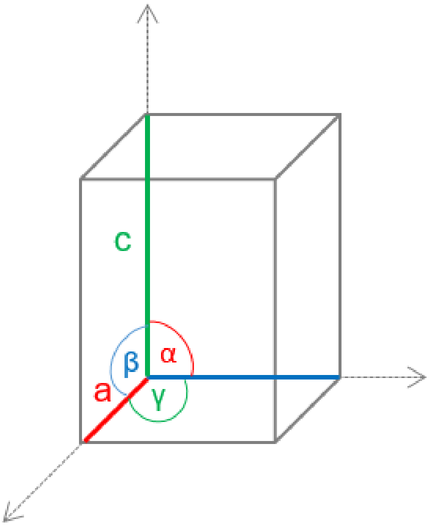

Figure 9: Schematic of a unit cell with lattice parameters a, b, c and the associated angles.

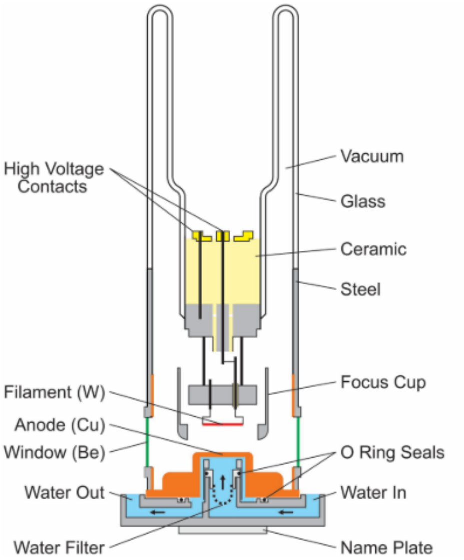

Figure 10: Illustration of the radiation source used for X-ray diffraction [42].

These electrons are focused and directed to an anode consisting of a pure metal (mostly copper), which emits X-rays according to two possible phenomena. On the one hand deceleration of the electrons in the magnetic field of the metal ions leads to the formation of X-rays called "Bremsstrahlung". On the other hand electrons from inner atomic shells can be ejected and the outer shell electron "jumps" into these gaps to get into a more stable state, what also causes X-ray generation. Depending on the initial and final shell position, different radiations like Kα1, Kα2 or Kβ are emitted (Figure 11). This process produces a lot of heat, hence the anode has to be cooled with water at the back. In terms of the X-ray diffraction, monochromatic radiation, mostly the strong Kα-radiation is needed. Therefore, filters or monochromators are used to get rid of the remaining radiations. The monochromatic X-rays are now focused to react with the crystalline sample, where they result weather constructive or destructive reflection. Constructive interference means that the phase difference between all waves is an integer n of the wavelength λ and they are "in phase", consequently reinforcing each other. In contrast, destructive interference means that the waves cancel each other in terms of a phase difference being nλ/2. Therefore, constructive interference is used for the XRD analysis, which conditions are geometrically described by the Bragg's law [41][43]. The illustration of the geometry used for the Bragg equation, which is derived from three main assumptions, can be seen in Figure 12.

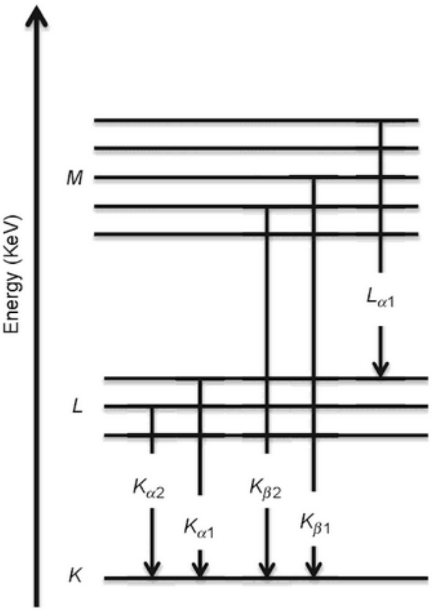

Figure 11: Schematic of the characteristic X-ray radiation according to the atomic energy levels.

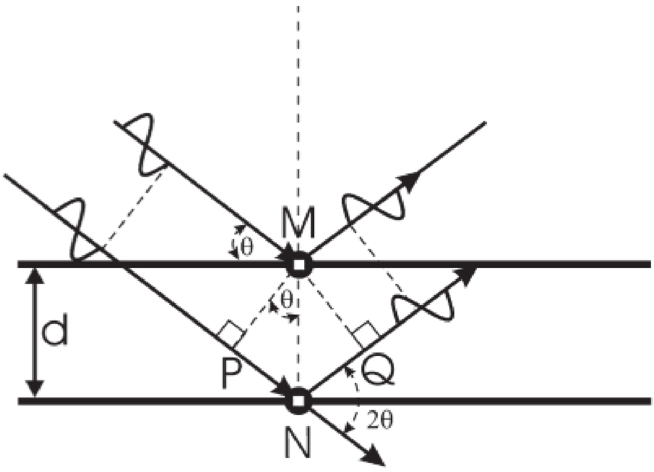

Figure 12: Illustrated geometry used for Bragg equation [42].

On the one hand Δ = PN+NQ has to be a multiple n (0,1,2,...) of the wavelength λ stated in equation (14). Equation (15) can be geometrically derived from the rectangular triangle seen in the illustration and as a consequence, equation (16) is obtained. Equalizing equation (14) and (16) results Bragg's law (equation (17)), where n is an integer named the order of reflection, λ is the wavelength of the X-ray beam, d_{hkl} is the interplanar spacing of the parallel lattice planes and θ is the diffraction angle [42].

$$\Delta = n\lambda \tag{14}$$

$$PN = NQ = d_{hkl} * \sin(\theta) \tag{15}$$

$$\Delta = 2d_{hkl} * \sin(\theta) \tag{16}$$

$$n\lambda = 2d_{hkl} * \sin(\theta) \tag{17}$$

The reflected X-rays are detected and the data can be used to generate an X-ray diffraction pattern, where the intensity is plotted against the diffraction angle 2θ. The diffractogramm displays peaks relating to different Miller indices characteristic and unique for each crystal structure. With Rietveld refinement, the data are compared with standards taken from a database and different properties like crystal structure, space group, lattice parameter or crystal orientation can be obtained. Additionally, the shape of the patterns gives information about whether the material exhibits large amorphous proportions (broad peaks) or is a crystalline solid (sharp, narrow peaks) illustrated in Figure 13 [41–43].

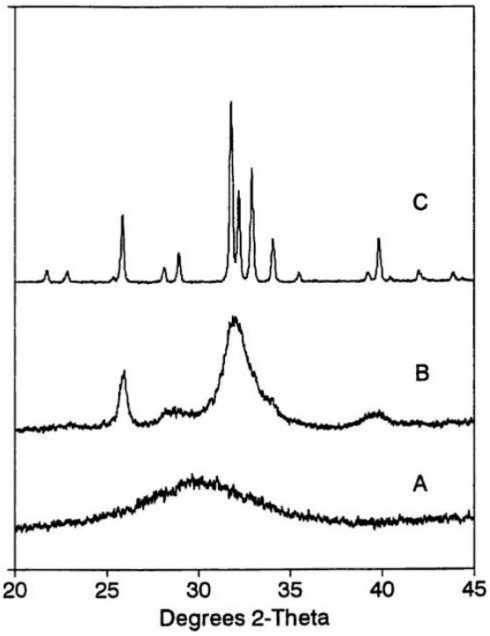

Figure 13: Illustration of amorphous (A), partly crystalline (B) and perfect crystalline (C) material [44].

For the determination of the average crystallite size (D), the Scherrer equation can be utilized [45]:

$$D = \frac{K*\lambda}{FWHM(2\theta)*\cos(\theta)} \tag{18}$$

D……..crystallite size [nm]
K……..constant close to 1
λ……...wavelength [nm]
θ……...diffraction angle [rad]
FWHM….full width at half maximum [nm]

2.5.2 Scanning electron microscopy

A microscope in general is a device which allows to visualize fine structural details within a sample that cannot be seen with the naked eye. A scanning electron microscope uses the same principle as a standard light microscope with the difference that an electron beam is reflected instead of visible light [45][46]. Figure 14 represents a schematic illustration of the components of a scanning electron microscope. The electron beam is produced using a so-called electron gun, which consists of a cathode made of tungsten (W) or LaB_6 and an anode. The electrons can be generated by a thermal method, where the cathode is heated until the electrons have enough energy to leave the cathode. A much more negative Wehnelt electrode between the cathode and anode is used to focus the electrons and to accelerate them towards the anode. The second possibility is to generate electrons via field emission by applying an electric field [46][47]. The accelerated electrons are focused using condenser lenses, objective lenses and scanning coils. The condenser lenses are magnetic lenses located nearest to the electron gun and they are used to reduce the cross sectional diameter of the electron beam to a few nanometres. The objective lenses are focusing the beam in the direction of the sample surface and the scanning coils allow the beam to scan the sample in x and y directions to produce images [46]. Finally, if the beam of primary electrons (PE) reaches the sample surface, different interactions can occur. On the one hand the electrons can be elastically scattered, which means that no energy is lost, and on the other hand inelastic scattering results some energy loss during interaction. According to the depth of reaction within a so-called teardrop shaped interaction volume (Figure 15), various types of signals including secondary electrons (SE), backscattered electrons (BSE), Auger electrons (AE) or X-rays can be produced. Secondary electrons are a result of inelastic scattering of the primary electrons with the outer electrons of an atom. In comparison, the backscattered electrons are generated via elastic scattering leading to much higher energies, what allows the electrons to escape from deeper regions. Auger electrons are a result of energy transition between the electron levels. For the capturing of the different signals, detectors are used to transduce them into electrical signals, which can be turned into images or graphs [46][47].

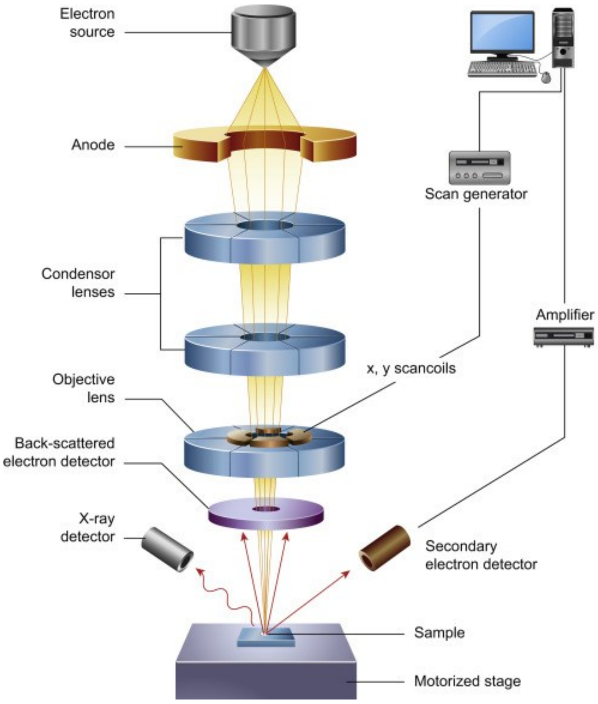

Figure 14: Schematic representation of a scanning electron microscope [43].

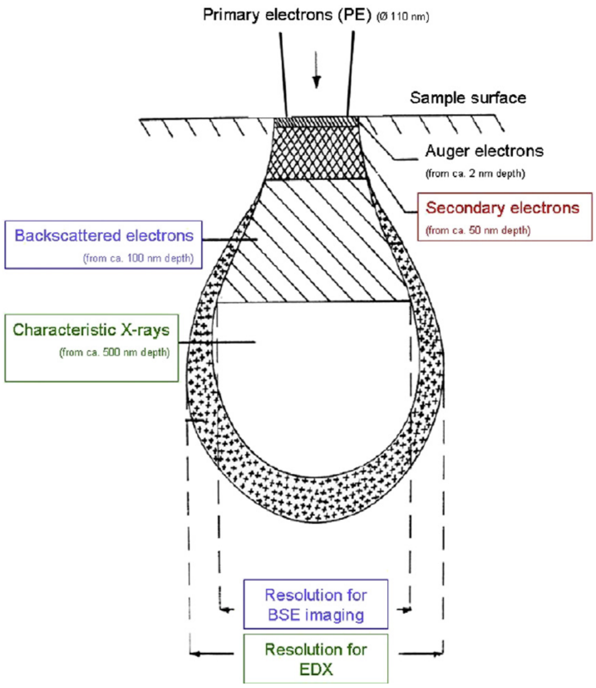

Represets

Figure 15: Signals emitted from different parts of the interaction volume [47].

2.5.3 Energy dispersive X-ray spectroscopy

Scanning electron microscopes are often combined with an energy dispersive X-ray analyser to get information about the chemical composition of a sample. X-rays are produced if the sample interacts with the electron beam. In this process, electrons are knocked out of inner shells of the atom. To compensate this unstable state, an electron from an upper shell jumps into this gap, which leads to the formation of X-rays. The energy value of the X-rays is characteristic for each chemical element, electronic layer (K, L, M) and electronic transition (α, β, χ, δ). A dispersive X-ray energy detector mostly consisting of Si and Li is used to collect the emitted X-ray photons and converts the energy into voltage signals, which are transformed into counts/channel and characteristic EDX spectra are obtained. From these spectra, information about the chemical composition is obtained [45–47]. Figure 16 shows such a spectrum of a α-MnO_2 sample.

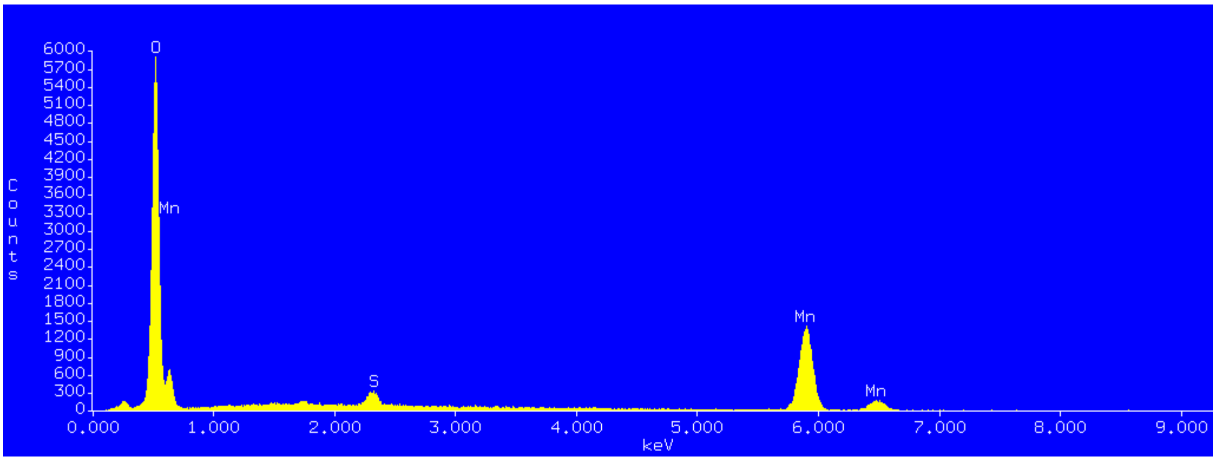

Figure 16: EDX spectrum of a α-MnO_2 sample.

2.5.4 Brunauer-Emmett-Teller method

The specific surface area plays a crucial role for bifunctional catalysts. Higher surface areas indicate better electrochemical performances due to more available active sites for the interaction between the catalyst and the electrolyte [13][31][48]. Various factors can have an impact on the surface area. For example, particle size reduction as a consequence of milling increases the surface area whereas it is reduced by high temperature processes, e.g. melting. The specific surface area is mostly determined via Brunauer-Emmett-Teller method based on a multilayer adsorption theory [49]. Adsorption is described as the accumulation of particles onto the surface of a solid. After a certain time, an equilibrium is reached that is strongly influenced by temperature, pressure and strength of interfacial intermolecular interactions. Two different types of surface adsorption are known: physisorption and chemisorption. During the chemisorption process, chemical bonds are formed and in contrast, physisorption is related to the formation of weak van der Waals bonds. The relation between the adsorbed amount on the surface and the partial pressure at a constant temperature is called adsorption isotherm. According to IUPAC [50], five major types of adsorption isotherms, depending on the physicochemical conditions of the interactions, are known (Figure 17) [45][49].

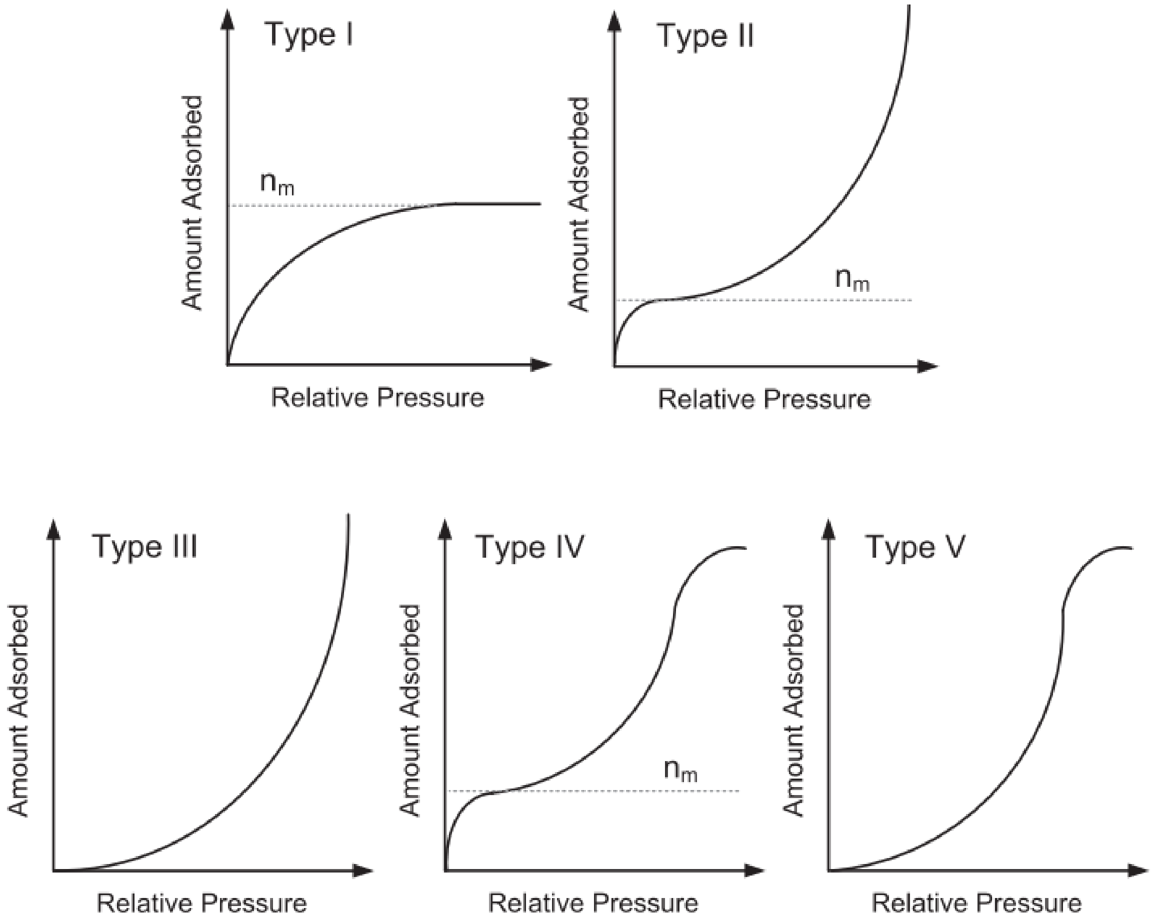

Figure 17: Five major adsorption isotherms according to IUPAC (nm = monolayer capacity) [49].

The BET equation (19) can be used to determine the amount of molecules, which is necessary to form a monolayer on the surface of the sample [45][51]. The equation can only be utilized for a type II or IV isotherm [52].

$$V = \frac{V_m * c * p}{(p_0 - p)\{1 + (c-1)p/p_0\}} \tag{19}$$

V……..volume of adsorbed gas [cm^3]

V_m……monolayer capacity [cm^3]

c ……..constant, related to the average heat of adsorption of the monolayer

p ……..vapour pressure [kPa]

p_0 …….saturation vapour pressure [kPa]

Equation (19) can be rearranged to a linear form of the BET equation:

$$\frac{p}{V(p_0\text{-}p)}=\frac{1}{V_m{*}c}+\frac{(c\text{-}1){*}p}{V_m{*}c{*}p_0} \tag{20}$$

The plot of $p/\{V(p_0\text{-}p)\}$ against p/p_0 should give a straight line in a certain p/p_0 range, called the adsorption (reversible) region of the isotherm. From the slope, V_m and c can be determined and according to equation (21), the specific surface area can be calculated.

$$S_{BET}=\frac{V_m{*}N_A{*}A}{M} * 10^{-20} \tag{21}$$

A…….. projected area of one adsorbate molecule on the surface [m²/molecule]
M..……molar volume [cm³/g*mole]
N_A……Avogadro's number [$6.022{*}10^{23}$ mol^{-1}]
S_{BET} …..specific surface area [m²/g]

2.5.5 Barrett-Joyner-Halenda method

The Barrett-Joyner-Halenda (BJH) method is widely used to determine the pore size distribution from the nitrogen adsorption isotherms type IV in the mesopore and small macropore range. According to IUPAC classification, it can be distinguished between micropores with a pore diameter up to 2 nm, mesopores (2 to 5 nm) and macropores (50 nm or higher). The BJH scheme is represented in the following equation:

$$V_{p_n}=R_n\Delta V_n\text{-}R_n\Delta t_n\sum_{j=1}^{n-1}c_jA_{pj} \tag{22}$$

where V_{pn} is the pore volume, $R_n = r_p^2/(r_k+\Delta t)^2$, r_p is the radius of the mesopore, r_k is the radius of the meniscus, V_n is the volume of the desorbed gas, t_n is the thickness of the adsorbed layer, c_j is the ratio of $(r_p\text{-}t)/r_p$ and A_{pj} is the area of each pore.

In this method it is assumed that the pores have a cylindrical shape and two general phenomena are happening in the pores: physical adsorption on the pore walls and capillary condensation in the inner capillary volume. Additionally, BJH method is based on the well-known Kelvin equation (23), as shown below, which is a relation of the curvature of the meniscus present in a pore to the p/p0 value associated with condensation [52–55],

$$r_k = \frac{2\gamma V_L}{RT \ln(p/p_0)} \tag{23}$$

where r_k is the radius of the meniscus, V_L is the molar volume of liquid adsorbate, γ is the surface tension, R is the gas constant and T is the absolute temperature. Figure 18 illustrates the shape of such a cylindrical pore with the physically adsorbed layer and the meniscus.

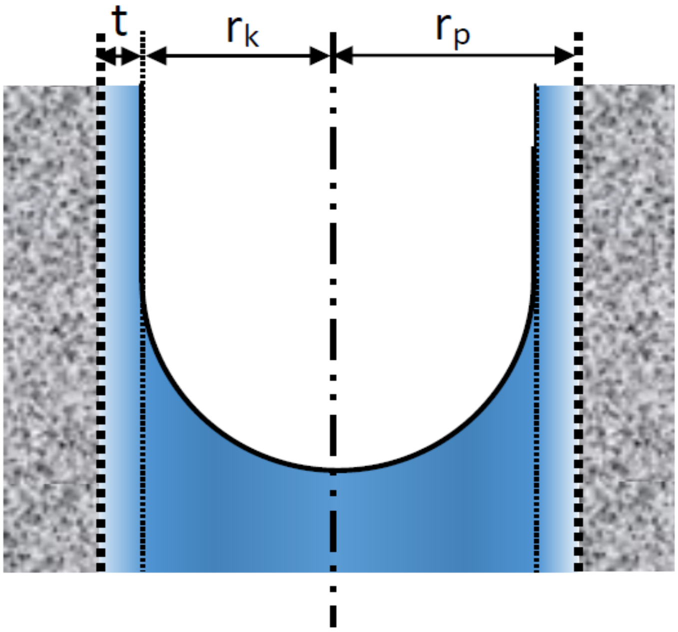

Figure 18: Illustration of the structure of a cylindrical shaped mesopore with physisorbed layer and meniscus [56].

As it can be seen, the radius r_p of the mesopore is a sum of the adsorbed layer thickness t (obtained from adsorption isotherm) and the radius of the meniscus r_k (equation 24). For the determination of r_k, equation (25) can be used. It is derived from Kelvin equation (23) using γ and V_L values of nitrogen at liquid nitrogen temperature (77 K) and assuming a cylindrical mesopore shape.

$$r_p = t + r_k \tag{24}$$

$$r_k = 0.953/\ln(p/p_0) \tag{25}$$

Pore size distribution is now obtained by plotting ΔV/Δr against the pore radius. The pore volume is obtained from equation (22) and the radius can be calculated using equation (24). A typical illustration of a pore size distribution according to Barrett-Joyner-Halenda (BJH) method is illustrated in Figure 19 [56].

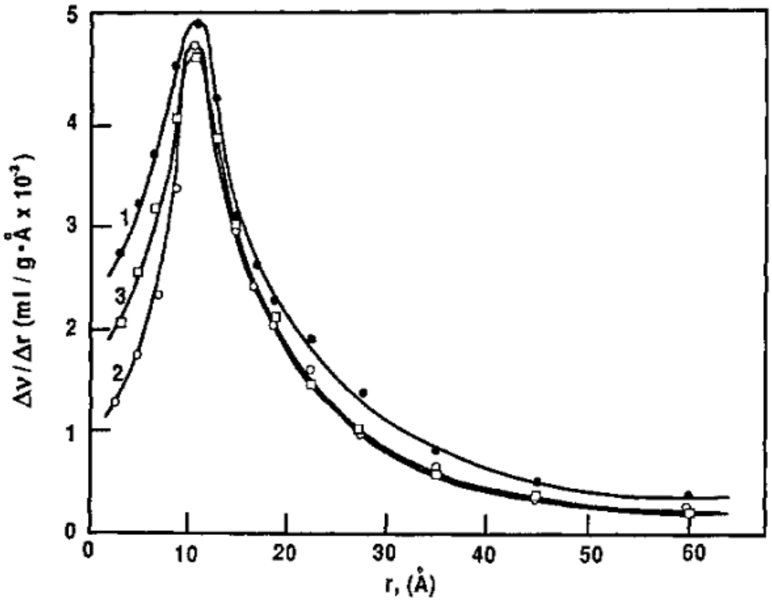

Figure 19: Illustration of a typical pore size distribution graph [45].

2.5.6 Structural and surface water content

The water content of a material has an effect on many properties, for example the electrocatalytic activity, density or electronic conductivity [57–60]. It can be distinguished between the surface water and structural water. The surface water is physically adsorbed on the surface of the crystallites and can be easily removed by applying vacuum or heating the sample to temperatures up to 100°C. The structural water is attributed to the chemically bonded water explained by Ruetschi et al. [37][57][60], who describes a cation vacancy model to explain the influence of the water content and the catalytic activity with an overall MnO_2 chemical formula of:

$$Mn_{1-x-y}{}^{4+} \cdot Mn_y{}^{3+} \cdot O_{2-4x-y}{}^{2-} \cdot OH_{4x+y}{}^{-} \qquad (26)$$

With this formula they explain that MnO_2 consists in general of Mn^{4+} and O^{2-}. This structure has also some defects, which might be cation vacancies, where a fraction x of Mn^{4+} is missing. For the compensation of the charges, OH^- ions replace some O^{2-}. In addition, y Mn^{4+} are exchanged by Mn^{3+} and the charge is again balanced via OH^- ions. In summary, manganese dioxide consists of Mn^{4+}, Mn^{3+}, O^{2-} and OH^- according to Ruetschi et al. [57]. The structural water is associated to the OH^- atoms. Thereby, a higher amount of structural defects and thus structural water leads to a higher catalytic activity.

The content of surface and structural water can be calculated according to the following equations:

$$\text{surface water } (\%\ H_2O_{Su}) = \frac{m0\text{-}m1}{m0} \times 100\ \% \tag{27}$$

$$\text{structural water } (\%\ H_2O_{St}) = \frac{m1\text{-}m2}{m1} \times 100\ \% \tag{28}$$

m0……..mass at the beginning

m1……..mass after 2 h at 110 °C and cooling down to RT in the desiccator

m2……..mass after 2 h at 400 °C and cooling down to RT in the desiccator

2.6 Electrochemical characterisation

2.6.1 Potential sweep voltammetry

Potential sweep voltammetry and especially cyclic voltammetry (CV) is used to get information of the electrochemical processes and the behaviour of reactions. For the investigation of such experiments, an electrochemical cell with a typical three electrode configuration including working, counter and reference electrode is utilized [61].

2.6.1.1 Linear sweep voltammetry

The simplest potential sweep technology is the linear sweep voltammetry (LSV), where a potential is applied and ramped linearly from the onset potential E_1 to a stop potential E_2 at a certain scan rate (Figure 20). The potential of the working electrode is plotted against the resulting current to give a voltammogram (Figure 21).

$$O + ne^- \rightleftarrows R \tag{29}$$

If a potential is applied to a species O or R like in the reversible reaction (29), the species is getting oxidised/reduced and the current increases according to Nernst equation, until an equilibrium [O] = [R] is achieved. A diffusion layer near the electrode surface continues to grow, slowing down mass transport of the O/R species to the electrode. This results in a decrease in the current and the peak like shape is formed [20][61][62][63].

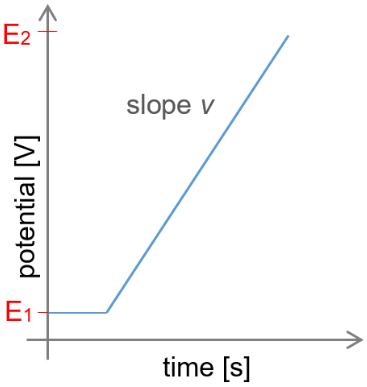

Figure 20: Potential-time curve of linear sweep voltammetry (LSV).

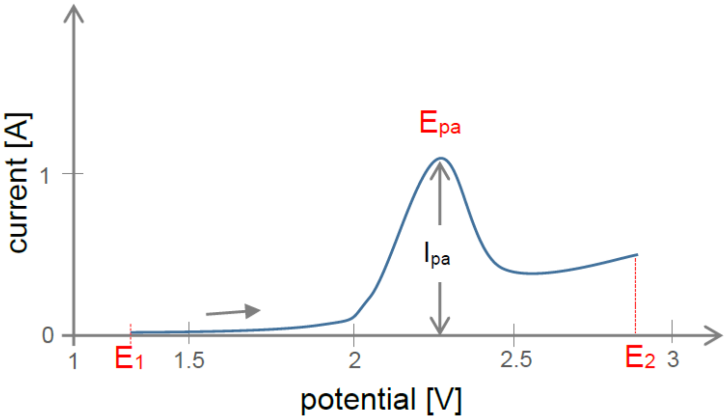

Figure 21: Linear sweep voltammogram of the reversible reaction $O + ne^- \rightleftarrows R$.

2.6.1.2 Cyclic voltammetry

In cyclic voltammetry (CV) experiments, the initial process is the same as for LSV, but the potential is ramped in the opposite direction after the so-called switching potential (E_2) is reached. This process can be repeated as many times as needed, resulting in a potential-time curve with a typical triangular shape (Figure 22). The applied potential is again plotted against the responding current giving a cyclic voltammogram, as shown for a reversible redox process (equation (29)) in Figure 23. Usually, species exist in their oxidised form, thus the potential is generally chosen to start in the negative-going direction, starting at a potential, where no reduction occurs. The oxidised species O is reduced to R forming a cathodic (reduction) peak. At a certain potential after the reduction peak, the sweep is reversed and the potential is applied in

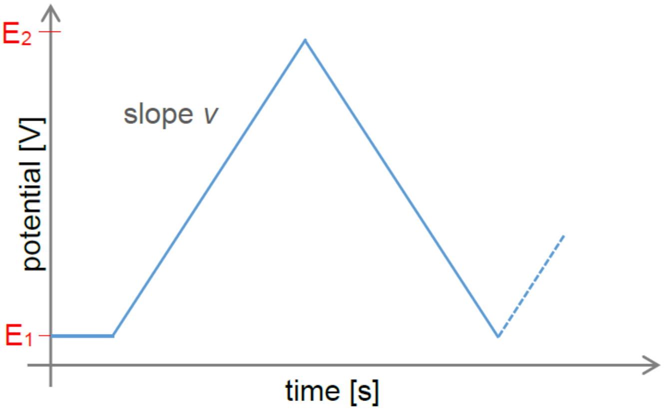

Figure 22: Potential-time curve of cyclic voltammetry (CV) with characteristic triangular shape.

the positive-going direction, where R is re-oxidised to O resulting in an anodic (oxidation) peak [61–63].

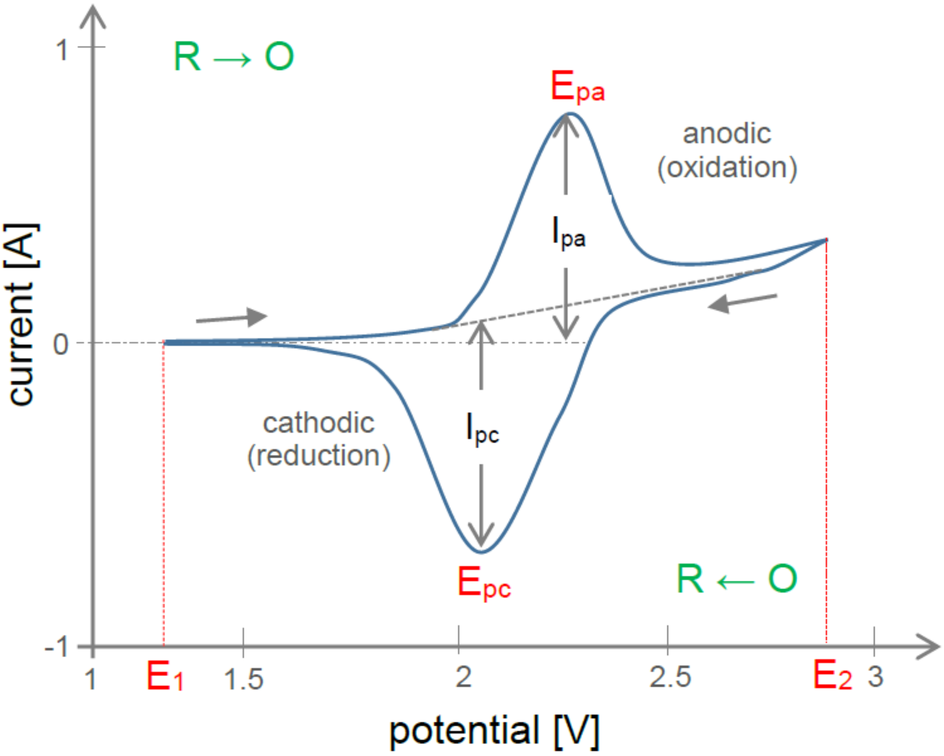

Figure 23: Illustration of a cyclic voltammogram of a reversible reaction O + ne⁻ ⇄ R.

The cyclic voltammograms can be analysed according to a few parameters including the anodic peak current (I_{pa}) and cathodic peak current (I_{pc}) as well as the anodic peak potential (E_{pa}) and the cathodic peak potential (E_{pc}). The peak currents for a reversible couple (at 25°C) can be given by the Randles–Sevcik equation [63]:

$$I_p=(2.69*10^5)n^{3/2}ACD^{1/2}v^{1/2} \tag{30}$$

I_p……..peak current [A]

n……..number of transferred electrons

A……..electrode area [cm²]

C……..concentration [mol/cm³]

D……..diffusion coefficient [cm²/s]

v……..scan rate [V/s]

According to this equation, the peak current is directly proportional to the concentration as well as to the square root of the scan rate *v*. In respect of this, the current increases linearly with the square root of the scan rate, what is a requirement for a reversible reaction. A few other parameters can be examined to confirm if the process is reversible or not. First of all, in a reversible system, the ratio of I_{pa} to I_{pc} always has to be one and the peak potential E_p should be independent of the scan rate. In addition, the difference of the peak potentials (ΔE_p) is given by the equation below [61][63]:

$$\Delta E_p = E_{pa} - E_{pc} = \frac{0.059}{n} \text{ V} \tag{31}$$

Thus, in a fast reversible one-electron process ΔE_p is about 59 mV. Furthermore, equation 31 can be used to determine the electrons transferred during the oxidation and reduction process. If these requirements are not fulfilled, an irreversible system with sluggish electron exchange is present indicated by shape change of the cyclic voltammograms [61][63][64].

2.6.2 Rotating disc electrode

A rotating disc electrode (RDE) is the most convenient and widely-used hydrodynamic working electrode applied in a three electrode cell to investigate kinetic and mechanistic studies of an electrochemical reaction [61][65]. The construction of such a rotating disc electrode is rather simple. It consists of a disc of the electrode material surrounded by an insulating material (mostly Teflon). The disc is connected to a motor, which enables the electrode to be rotated along the axis normal to the surface of the disc (Figure 24). The RDE acts like a pump that pulls the solution towards the electrode and finally, the centrifugal force flings the solution outwards (Figure 25) [64–66]. A well-defined laminar flow is generated, transporting the material from the bulk solution to the electrode surface. A relatively stagnant layer close to the electrode surface is formed, which is called the hydrodynamic boundary layer. An estimation of the thickness of this layer (δ_H) can be done with the equation below:

$$\delta_H = 3.6 \, (v/\omega)^{1/2} \tag{32}$$

where v is the kinematic viscosity of the solution and ω is the angular rotation rate given by $\omega = 2 \pi f / 60$ (f is the rotation rate in revolutions per minute). According to this equation, δ_H is about 300 to 400 µm in an aqueous solution [67].

A convection-diffusion concept mathematically describes the movement of the material to the electrode surface. While the mass transport into the stagnant layer is caused by convection, the final movement of the molecules to the closer electrode surface is caused by diffusion through a so called diffusion layer. The thickness of such a layer (δ_F) can be calculated according to the equation below:

$$\delta_F = 1.61\ D_F^{1/3}\ \nu^{1/6}\ \omega^{-1/2} \tag{33}$$

where D_F is the diffusion coefficient of a molecule. The diffusion layer is much thinner than the boundary layer giving a thickness of $\delta_F \approx 0.05\ \delta_H$ with a diffusion coefficient of $\approx 10^{-5}$ cm²/sec. The Levich equation (chapter 2.6.3.) describes the first mathematical treatment of such a convection-diffusion model [66][67].

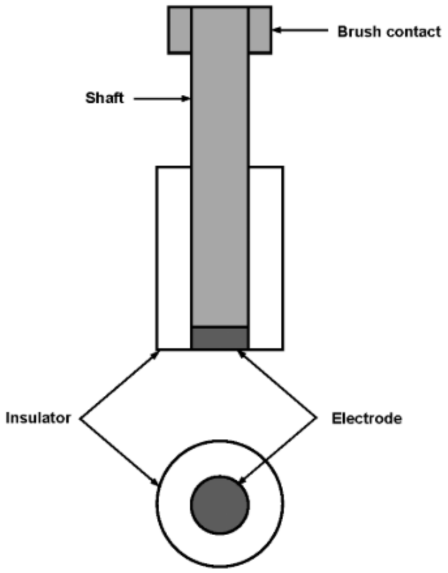

Figure 24: Schematic illustration of the components of a rotating disc electrode (RDE) [65].

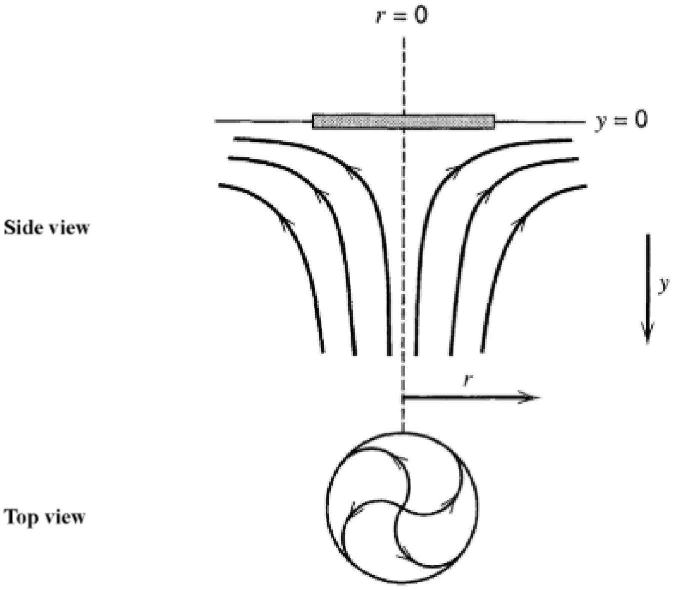

Figure 25: Representation of the convective flow caused by the rotating disc electrode (RDE) [64].

2.6.3 Levich and Koutecky-Levich analysis

The Levich and Koutecky-Levich analysis can be used to determine the number of electrons n, which are exchanged during the oxidation and reduction reaction. A rotating disc electrode is used to measure a series of voltammograms at different rotation rates. In the case of simple and reversible half reactions, the result are sigmoidal curves regardless of the rotation rate. An example of such voltammograms is illustrated in Figure 26. It can be seen that the current densities are not influenced by the rotation rates in the potential range of 0.85-0.93 V vs. RHE. According to this, the current densities is this region are controlled only by electron-transfer kinetics. At potentials below 0.85 V vs. RHE, the current densities increase with increasing rotation rate and at potentials more negative than ~0.57 V, a plateau is formed, which is called limiting current density limited by mass-transport [67][68].

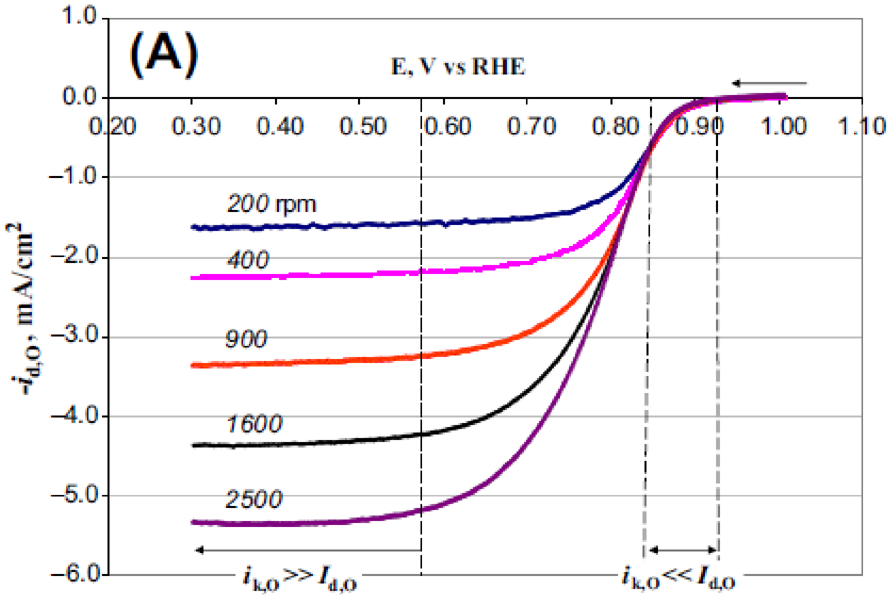

Figure 26: ORR voltamogramms using a Pt disc electrode in O_2 saturated 0.5 M H_2SO_4 at different rotation rates ω and a scan rate v of 5 mV s^{-1} [68].

For the Levich analysis, the measured limiting current densities at a certain potential are plotted against the square root of the rotation rate. A so called Levich-plot is gained, where the limiting current density should linearly increase with the square root of the rotation rate forming a straight line theoretically intercepting the vertical axis at zero (Figure 27, left) according to Levich equation (34) [67].

$$i_D = 0{,}62 * n * F * A * D_R^{2/3} * \omega^{1/2} * v^{-1/6} * C_R \qquad (34)$$

I_D ....Diffusion limited current [A]

n ....Number of electrons

F ....Faraday constant [96485 C/mol]

A ....Active area of electrode [cm^2]

D_R.......Diffusion coefficient [cm^2/s]

ω ....Rotation rate of electrode [rad/s]

v ....Kinematic viscosity [cm^2/s]

C_R .....Bulk concentration [mol/cm^3]

The equation can be rearranged and the number of electrons n can be calculated:

$$n = \frac{i_D}{0.62 * F * A * D_R^{2/3} * \omega^{1/2} * v^{-1/6} * C_R} \tag{35}$$

For the Koutecky-Levich analysis, the reciprocal current density at a certain potential is plotted against the reciprocal square root of the rotation rate forming straight lines intercepting the vertical axis at zero. An intercept unequal to zero gives a hint that the reaction is not only mass-transport controlled but also kinetically limited (i_K = kinetic current [A]). The illustration of a Koutecky-Levich plot can be seen in Figure 27 (right). The linear Koutecky-Levich equation is presented below [67]:

$$\frac{1}{i_D} = \frac{1}{i_K} + \left(\frac{1}{0.62 * n * F * A * D_R^{2/3} * v^{-1/6} * C_R}\right) \omega^{-1/2} \tag{36}$$

The number of electrons n can be derived from the slope of the curve according to the equations (37) and (38).

$$\text{Slope} = \frac{1}{0.62 * n * F * A * D_R^{2/3} * v^{-1/6} * C_R} \tag{37}$$

$$n = \frac{1}{\text{Slope} * 0.62 * F * A * D_R^{2/3} * v^{-1/6} * C_R} \tag{38}$$

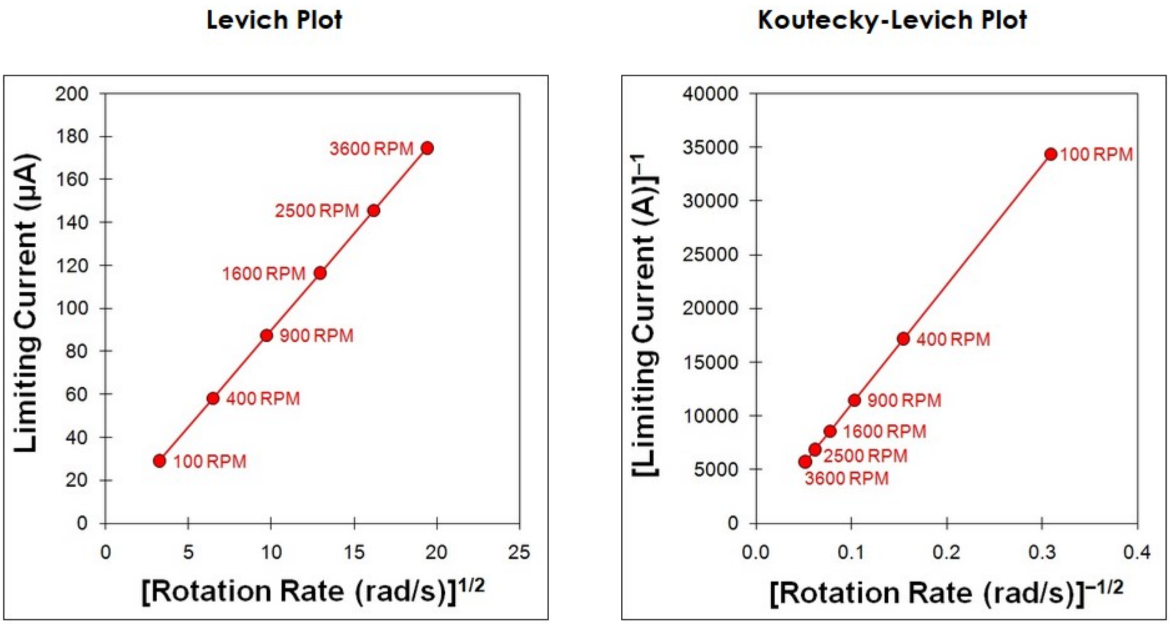

Levich Plot

Koutecky-Levich Plot

Figure 27: Illustration of a typical Levich plot (left) and Koutecky-Levich plot (right) [67].

3 Experimental procedure

Two different α-MnO_2 samples, based on the best working catalyst for OER and ORR in literature [14], are prepared in this work. They are combined in different ratios with a $NiCo_2O_4$ spinel synthesized in prior studies via hydroxide precipitation method [15]. The catalysts are physicochemically characterized and their electrochemical activity as a bifunctional catalyst for a secondary zinc-air battery is examined.

3.1 Catalyst preparation

As $NiCo_2O_4$ spinel, a sample labelled as P9 synthesised by Birgit Krenn and described in the master´s thesis [15], is used. This spinel showed the best performances for oxygen evolution reaction (OER) compared to all her samples. The catalyst is prepared via hydroxide precipitation method, where $Ni(NO_3)_2 \cdot 6\ H_2O$ and $Co(NO_3)_2 \cdot 6\ H_2O$ dissolved in deionised water are added dropwise to a NaOH solution yielding a blue/yellow precipitate after stirring at room temperature for 1.5 h. The precipitate is filtered, washed with deion. water and dried at 100 °C for 18 h. Afterwards, the dark brown powder is crushed in an agate mortar and sieved. Finally, the product is calcined at 375°C for 2 hours.

For the synthesis of α-MnO_2, a few production steps including calcination and an acid digestion process as described by Mainar et al. [14], are carried out. Prior to synthesis, the precursor material is ball-milled. The detailed procedures are as follows.

3.1.1 Ball-milling of electrolytic manganese dioxide (EMD)

Scanning electron microscopy images show that the particle size of the electrolytic manganese dioxide (EMD) used in this work is fairly big compared to the one of Mainar et al. [14]. Because of this, EMD is ball-milled at 400 revolutions per minute (rpm) for 2 hours (alternating: 15 min milling/15 min pause) using a planetary ball-mill (Fritsch Pulverisette 7 Premium Line), to gain smaller particles. Two zirconium oxide beakers filled with 180 balls of 5 mm diameter, respectively, made of the same material, are applied [69]. Each beaker is filled with 4 g of EMD.

3.1.2 Synthesis of Mn_2O_3 from EMD

For Mn_2O_3 production, 10 g of the milled EMD powder is heated up to 700 °C for 24 h in atmospheric air using a high temperature oven from Schröder (S13). The heating rate is 5 °C min^{-1}. The product is cooled down to room temperature in the desiccator and left there overnight. After this, the black powder is crushed with a mortar and filled into a vial.

3.1.3 Synthesis of α-MnO_2 catalysts via acid digestion

The final step is the synthesis of alpha-manganese dioxide using the Mn_2O_3 as starting material. It is converted into α-MnO_2 during an acid digestion process. Two different amounts of Mn_2O_3 in constant acid concentration and temperature are used, according to the best catalysts for OER and ORR in the work of Mainar et al. [14] (ORR: 18 g and OER: 10 g; in 1 L 6 M H_2SO_4). In this work, 4.5 g and 2.5 g Mn_2O_3, respectively, are treated with 250 mL of 6 M H_2SO_4 at 130°C for 16 h. The two synthesized samples are labeled as α-MnO_2-18 g and α-MnO_2-10 g. At first, 250 mL of 6M H_2SO_4 solution are prepared in an Erlenmeyer flask by diluting of concentrated sulfuric acid (Figure 28).

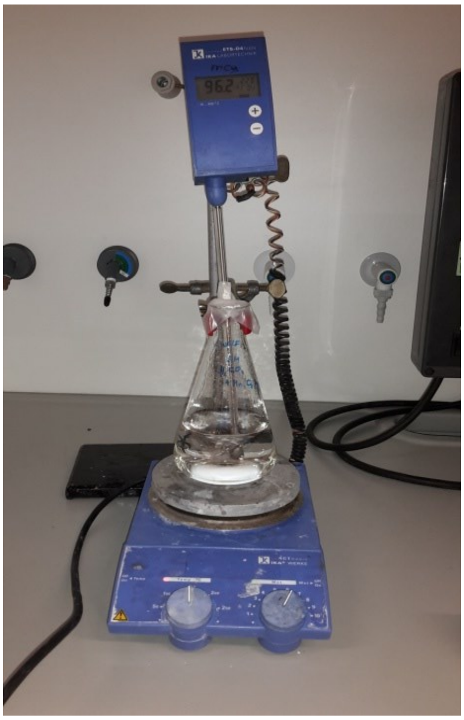

Figure 28: Acid digestion.

Afterwards, the diluted acid is heated up until 130 °C is reached and then, Mn_2O_3 is added. The solution is kept under magnetic stirring at 130°C for 16 h. The Erlenmeyer flask is covered with parafilm to reduce the evaporation of the solution. Because of the volume loss, the solution is filled up once to 250 ml with deionized water. After the mixture is cooled down, the black/brown precipitate is filtered with a glass frit (P4) and washed two times with deionized water and ethanol to get rid of the excessive acid (Figure 29). Subsequently, after drying the wet powder (Figure 30) in the desiccator overnight, it was finally dried at 110°C for 2 hours.

Figure 29: Filtration of α-MnO_2.

Figure 30: Wet α-MnO_2 powder.

3.2 Physicochemical measurements

For the investigation of the physicochemical properties of the different manganese oxides (EMD, Mn_2O_3, α-MnO_2-18 g and α-MnO_2-10 g) various measurements are carried out. Structure characterisation is done by means of X-ray powder diffraction. Morphology, particle size and composition of the samples are examined by scanning electron microscopy (SEM) and energy dispersive X-ray spectroscopy (EDX). Brunauer-Emmett-Teller (BET) and Barrett-Joyner-Halenda (BJH) method are used to determine the specific surface area as well as the porosity of the manganese oxides. Additionally, the water content is examined via thermal treatment.

3.2.1 X-ray diffractometry

The characterisation of the structure is done by means of a Bruker D8 Advance powder diffractometer, with a Cu-Kα X-ray source (λ=1.5418 Å) in the range of 15° to 80° 2θ with a step size of 0.02° and a count time of 5s/step. The analysis are performed at the Institute for Physical Chemistry at Graz University of Technology. The software program X´Pert HighScore plus (PANalytical) is used for data analysis and the evaluation of the diffractograms is done by Rietveld refinement. The measured values are compared and fitted with the ones calculated from a structural model (Literature data ICSD). Additionally, the XRD patterns are illustrated and compared with the literature data. The Scherrer equation is used to estimate the crystallite size of the different powders.

3.2.2 Scanning electron microscopy

For the determination of the morphology and particle size of the manganese oxide samples, images with an ESEM Tescan 500 PA and a Zeiss DSM 982 scanning electron microscope are recorded at various magnifications. The samples are fixed by utilizing a double-sided carbon tape placed on a specimen holder.

3.2.3 Energy dispersive X-ray spectroscopy

The elemental composition of the powders is obtained by energy dispersive X-ray spectroscopy (EDX) using an analyser from Oxford Instruments. The spectra are recorded at three different areas, to obtain the average atomic and weight percentages of the elements present in the manganese oxide powders.

3.2.4 Brunauer-Emmett-Teller and Barrett-Joyner-Halenda measurements

For the calculation of the specific surface area (SSA), the Brunauer-Emmett-Teller method (BET) is utilized. The measurements are performed at the Institute for Process and Particle Engineering at Graz University of Technology. The data are obtained on a TriStar II 3020 apparatus. The samples are outgassed at 100°C for 24 h, before the main analysis is started at 77 K. Afterwards, a monolayer of nitrogen (N_2) is formed on the surface of the α-MnO_2 samples. The volume of adsorbed N_2 is determined and the N_2 adsorption/desorption isotherms are recorded in a relative pressure range of 0.01 to 0.99. By applying the BET equation, the specific surface area is calculated by taking eight points between a relative pressure range of 0.05 – 0.2. Afterwards, the volume of pores between 1.70 nm and 300 nm diameter and the pore size is determined using the Barrett-Joyner-Halenda (BJH) method.

3.2.5 Surface and structural water content

After the synthesis of α-MnO_2, the structural and surface water content of the alpha-manganese dioxides are examined [38]. For the determination, 500 mg (m0) of the catalysts are heated up to 110 °C for 2 h in a furnace. Subsequently, the powder is cooled down to room temperature in the desiccator to avoid adsorption of moisture. The weight of the sample is quantified again (m1) to calculate the surface water content, which is attributed to the loss of physically adsorbed water. Afterwards, the powder used before is treated in another heating process applying a temperature of 400 °C for 2 h using a high temperature oven (Schröder S13). The material is cooled down to room temperature in the desiccator and weighed once again (m2) to determine the structural water content, which is attributed to the loss of chemically bond water. The calculations are done with equations (27) and (28) given in the theory part.

3.3 Electrochemical characterisation

For the examination of the electrochemical performance of the α-MnO_2, $NiCo_2O_4$ and mixed α-MnO_2/$NiCo_2O_4$ catalysts, half-cell experiments including cyclic voltammetry (CV) and linear sweep voltammetry (LSV) are carried out. The measurements are performed using a rotating disc electrode (RDE) from Pine Instruments Co. (AFMSRCE) with a typical three-electrode setup. An Autolab PGSTAT potentiostat (AUT83568 and AUT86739) including the software NOVA 1.11 is used for data analysis. The cyclic voltammetry experiments are performed for the investigation of various oxidation and reduction processes of the manganese oxides and $NiCo_2O_4$ spinel as well as for examining long term stability. The bifunctional activity of the catalysts concerning oxygen reduction (ORR) and oxygen evolution reaction (OER) kinetics is examined via linear sweep voltammetry measurements.

3.3.1 Working electrode preparation

For the preparation of the working electrode, the catalyst is transferred to a glassy carbon (GC) rotating disk electrode (Ø = 5 mm; 0,196 cm^2) via a suspension [14]. In this work, five different slurries (Figure 31, left) are produced as summarized in Table 1. The catalyst powders of pure α-MnO_2 and of mixed samples are mixed with 5 ml isopropanol/water solution (7:3, v:v). Additionally, they are blended with carbon powder in a ratio of 1:1 (MnO_2:carbon powder). For the pure $NiCo_2O_4$ spinel slurry, the catalyst powder is mixed with 6 ml of deionized water. All suspensions are ultrasonically blended for 30 min. Before each measurement, the RDE is polished with an Al_2O_3 powder (particle size 0.3 µm) and water, cleaned in the ultrasonic bath and dried with the infrared (IR) lamp. Afterwards, either two times 5 µl (for α-MnO_2 and mixed catalysts) or three times 15 µl (for $NiCo_2O_4$) of the suspension are pipetted very carefully on the GC disc, respectively. After each pipetting step, the catalyst is left to dry by a rotation speed of 400 rpm at room temperature in the case of the pure α-MnO_2 and mixed catalysts. The $NiCo_2O_4$ suspension is dried under the IR lamp (Figure 31, right). A final Nafion layer was applied to ensure stability of the catalyst layer.

Table 1: Composition of the catalyst suspension and final catalyst loading.

Slurry	**α-MnO_2 [mg]**	**$NiCo_2O_4$ [mg]**	**Vulcan XC-72 [mg]**	**Catalyst loading [mg/cm^2]**
1 (α-MnO_2)	9.8	-	9.8	0.100
2 ($NiCo_2O_4$)	-	2	-	0.077
3 (α-MnO_2/$NiCo_2O_4$ 1:1)	4.9	4.9	4.9	0.100
4 (α-MnO_2/$NiCo_2O_4$ 1:1 double)	9.8	9.8	9.8	0.200
5 (α-MnO_2/$NiCo_2O_4$ 4:1)	7.35	2.45	7.35	0.100

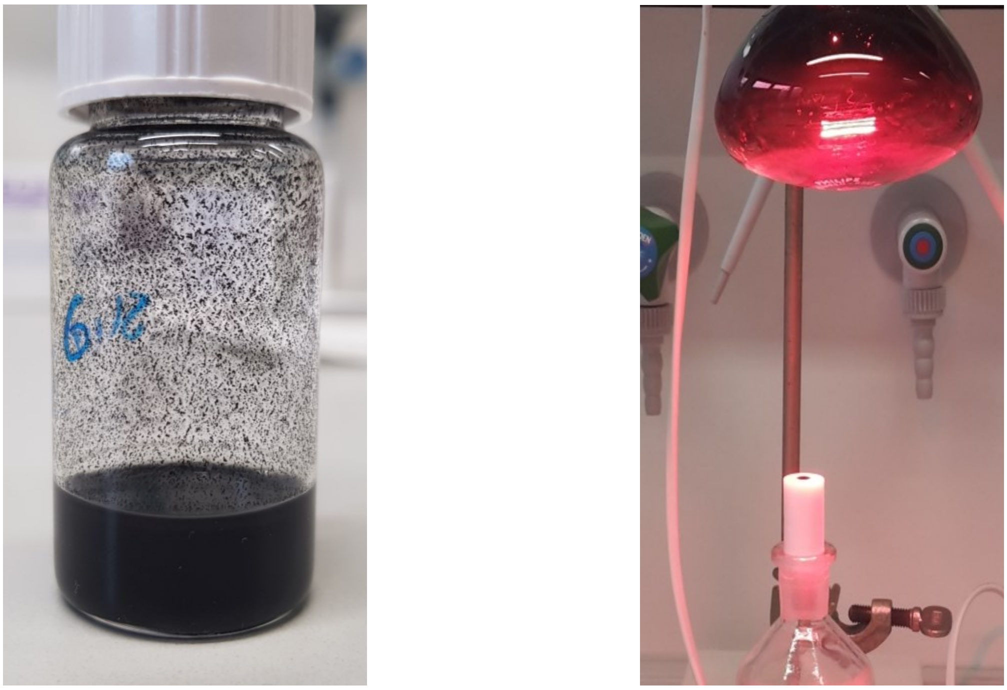

Figure 31: *Catalyst suspension (left) and* drying of the catalyst and Nafion layer under *IR lamp (right)*.

3.3.2 Cyclic voltammetry, oxygen evolution and reduction reaction measurements

The rotating disc electrode (RDE) is assembled in a three-electrode cell (Figure 32), which consists of the working, counter and reference electrode. The RDE is used as the working electrode and the counter electrode is a platinum net. An Hg/HgO reference electrode in a Haber Luggin-Capillary filled with 8 M or 0.1 M KOH is utilized. Potassium hydroxide solution (0.1 M and 8 M) is used as alkaline electrolyte. Prior to recording the CV and the OER measurements, the solution is purged with nitrogen for 30 min to remove oxygen from the solution. For ORR measurements, the cell is aerated before with oxygen for 30 min. During the measurements, O_2 or N_2 is blown over the solution, respectively. All measurements are done at room temperature.

Five voltammograms for OER and ORR are recorded at a scan rate of 5 mVs^{-1} and a rotation rate of 1600 rpm. The fifth sweep was used for data comparison. An additional voltammogram for OER at 400 rpm and for ORR at 900 rpm is recorded to compare it with data from other projects and to investigate the influence of the rotation rate on the catalytic activity. The cyclic voltammetry measurements are performed at a scan rate of 10 mVs^{-1} and the second cycle is used for comparison.

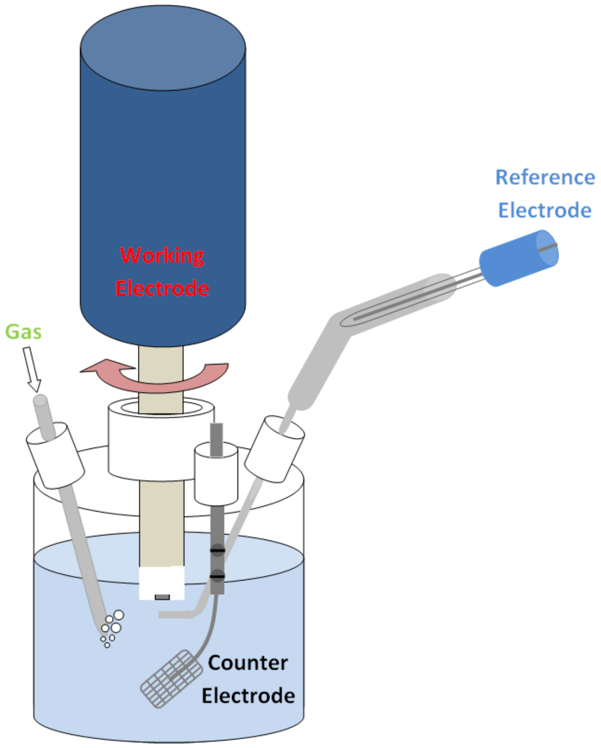

Figure 32: Assembling of the electrochemical cell.

3.3.3 Levich and Koutecky-Levich analysis

The Levich and Koutecky-Levich analysis are used to determine the number of electrons n, which are transferred during the oxygen reduction reaction. The values of the diffusion coefficient D_0 of O_2 in solution (1.73×10^{-5} $cm^2\ s^{-1}$ in 0.1 M KOH), the bulk concentration C_R of O_2 in solution (1.14×10^{-6} mol cm^{-3} in 0.1 M KOH) and the kinematic viscosity v (0.01 $cm^2\ s^{-1}$ for 0.1 M KOH) are taken from literature [31]. The geometric area of the RDE is 0.196 cm^2. The voltammograms are recorded at five different rotation rates (100, 400, 900, 1600, 2500 rpm). According to the Levich equation, given in the theory part (2.6.3), the limiting current density is plotted against the square root of the rotation speed. After confirming linearity of the graph, the number of electrons n can be calculated. For the Koutecky-Levich analysis, the reciprocal limiting current density is plotted against the reciprocal square root of the rotation speed and the number of electrons is obtained via the slope.

4 Results and discussion

4.1 Physicochemical characterisation

4.1.1 X-ray diffraction

The XRD patterns of EMD, Mn_2O_3, α-MnO_2-10 g and α-MnO_2-18 g can be seen in Figure 33. Additionally, diffractograms from the Inorganic Crystal Structure Database (ICSD) [24] are added in the case of Mn_2O_3 (ICSD: 9090) and α-MnO_2 (ICSD: 20227). Rietveld refinement of the starting material EMD shows a mixture of approx. 43 vol% γ-MnO_2 (ICSD: 54114) and 57 vol% ε-MnO_2 (ICSD: 76430). Comparing the diffractogram of this study with those of Walanda et al. [38] and Dias et al. [59], they look quite similar and all characteristic peaks could be obtained, what is denoted in Figure 33. Furthermore, the XRD pattern shows very broad peaks and a high background, what may indicate small crystallites and a high amount of amorphous parts. After the heating process, the diffractogram of the produced Mn_2O_3 demonstrates very sharp and narrow peaks, what can be assigned to high crystallinity. With Rietveld refinement, this assumption could be proofed due to the fact that all reflections relate to very crystalline, phase pure, orthorhombic α-Mn_2O_3. The X-ray diffraction patterns of both α-MnO_2 samples look quite similar, with the only difference, that the 18 g sample shows slightly different intensities caused by texture. High crystallinity is again indicated by sharp peaks. The measured values are again compared and fitted with the ones calculated from a structural model (Literature data ICSD) using Rietveld refinement. All diffraction peaks can be clearly indexed to α-MnO_2 presenting a tetragonal crystal structure with a space group of I4/m (87). In addition, no significant peaks from other phases or impurities could be detected, what demonstrates a high phase-purity of the products. The crystallite size of the two α-MnO_2 products is estimated via Scherrer equation with the assumption of spherical particles and k=0.9 is generally taken for powders [59]. For the calculation of the crystallite size, the average FWHM of several peaks is used. A crystallite size of approximately 18 nm for both products is determined. Figure 34 shows that α-MnO_2-10 g and α-MnO_2-18 g present the same shape and width of the peaks and therefore, the same values of FWHM yield identical results.

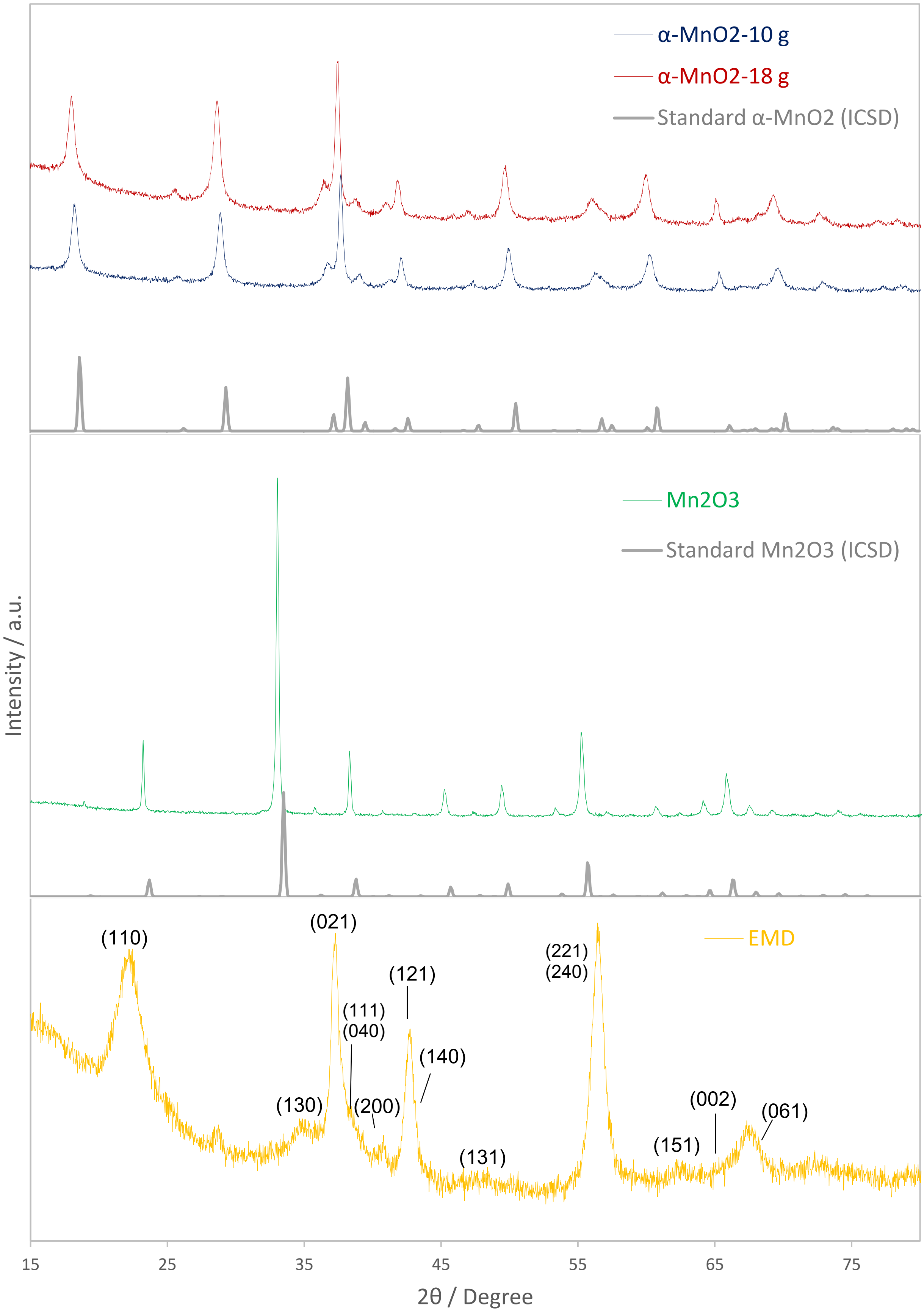

Figure 33: X-ray diffraction patterns of different manganese oxide samples compared with data from ICSD.

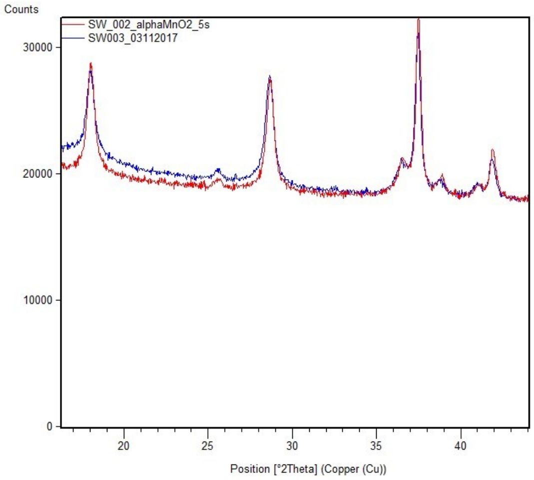

Figure 34: Scaled XRD patterns of α-MnO_2-10 g and α-MnO_2-18 g utilized for crystallite size analysis.

Furthermore, the lattice constants a, b and c of all manganese oxide samples are determined via Rietveld refinement as can be seen in Table 2. The results fit with the lattice constants taken from literature.

Table 2: Lattice constants of EMD, Mn_2O_3, α-MnO_2-10 g and α-MnO_2-18 g compared with literature data from the ICSD [24].

	a [Å]	**b [Å]**	**c [Å]**
EMD (γ-MnO_2)	4.381	9.485	2.835
EMD (ε -MnO_2)	2.773	2.773	4.415
γ-MnO_2 (ICSD #54114)	4.264	9.513	2.859
ε-MnO_2 (ICSD #76403)	2.786	2.786	4.412
Mn_2O_3	9.414	9.422	9.405
Mn_2O_3 (ICSD #9090)	9.416	9.423	9.405
α-MnO_2-10 g	9.833	9.833	2.861
α-MnO_2-18 g	9.850	9.850	2.863
α-MnO_2 (ICSD #20227)	9.784	9.784	2.863

4.1.2 Scanning electron microscopy

The images of different manganese oxides investigated by scanning electron microscopy for the shape, morphology and particle size analysis can be seen in Figure 35 to Figure 40. The first three pictures (Figure 35 to Figure 37) show the starting material EMD, which is used for α-MnO_2 production, before and after the ball-milling process. The unground EMD powder looks like crushed stone plates, which have a size from 2.5 µm up to 50 µm. A few finely powdered particles in the nanometer range can be recognized. After milling, the particle size is drastically reduced to a range of 0.2 to 5 µm and the particle size distribution is much more uniformly. Mn_2O_3 (Figure 38) demonstrates a reef-like morphology compared to the porous electrolytic manganese dioxide as also described by Mainar et al. and others [14][70–72]. Agglomerates with sizes up to 15 µm are covered with smaller spherical particles in the nano size range. Figure 39 and Figure 40 present the SEM-images of both α-MnO_2 samples, which illustrate the same surface shape of quasi-spherical particles in the range of 0.5 to 10 µm. Bigger particles can be recognized for the α-MnO_2-18 g powder. It is known that the electrocatalytic activity is, besides the crystal structure, also influenced by the morphology and shape of the catalysts. Apart from nanowires, the best performance is reached with materials indicating a nanorod like shape [73][74].

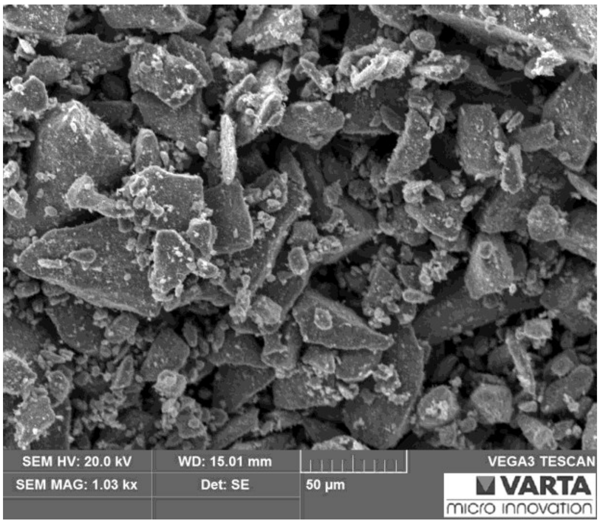

Figure 35: SEM image of unground EMD with a magnification of 1000.

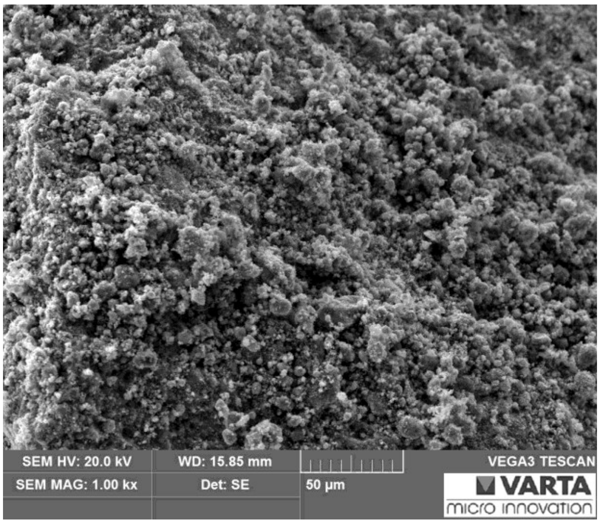

Figure 36: SEM image of ball-milled EMD with a magnification of 1000.

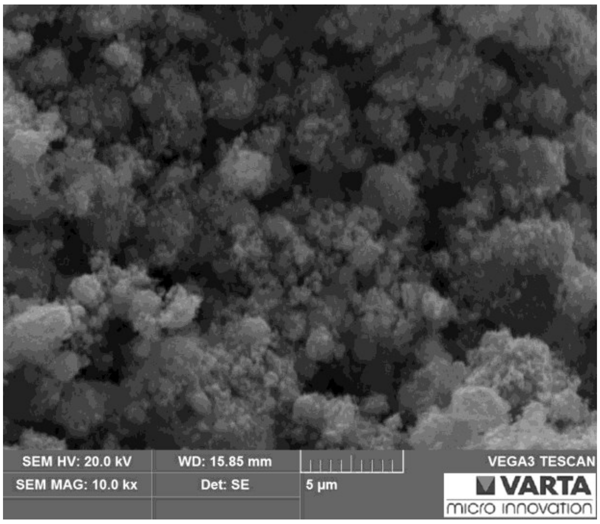

Figure 37: SEM image of ball-milled EMD with a magnification of 10000.

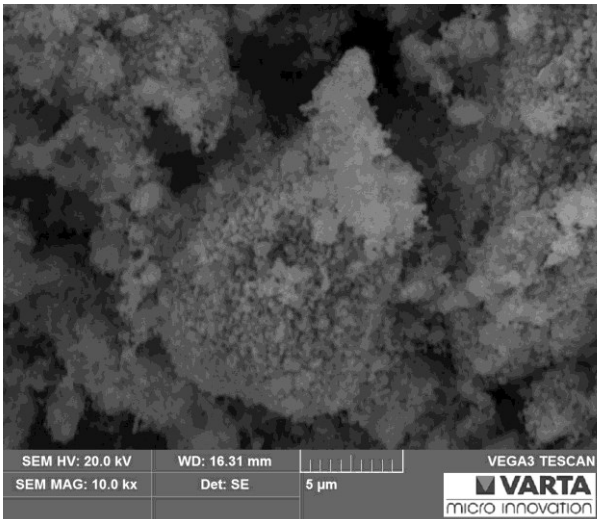

Figure 38: SEM image of Mn_2O_3 *with a magnification of 10000.*

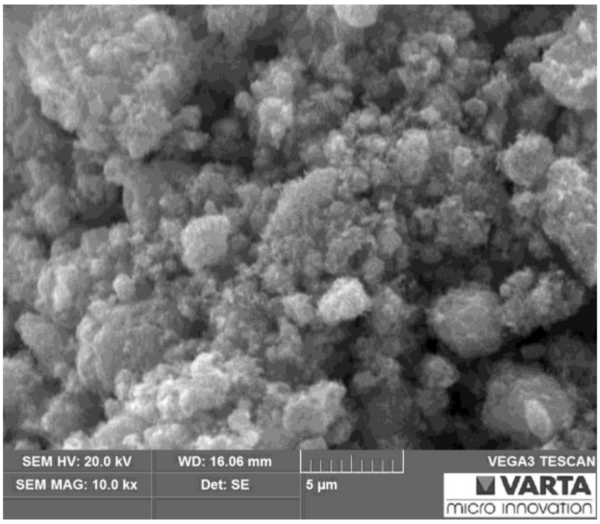

Figure 39: SEM image of α-MnO_2*-10 g with a magnification of 10000.*

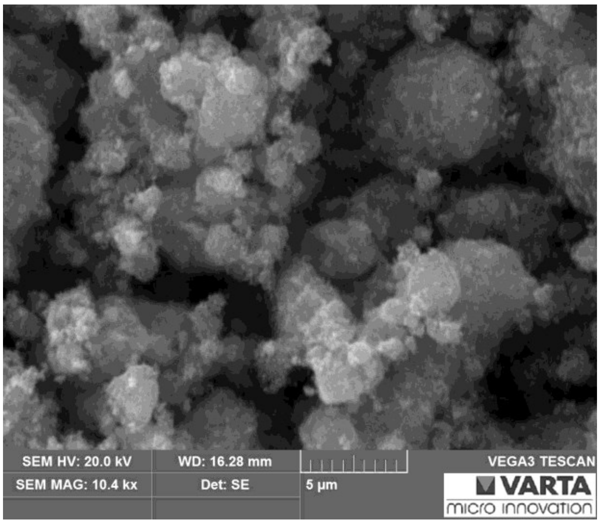

Figure 40: SEM image of α-MnO_2*-18 g with a magnification of 10000.*

The images of the α-MnO_2 samples (Figure 39 and Figure 40) obtained with the ESEM Tescan 500 PA scanning electron microscope give a hint about some nanorods, also described in the work of Mainar et al. [14]. For the confirmation of this suspicion, the morphology is examined with the more precise Zeiss DSM 982 scanning electron microscope. Figure 41 to Figure 44 show even distributed nanorod-like morphologies of the α-MnO_2 catalysts with a length of 200-500 nm and a diameter of a few nanometer. The nanorods of the α-MnO_2-18 g sample appear to be shorter and slightly thinner compared to the 10 g sample.

Compared to α-MnO_2, the images of the $NiCo_2O_4$ spinel analysed by Birgit Krenn, show particles with a more plate like shape and larger agglomerates (not shown here) [15].

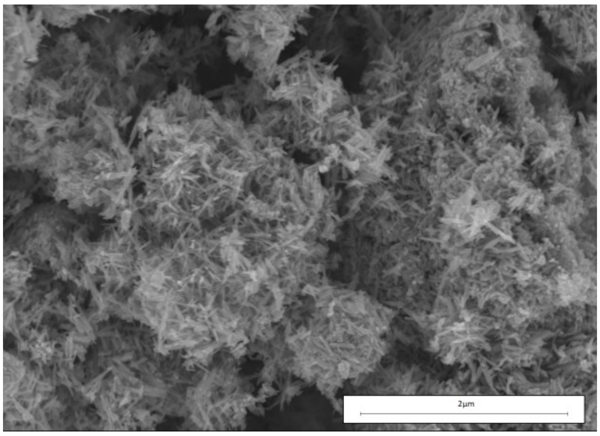

Figure 41: SEM image of α-MnO_2-10 g with Zeiss DSM 982 microscope.

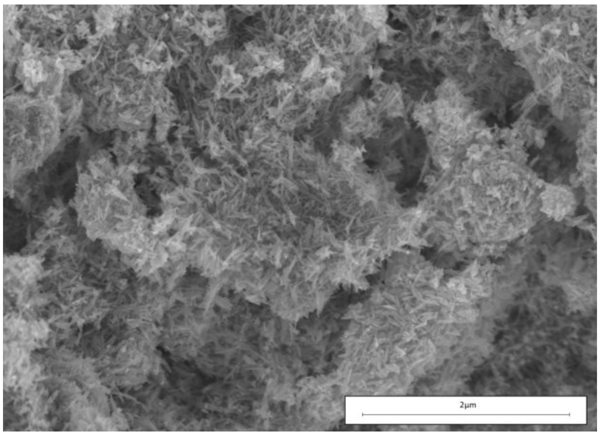

Figure 42: SEM image of α-MnO_2-18 g with Zeiss DSM 982 microscope.

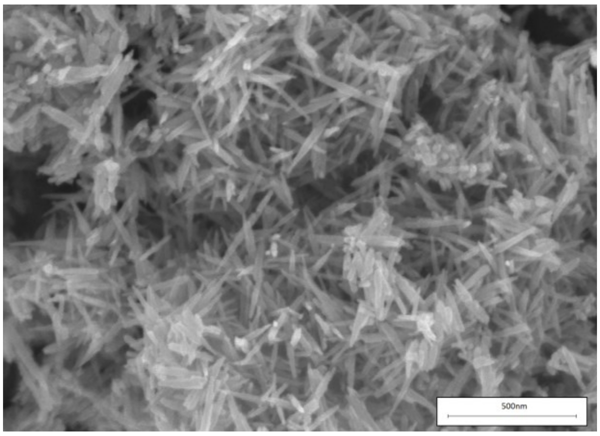

Figure 43: SEM image of α-MnO_2-10 g with Zeiss DSM 982 microscope.

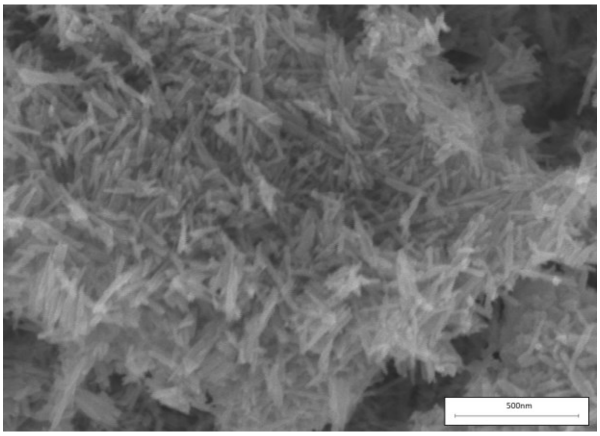

Figure 44: SEM image of α-MnO_2-18 g with Zeiss DSM 982 microscope.

4.1.3 Energy dispersive X-ray spectroscopy

The mean values of the chemical composition of various manganese oxides (EMD, Mn_2O_3, α-MnO_2-18 g and α-MnO_2-10 g) are presented in Table 3 and Table 4. EDX-spectra are obtained from three different areas of the sample surface. The results are given in atomic and weight percent. The outcome of this measurement yielded that all four samples mainly consist of manganese and oxygen. In addition, a small amount of sulphur is observed what can be attributed to the sample preparation. The starting material EMD and Mn_2O_3 show the same amount of sulphur (approx. 0.3 %). After the acid digestion process, the sulphur content is three to four times higher in case of both α-MnO_2 products (~1.3 %). The atomic ratios of Mn:O in the manganese dioxide samples deviates from the theoretical values, but it has to be pointed out, that EDX is only a semi quantitative method. Both α-MnO_2 samples show a higher amount of oxygen (1:3) as theoretically expected (1:2). The higher content of oxygen is possibly caused by the presence of sulphate ions from the acid digestion. Furthermore, crystal water may also have some impact on the atomic ratio. In contrast, the atomic ratio of Mn to O is inexplicably found out to be 1:1 in the case of EMD. Unlike with EMD and α-MnO_2, the atomic ratio of Mn_2O_3 (1:1.5) correspond with theory. Additionally, intercalation of protons like Li^+, Na^+ or K^+ into the tunnels of the alpha manganese dioxides during the synthesis, as described in literature [75], can be ruled out because no elements of this kind are detected.

Table 3: Chemical composition (atomic %) of EMD, Mn_2O_3, α-MnO_2-18 g and α-MnO_2-10 g examined by EDX measurements.

	EMD [atomic%]	**Mn_2O_3 [atomic%]**	**α-MnO_2-18 g [atomic%]**	**α-MnO_2-10 g [atomic%]**
Mn	40.6 ± 5.9	40.7 ± 4.5	24.3 ± 9.4	26.4 ± 1.8
O	49.1 ± 5.8	59.0 ± 4.5	74.6 ± 9.8	72.6 ± 1.8
S	0.34 ± 0.1	0.27 ± 0.1	1.18 ± 0.4	1.01 ± 0.1

Table 4: Chemical composition (weight %) of EMD, Mn_2O_3, α-MnO_2-18 g and α-MnO_2-10 g examined by EDX measurements.

	EMD [weight%]	**Mn_2O_3 [weight%]**	**α-MnO_2-18 g [weight%]**	**α-MnO_2-10 g [weight%]**
Mn	77.5 ± 4.1	70.0 ± 4.1	50.7 ± 13.8	54.8 ± 2.3
O	22.1 ± 4.1	29.8 ± 4.0	47.9 ± 14.2	44.0 ± 2.2
S	0.32 ± 0.1	0.28 ± 0.1	1.44 ± 0.3	1.22 ± 0.1

4.1.4 Brunauer-Emmett-Teller and Barrett-Joyner-Halenda measurements

The results of the BET and BJH measurements are summarized in Table 5. Nitrogen adsorption and desorption isotherms of EMD, Mn_2O_3, α-MnO_2-18 g and α-MnO_2-10 g are illustrated in Figure 45. It is known from literature that higher surface area indicates better electrochemical performance due to the fact that more active sites for the oxygen adsorption are available [13][31][48]. The specific surface area (SSA) can be influenced by many factors as for example sample synthesis or the sintering process. The BET results show that a relative high SSA of EMD (44.96 m^2/g) is drastically reduced after heat treatment (3.29 m^2/g for Mn_2O_3). This also correlates with a much smaller pore volume of the sintered product (0.01 cm^3/g) compared to the porous EMD sample (0.14 cm^3/g). After acid digestion and formation of alpha manganese dioxides, the specific surface area is significantly increased again. The SSA of α-MnO_2-18 g (60.57 m^2/g) is higher than that of the α-MnO_2-10 g sample (54.65 m^2/g). These results correlate with the pore volume and pore diameter what strengthens the fact that a higher pore volume leads to higher specific surface area. The specific surface areas of this work are comparable with those of Mainar et al. [14]. The $NiCo_2O_4$ spinel shows a slightly smaller SSA (49.00 m^2/g) than the α-MnO_2 catalysts.

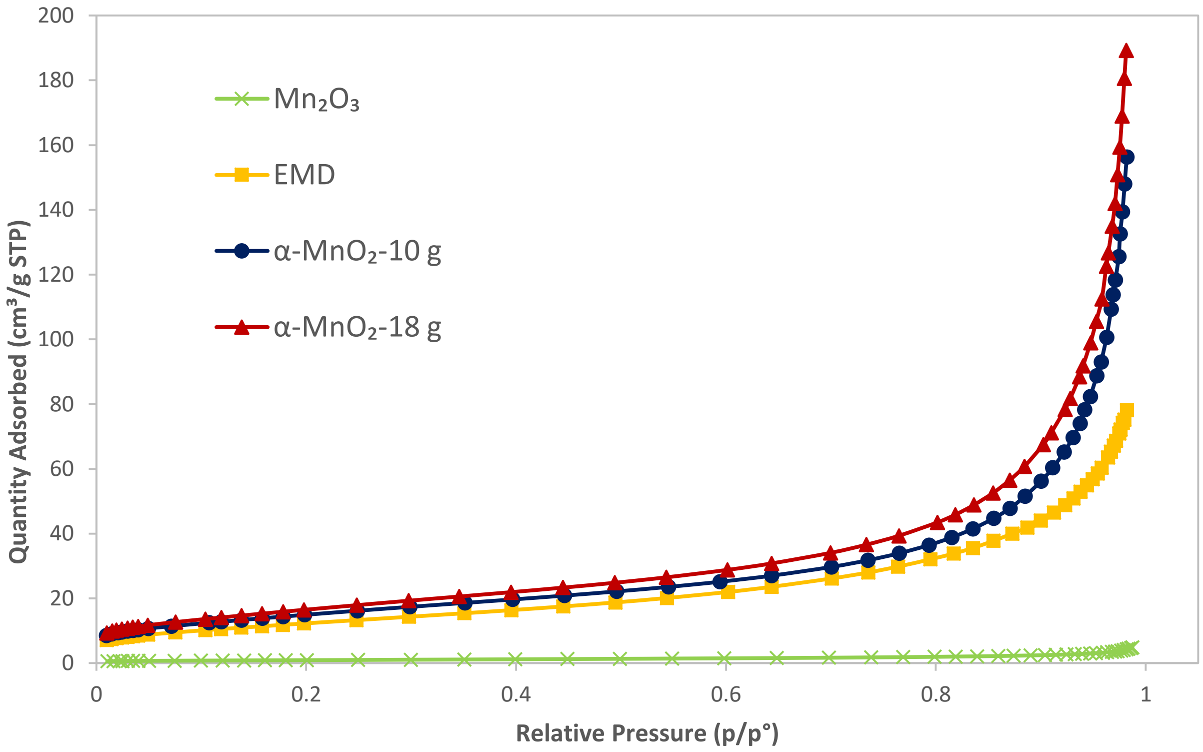

Figure 45: Nitrogen adsorption and desorption isotherms of various manganese oxides at standard temperature and pressure (STP).

Table 5: Calculated pore volume, diameter and specific surface area (SSA) compared with literature [14].

Sample	Pore volume [cm^3/g]	Pore diameter [nm]	SSA [m^2/g]	SSA [14] [m^2/g]
EMD	0.14	10.71	44.96	34.15
Mn_2O_3	0.01	11.89	3.29	3.33
α-MnO_2-18 g	0.38	21.19	60.57	67.36
α-MnO_2-10 g	0.32	21.01	54.65	55.58
$NiCo_2O_4$	-	-	49.00 [15]	-

4.1.5 Structural and surface water content

Table 6 shows the experimental values of α-MnO_2-18 g and α-MnO_2-10 g, which are used for the calculation of the surface (physically adsorbed) and structural (chemically bond) water content according to equation (27) and (28), given in the theory part.

Table 6: Data for the calculation of surface and structural water content.

	α-MnO_2-18 g [mg]	α-MnO_2-10 g [mg]
m0	500.7	499.3
m1	493.7	495.6
m2	472.8	472.9

The results compared with literature can be seen in Table 7. The content of physically adsorbed water is twice as high in the α-MnO_2-10 g (1.4 %) sample as in the α-MnO_2-18 g sample (0.7 %). Additionally, a lower portion of surface water compared to structural water is observed. In general, the surface water content is depending on the BET-surface area. A higher available surface is related to a higher content of physically adsorbed water, thus the sample with higher SSA (α-MnO_2-18 g) should provide a higher surface water content. But physically adsorbed water may also be desorbed only by applying vacuum [57]. Therefore, the contrary results in this study can be traced back to the initial drying step in the desiccator. Additionally, the experiment was carried out after the catalysts were stored in the desiccator for a long period. Furthermore, the content of the chemically bond water is nearly the same for both samples (α-MnO_2-18 g: 4.6 %; α-MnO_2-10 g: 4.3 %). The results do not correlate with those of Mainar et al. [14].

Table 7: Surface and structural water content of α-MnO_2-10 g and α-MnO_2-18 g compared with the results of Mainar et al. [14].

Sample	surface water [%]	structural water [%]
α-MnO_2-18 g	0.7	4.6
α-MnO_2-18 g [14]	19.80	2.74
α-MnO_2-10 g	1.4	4.2
α-MnO_2-10 g [14]	4.70	7.28

4.2 Electrochemical measurements

4.2.1 Cyclic voltammetry

For the investigation of the reduction and oxidation processes of the α-MnO_2, $NiCo_2O_4$ and mixed catalysts, cyclic voltammetry (CV) experiments are carried out in N_2 saturated 0.1 M and 8 M KOH at a scan rate of 10 mV s^{-1}. Figure 46 and Figure 47 present the CVs of both pure α-MnO_2 samples and the marked regions indicate the different manganese oxide phases formed during cycling, as described in literature [12][76–79]. In a first step, MnO_2 is reduced to MnOOH ($MnO_2 + H_2O + e^- \leftrightarrow MnOOH + OH^-$) and in lower potential regions, it is reduced to either Mn_2O_3 or Mn_3O_4. In a further reduction step, the Mn(II) species form $Mn(OH)_2$ in higher concentrated solutions [12]. Afterwards, the reduction products will be re-oxidised first of all to Mn_2O_3 and MnOOH that should be finally converted back to MnO_2. In the case of 8 M KOH solution, all reduction peaks can be associated with such species and the oxidation peaks of the Mn_2O_3 and MnOOH formation can also be detected but there is no oxidation of these two species to MnO_2. Furthermore, the reduction peaks in 0.1 M KOH electrolyte solution can be linked to the formation of MnOOH, whereas no significant peak at approx. -0.4 V, characteristic for the formation of Mn_2O_3 or Mn_3O_4, is obtained. The oxidation peak at ~0.15 V can be attributed to the re-oxidation of MnOOH to MnO_2. No reduction peak for the $Mn(OH)_2$ formation as well as for the oxidation to Mn_2O_3 is obtained. Additionally, in 8 M KOH electrolyte solution higher peak current densities are observed for the α-MnO_2-10 g sample compared to α-MnO_2-18 g, in 0.1 M KOH they are quite similar.

The cyclic voltammograms of the $NiCo_2O_4$ spinel in 8 M and 0.1 M KOH are presented in Figure 48 and Figure 49. The anodic profile of the second cycle depicts two sharp peaks in the higher concentrated electrolyte and one broad, composed of two overlapping peaks, for the diluted solution. The oxidation peak at ~0.2 V can be attributed to the redox couple Co(II)/Co(III). Due to the fact that no corresponding reduction peak is observed and the oxidation peak decreases with increasing cycle number, the process is irreversible. The second oxidation/reduction peak at ~0.45 V may be attributed to Ni(II)/Ni(III) and Co(III)/Co(IV). The peak current density of these peaks increases from the second to the tenth cycle [80–83].

Figure 50 to Figure 53 show the voltammograms of the mixed α-MnO_2-18 g/$NiCo_2O_4$ and α-MnO_2-10 g/$NiCo_2O_4$ samples in comparison with the individual catalysts in 8 M and 0.1 M KOH electrolyte solution. The CVs of the mixed catalysts show a combination of the oxidation and reduction peaks of the pure α-MnO_2 and $NiCo_2O_4$ samples. The small oxidation peaks of the curves in 8 M KOH at approx. -0.3 V can be associated with the formation of Mn_2O_3 and the one at ~0.45 V to the oxidation of Ni(II) and Co(III). The broad oxidation peaks at ~0 V may be a combination of the MnOOH formation of the α-MnO_2 and the oxidation of Co(II) of the spinel. The cathodic profile depicts small Ni(III) and Co(IV) reduction peaks at ~0.3 V. All other reduction peaks are attributed to MnO_2. These reduction peaks are also observed in 0.1 M KOH whereas the anodic profile shows just one broad peak at ~0.25 V composed of Co(II), Co(III), Ni(II) oxidation and formation of MnO_2. The sample mixed in a ratio of 1:1 with double amount of catalyst shows the highest current density range followed by the 1:1 and the 4:1 mixed one in all cases, except for the voltammograms of the catalysts containing α-MnO_2-10 g in 8 M KOH, where the current density of the 4:1 sample is higher than the 1:1. Furthermore, the current density range of the pure $NiCo_2O_4$ spinel is significantly lower compared to the one of the samples containing α-MnO_2.

Figure 54 and Figure 55 show the cyclic voltammograms of the pure electrode with/without Nafion and of the carbon powder XC-72 plus Nafion in 8 M and 0.1 M KOH. The current density of the pure electrode is slightly higher compared to the electrode coated with Nafion. Additionally, the voltammogram of the pure electrode in 8 M KOH shows a reduction peak at approx. -0.4 V that can be attributed to reactions of the glassy carbon electrode [84]. The coating of the electrode with XC-72 and Nafion generally leads to a slightly higher current density. It is also higher in 8 M than in 0.1 M potassium hydroxide solution. Furthermore, the electrodes coated with catalysts show a significantly higher current density compared to the pure electrode with/without Nafion and to that coated with XC-72 plus Nafion (Figure 56 and Figure 57).

Figure 58 to Figure 63 show the results of 100 voltammetric cycles in 8 M KOH to evaluate the long term stability of the pure α-MnO_2-18 g, the pure $NiCo_2O_4$ and the mixed catalyst. The reduction and oxidation peaks of the pure α-MnO_2-18 g catalyst (Figure 58) drastically decrease within the first 10 cycles. Afterwards, the current density only slightly decreases with increasing cycle number (Figure 59). In the case of the pure $NiCo_2O_4$, the reduction peak at ~0.25 V and the oxidation peak at ~0.45 V increase until the 10th cycle (Figure 60). Afterwards, the peak current density decreases and the anodic peak at ~0.45 V is shifted anodically between cycle 10 to 100 (Figure 61). In contrast, the oxidation peak at ~0.2 V continuously decreases with increasing cycle number. Additionally, the $NiCo_2O_4$ voltammogram shows a reduction peak at approx. -0.6 V in the first cycle (Figure 60). Several experiments are carried out to check the origin of this peak. At first, the potential is initially ramped in the negative direction to check if the formation of the peak is linked to oxidation processes prior to reduction. Nevertheless, the peak can be observed again in the first cycle. This peak also arises if the upper vertex potential is chosen to be 0.2 V to exclude $NiCo_2O_4$ reduction/oxidation. Therefore, an irreversible surface reaction is assumed. For the mixed catalyst (Figure 62 and Figure 63), the peak current density increases until the 30th cycle and afterwards, it slowly decreases with each cycle.

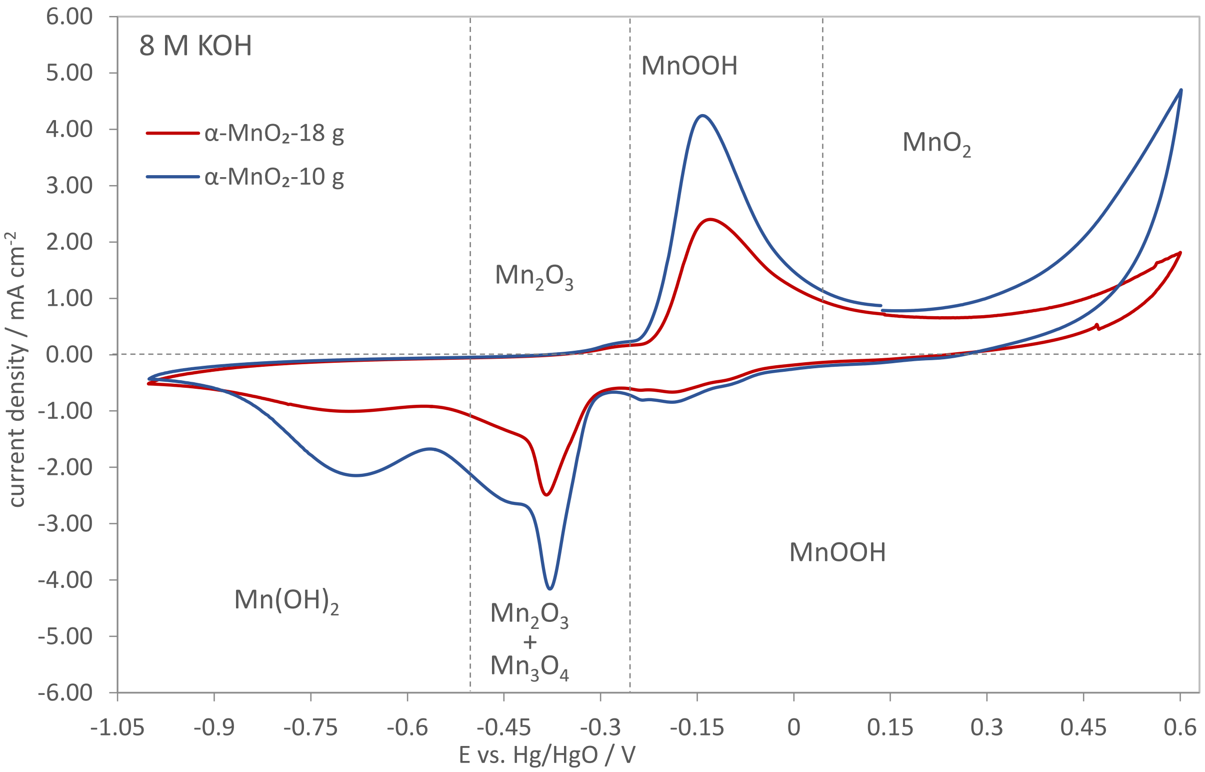

Figure 46: Cyclic voltammograms of α-MnO_2 samples in N_2 saturated 8 M KOH at RT with a scan rate v of 10 mV s-1 (cycle 2) compared with literature.

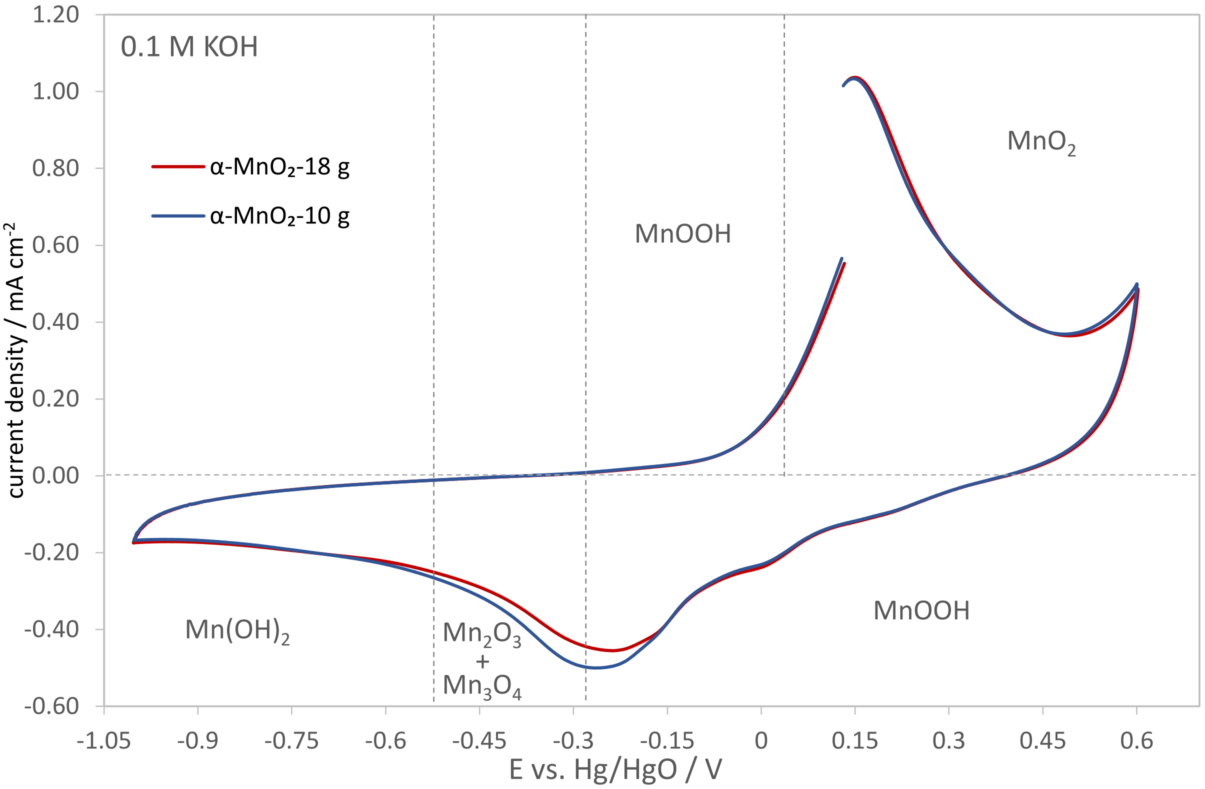

Figure 47: Cyclic voltammograms of α-MnO_2 samples in N_2 saturated 0.1 M KOH at RT with a scan rate v of 10 mV s^{-1} (cycle 2) compared with literature.

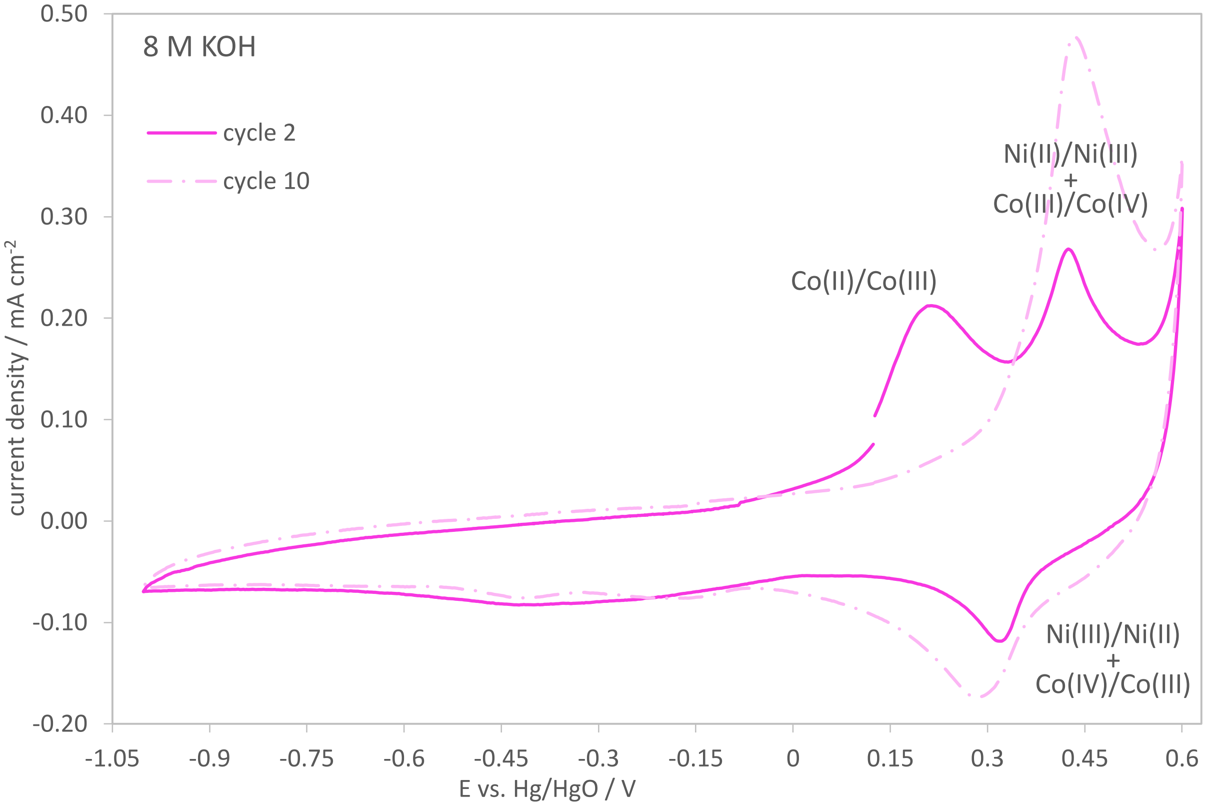

Figure 48: Cyclic voltammograms of $NiCo_2O_4$ spinel in N_2 saturated 8 M KOH at RT with a scan rate v of 10 mV s^{-1} at different cycle numbers.

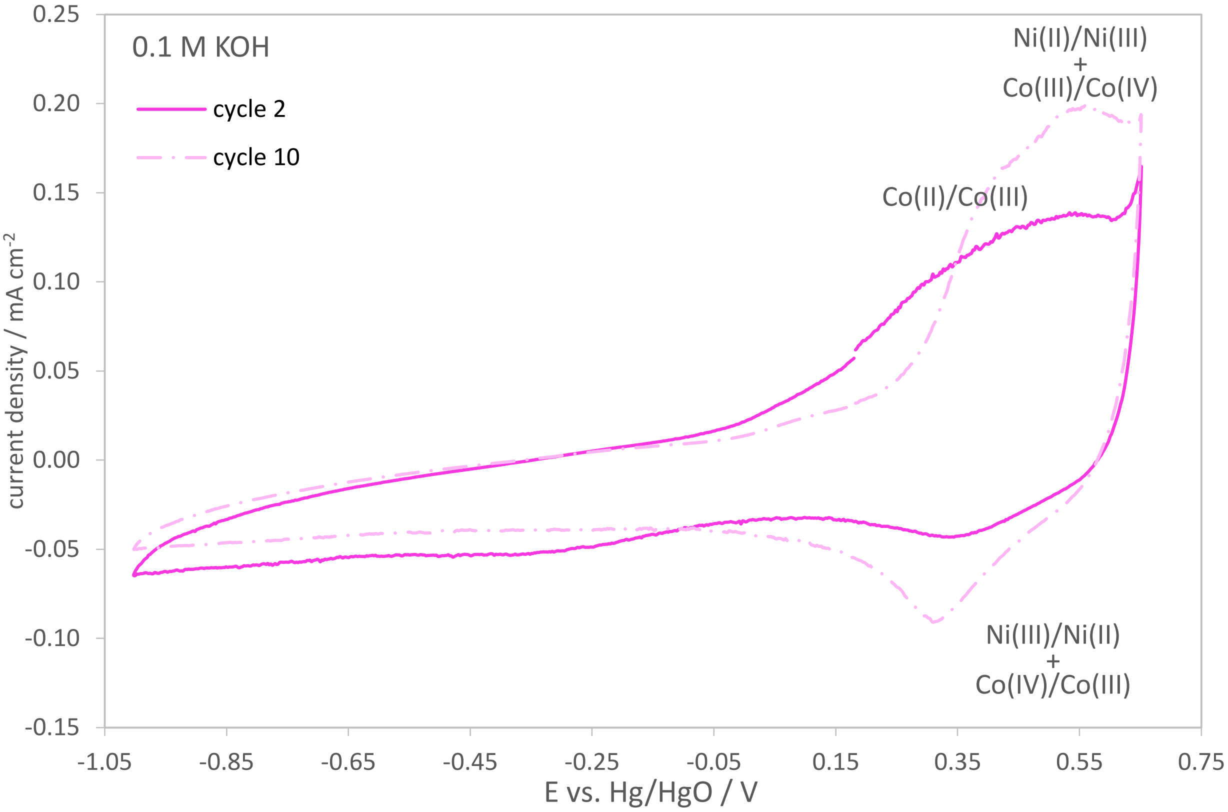

Figure 49: Cyclic voltammograms of $NiCo_2O_4$ spinel in N_2 saturated 0.1 M KOH at RT with a scan rate v of 10 mV s^{-1} at different cycle numbers.

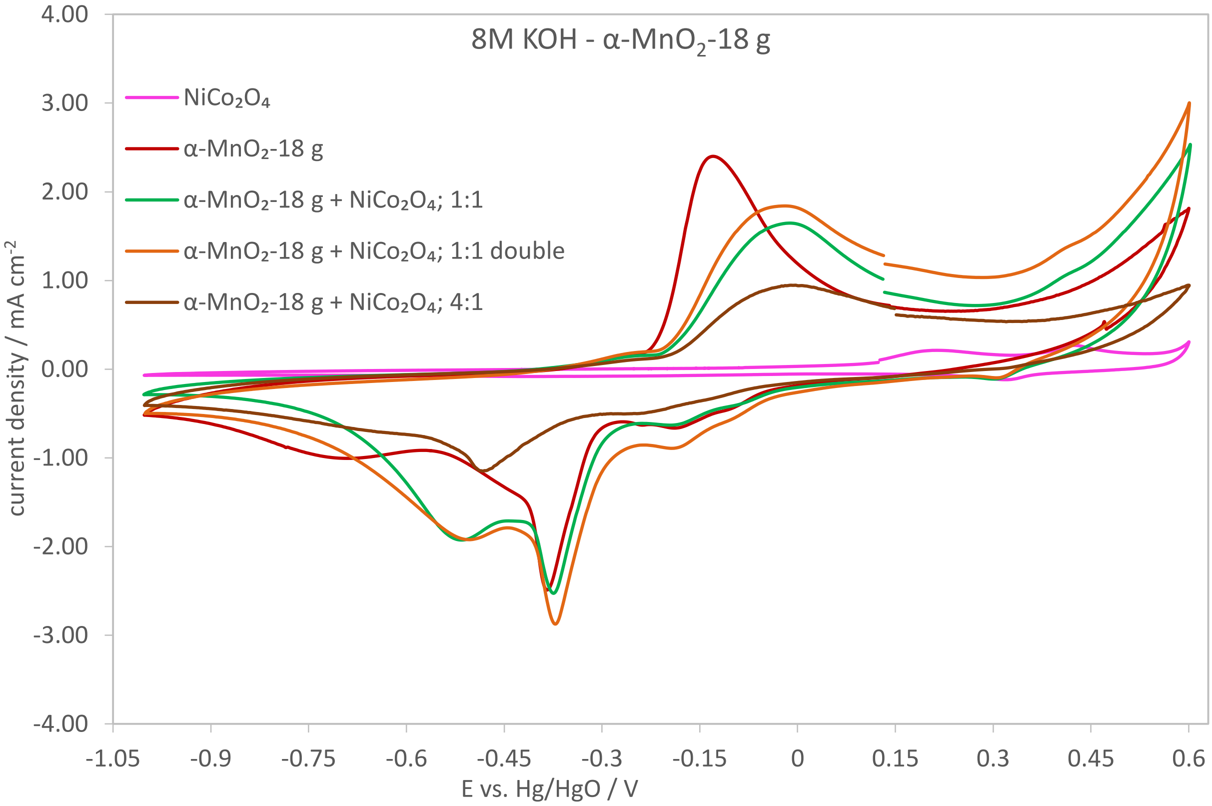

Figure 50: Cyclic voltammograms of α-MnO_2-18 g, $NiCo_2O_4$ spinel and mixed catalysts in N_2 saturated 8 M KOH at RT with a scan rate v of 10 mV s^{-1} (cycle 2).

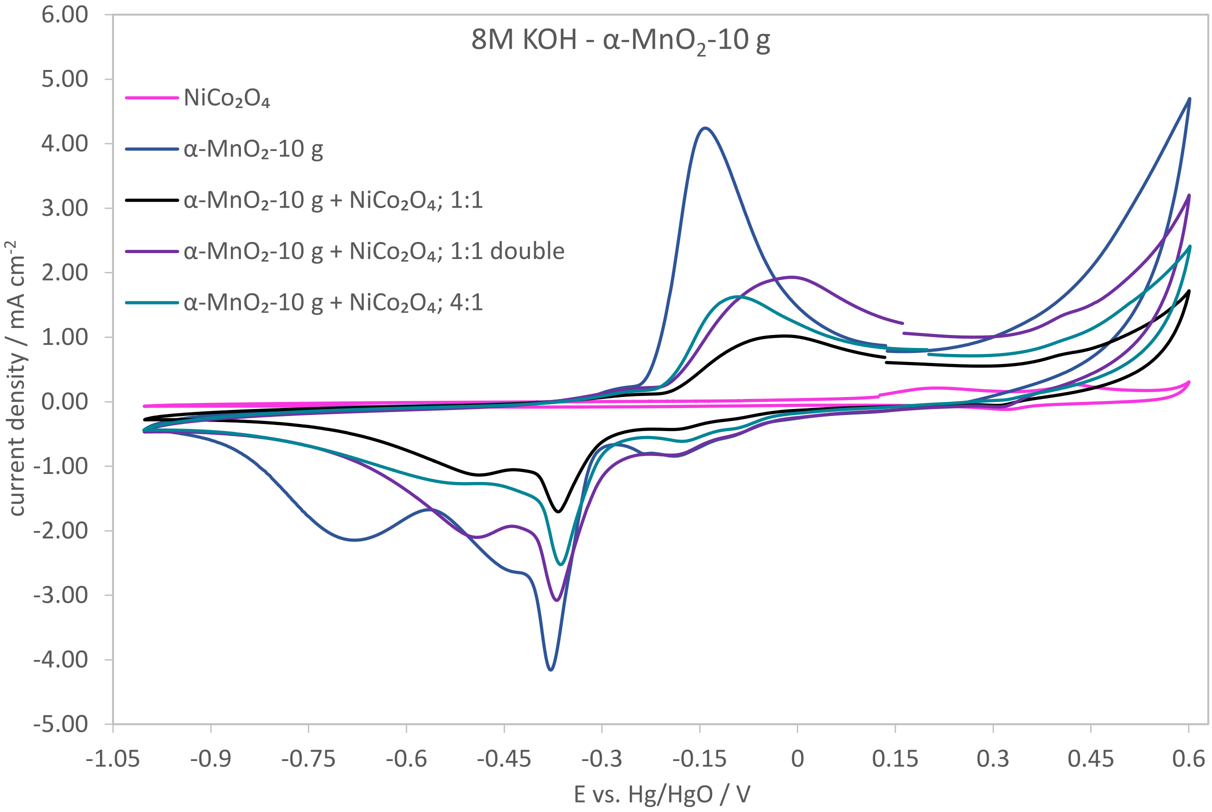

Figure 51: Cyclic voltammograms of α-MnO_2-10 g, $NiCo_2O_4$ spinel and mixed catalysts in N_2 saturated 8 M KOH at RT with a scan rate v of 10 mV s^{-1} (cycle 2).

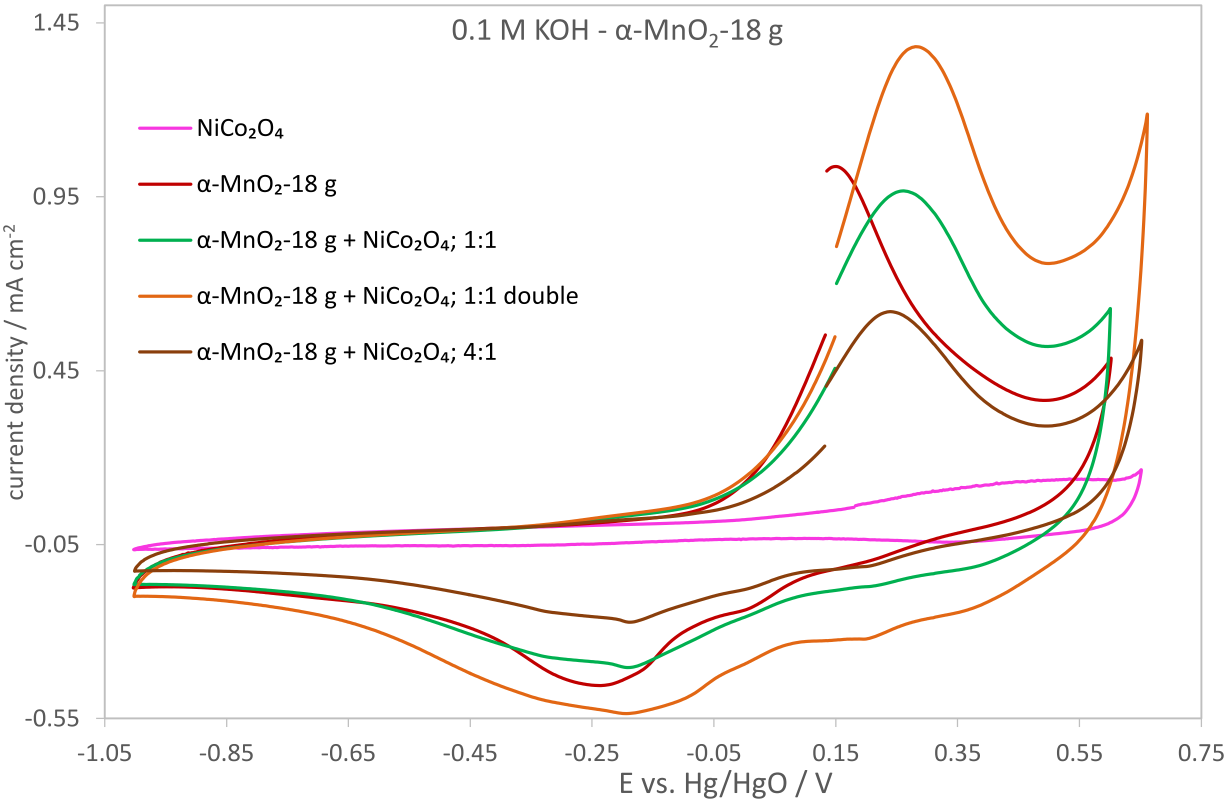

Figure 52: Cyclic voltammograms of α-MnO_2-18 g, $NiCo_2O_4$ spinel and mixed catalysts in N_2 saturated 0.1 M KOH at RT with a scan rate v of 10 mV s^{-1} (cycle 2).

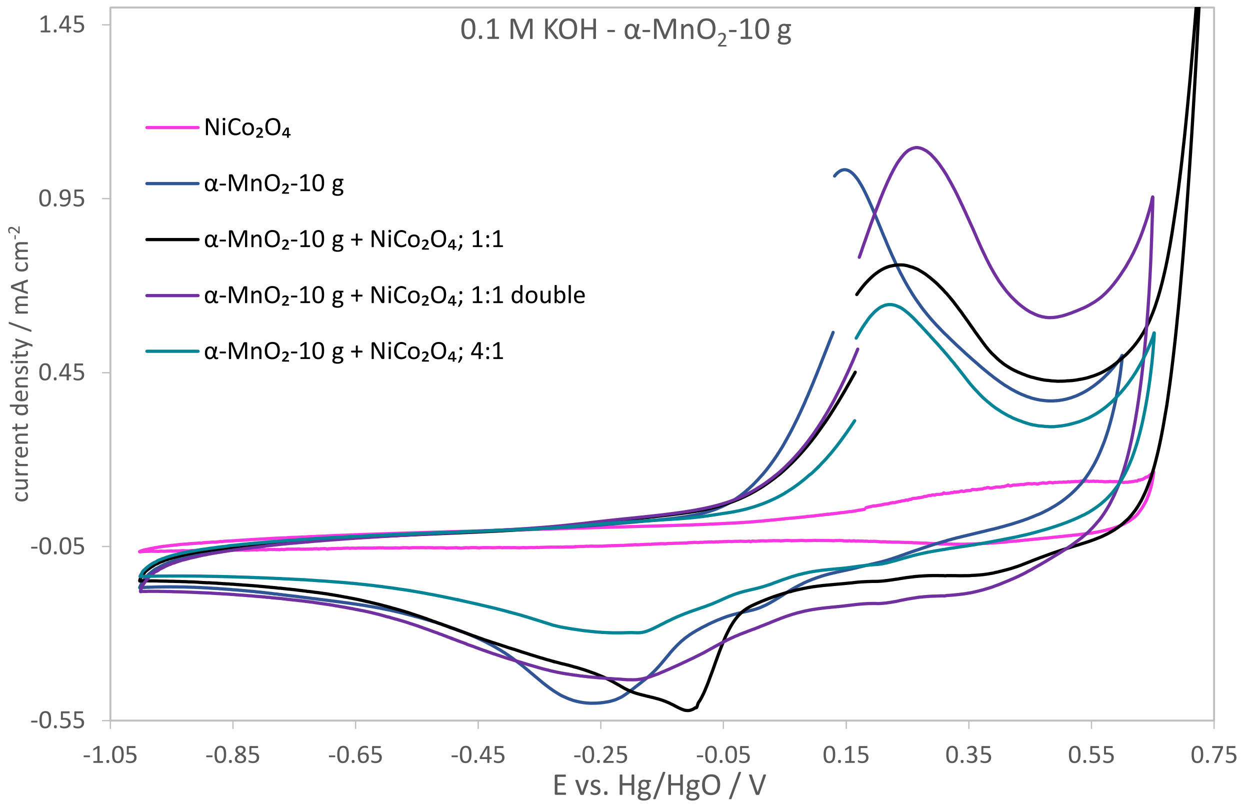

Figure 53: Cyclic voltammograms of α-MnO$_2$-10 g, NiCo$_2$O$_4$ spinel and mixed catalysts in N$_2$ saturated 0.1 M KOH at RT with a scan rate v of 10 mV s^{-1} (cycle 2).

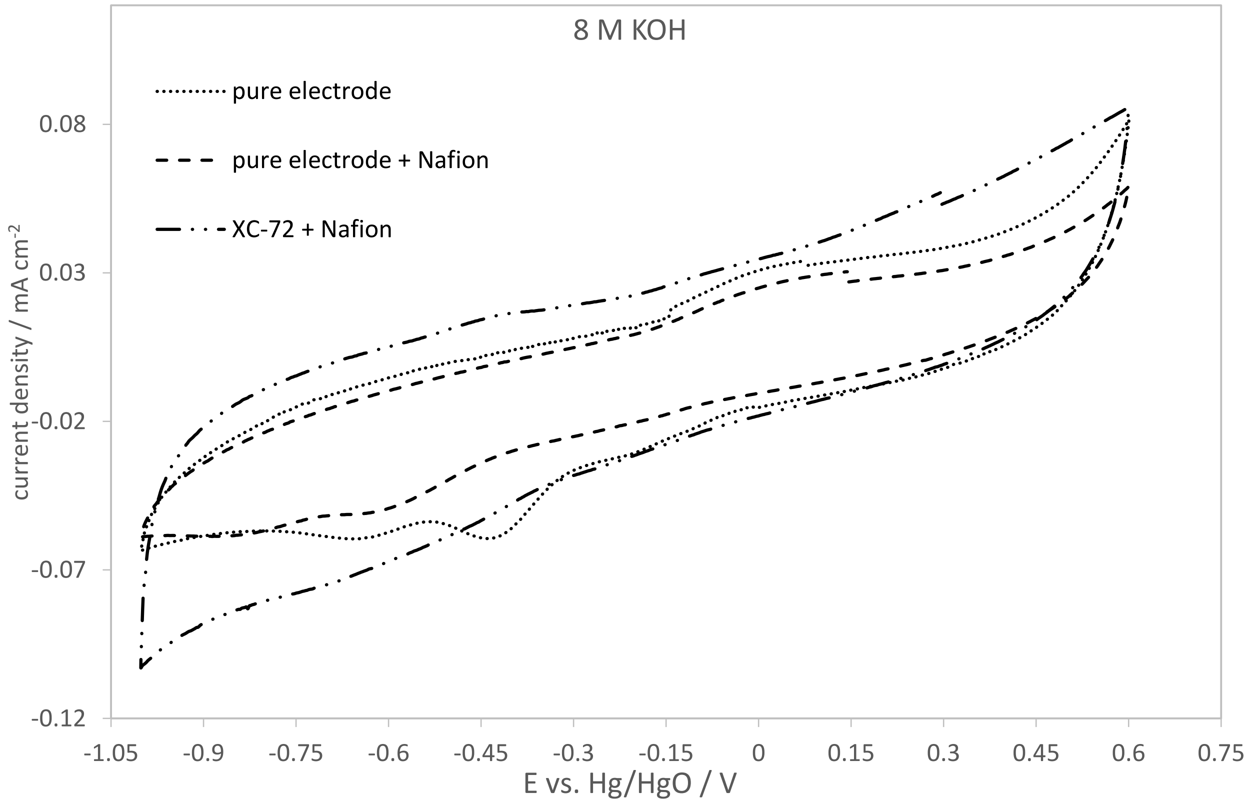

Figure 54: Cyclic voltammograms of the pure electrode with/without Nafion and of XC-72 with Nafion in N$_2$ saturated 8 M KOH at RT with a scan rate v of 10 mV s^{-1} (cycle 2).

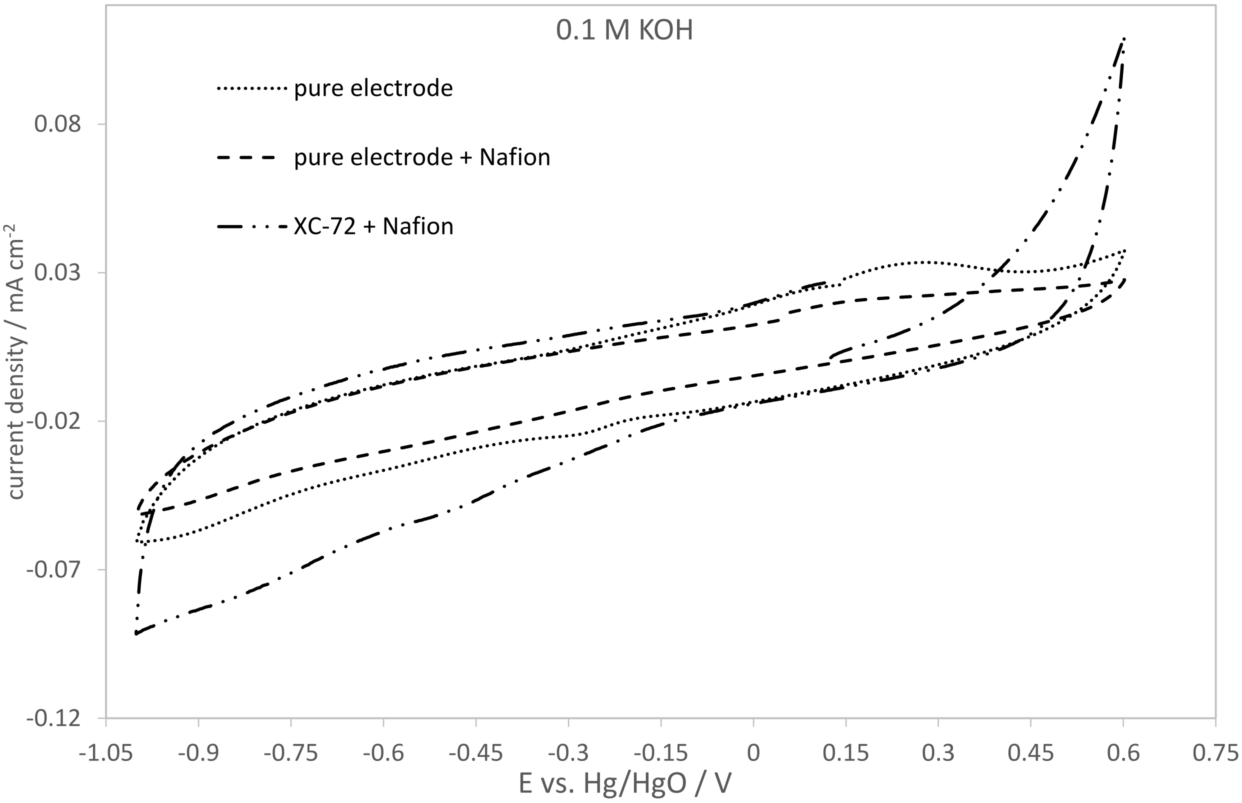

Figure 55: Cyclic voltammograms of the pure electrode with/without Nafion and of XC-72 with Nafion in N_2 saturated 0.1 M KOH at RT with a scan rate v of 10 mV s^{-1} (cycle 2).

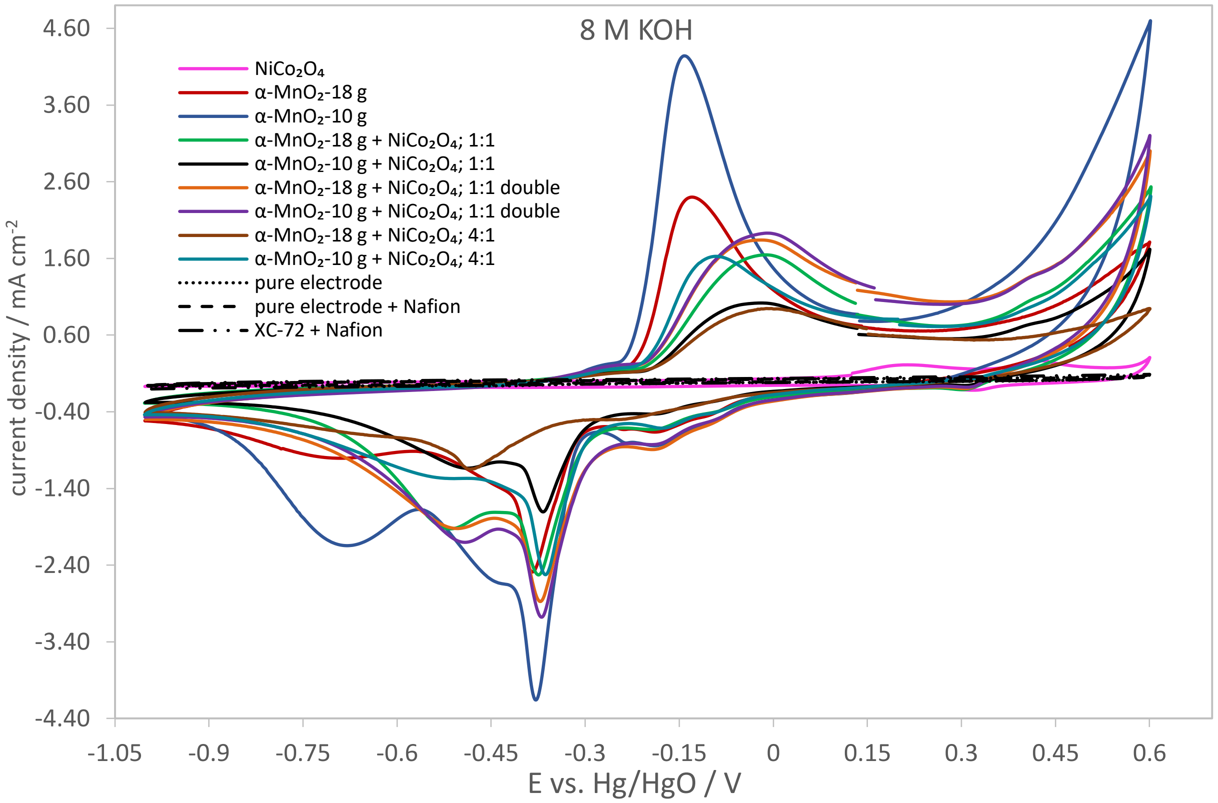

Figure 56: Cyclic voltammograms of α-MnO_2 samples, $NiCo_2O_4$ spinel and mixed catalysts compared with the pure electrode with/without Nafion and of XC-72 with Nafion in N_2 saturated 8 M KOH at RT with a scan rate v of 10 mV s^{-1} (cycle 2).

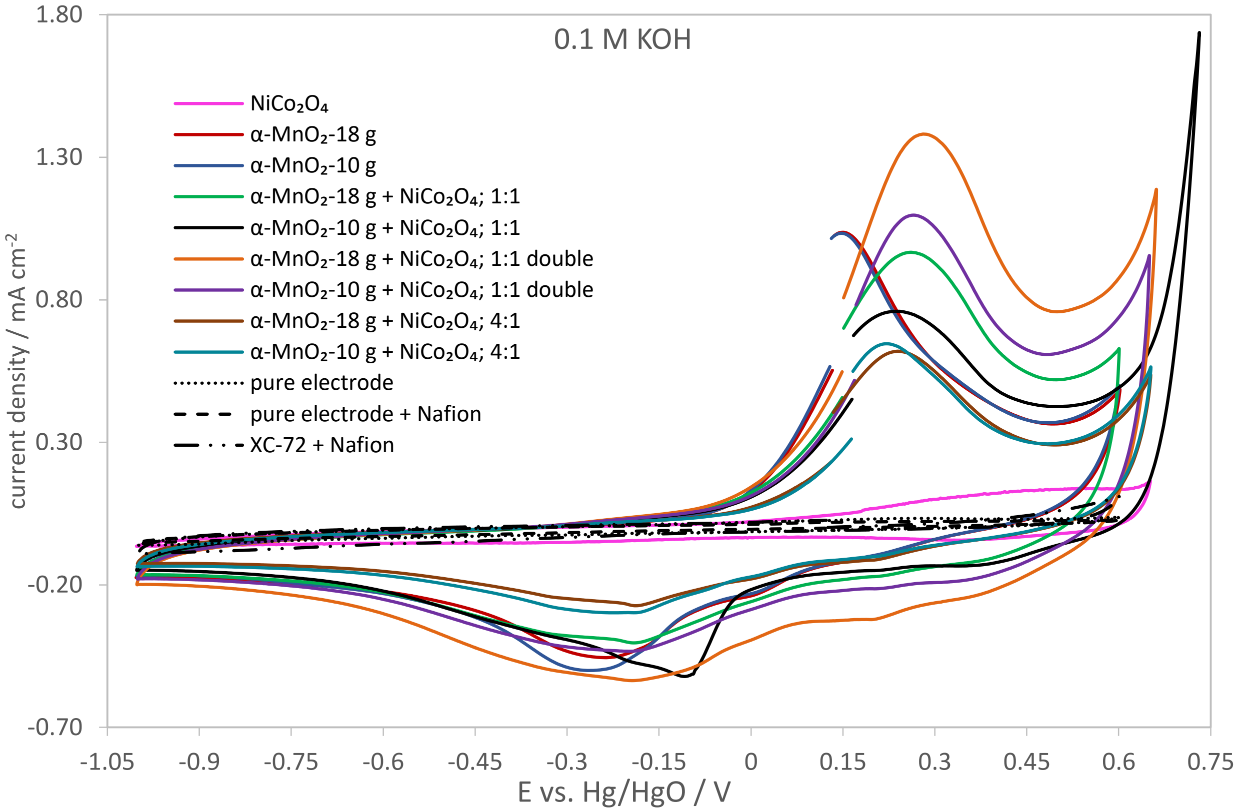

Figure 57: Cyclic voltammograms of α-MnO_2 samples, $NiCo_2O_4$ spinel and mixed catalysts compared with the pure electrode with/without Nafion and of XC-72 with Nafion in N_2 saturated 0.1 M KOH at RT with a scan rate v of 10 mV s^{-1} (cycle 2).

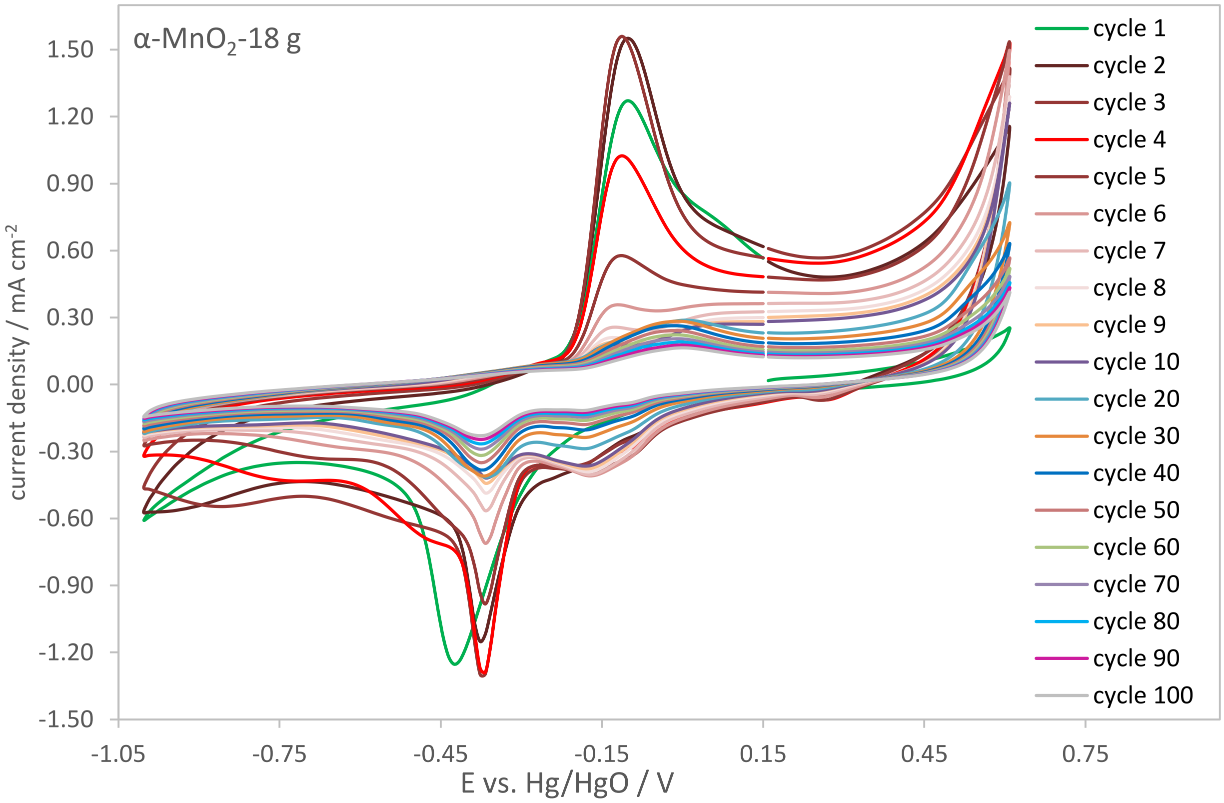

Figure 58: Cyclic voltammograms of α-MnO_2-18 g in N_2 saturated 8 M KOH at RT with a scan rate v of 10 mV s^{-1} for the evaluation of the long term stability of the catalyst (100 cycles).

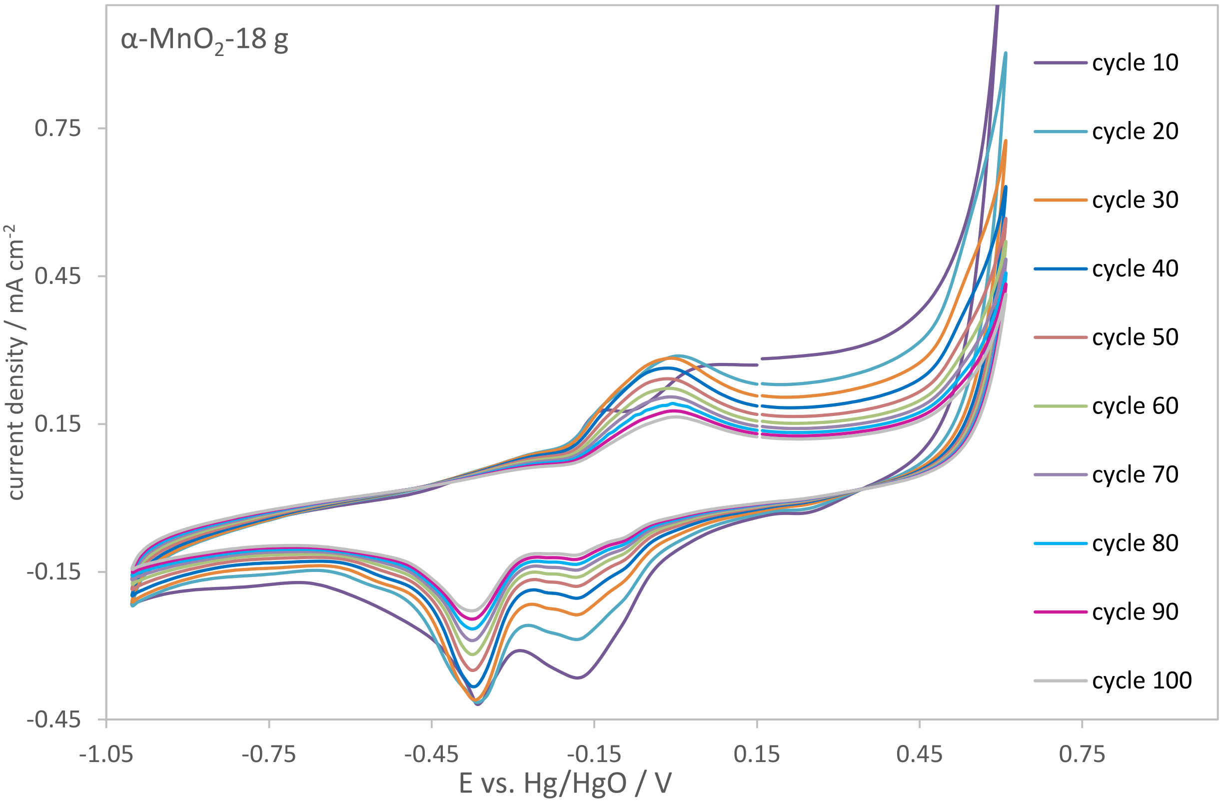

Figure 59: Cyclic voltammograms of α-MnO_2-18 g in N_2 saturated 8 M KOH at RT with a scan rate v of 10 mV s^{-1} for the evaluation of the long term stability of the catalyst (cycle 10 to 100).

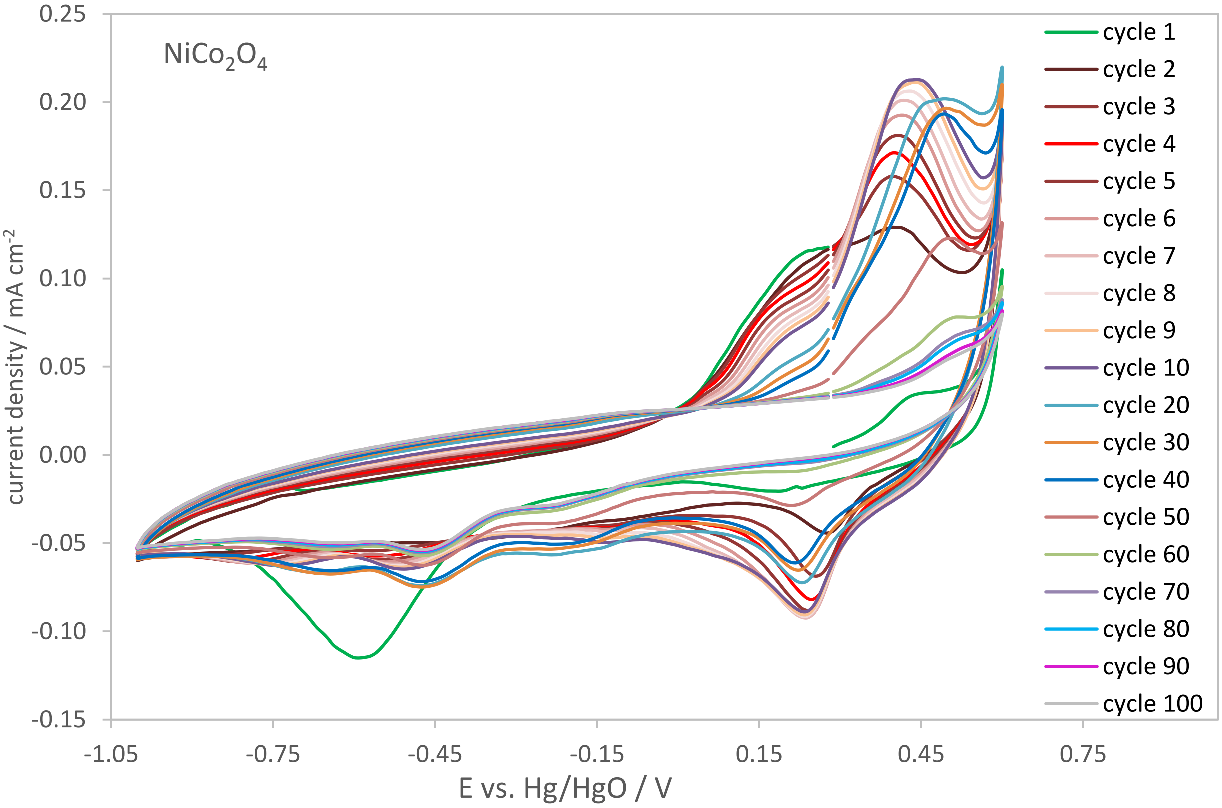

Figure 60: Cyclic voltammograms of $NiCo_2O_4$ in N_2 saturated 8 M KOH at RT with a scan rate v of 10 mV s^{-1} for the evaluation of the long term stability of the catalyst (100 cycles).

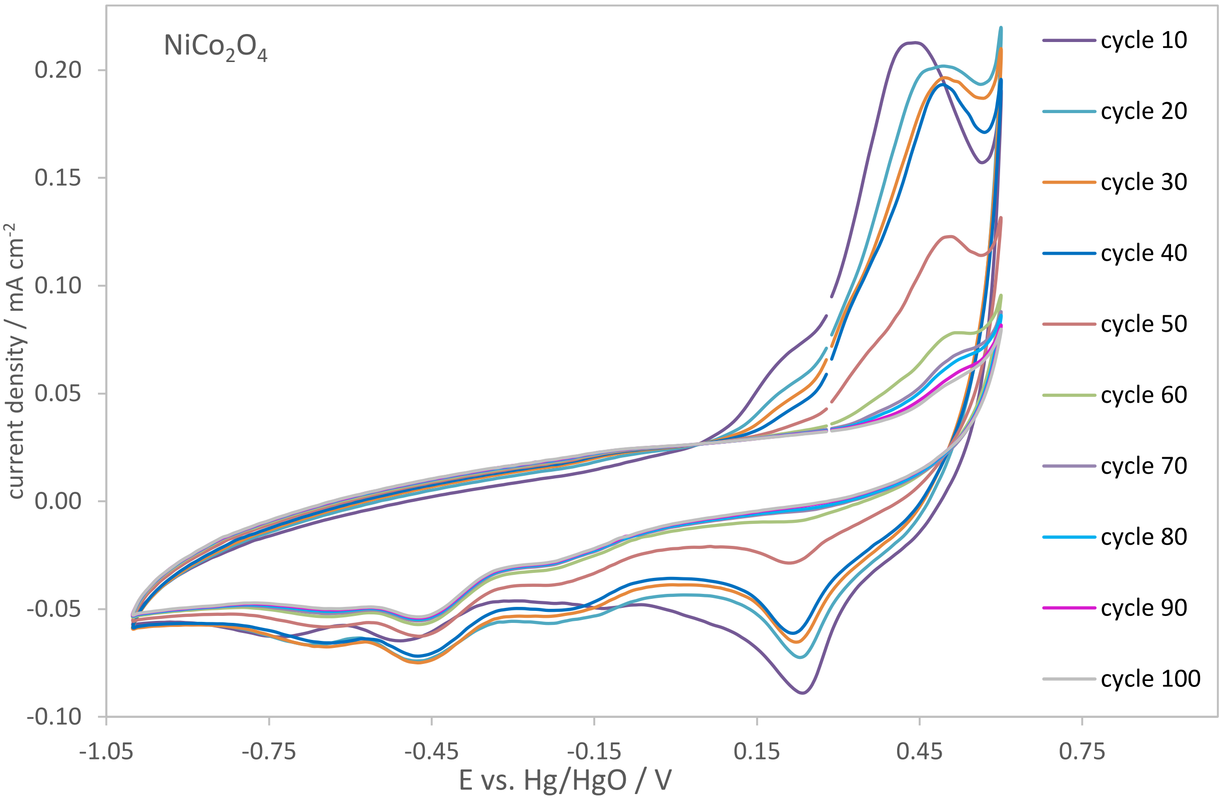

Figure 61: Cyclic voltammograms of $NiCo_2O_4$ in N_2 saturated 8 M KOH at RT with a scan rate v of 10 mV s^{-1} for the evaluation of the long term stability of the catalyst (cycle 10 to 100).

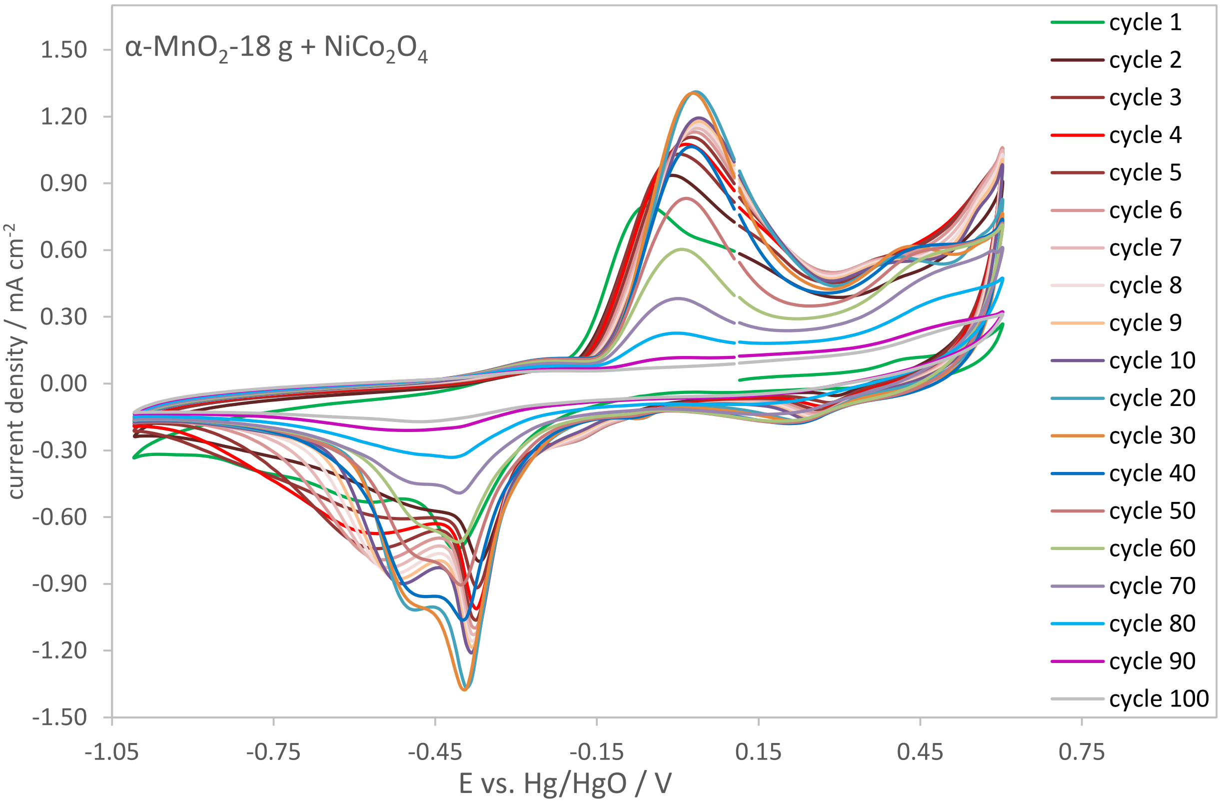

Figure 62: Cyclic voltammograms of mixed catalyt in N_2 saturated 8 M KOH at RT with a scan rate v of 10 mV s^{-1} for the evaluation of the long term stability (100 cycles).

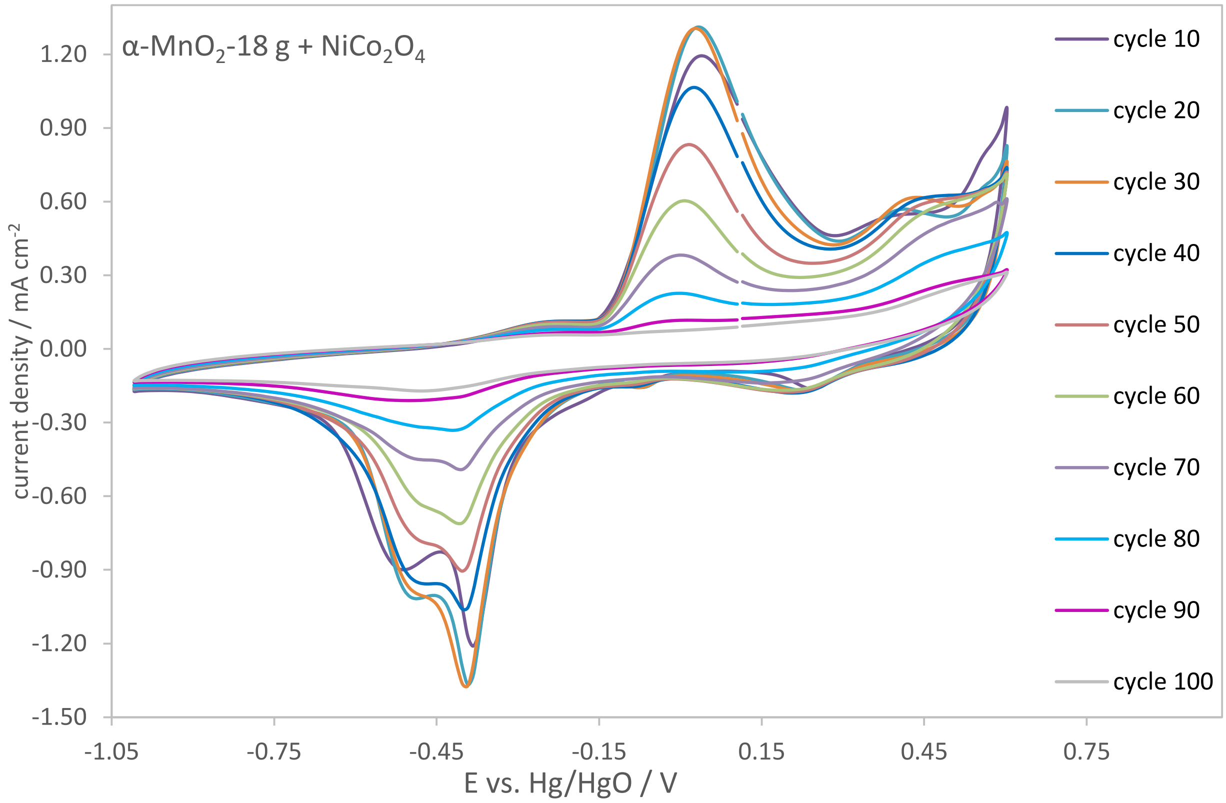

Figure 63: Cyclic voltammograms of mixed catalyst in N_2 saturated 8 M KOH at RT with a scan rate v of 10 mV s^{-1} for the evaluation of the long term stability (cycle 10 to 100).

4.2.2 Oxygen evolution reaction

The voltammograms of the oxygen evolution reaction (OER) of the different samples can be seen in Figure 64 to Figure 69. Figure 64 and Figure 65 demonstrate that the catalysts exhibit significantly lower overpotential in 8 M KOH (~0.6 V) than in 0.1 M KOH (~0.7 V), what can be explained by the higher conductivity and higher OH^- concentration in 8 M KOH. Figure 66 shows a comparison of all catalysts in 8 M KOH. It can be seen that the overpotential of $NiCo_2O_4$ is lower compared to both α-MnO_2 samples. The overpotential of the pure and mixed α-MnO_2-10 g catalyst is lower than that of the α-MnO_2-18 g samples mixed in the same ratio. Furthermore, the mixed catalysts in the 1:1 ratio show improved performances compared to the individual catalysts. The activity of the 4:1 catalysts is in between the one of the pure $NiCo_2O_4$ and the α-MnO_2 catalysts. Additionally, the overpotential of the 1:1 double catalysts is lower than that of the 1:1 samples. The activity of the mixed catalysts in 8 M KOH increases with the total $NiCo_2O_4$ amount (4:1 < 1:1 < 1:1 double). The comparison of all catalysts in 0.1 M KOH can be seen in Figure 67. The overpotential of $NiCo_2O_4$ is in between both α-MnO_2 samples. In addition, the overpotential of the pure α-MnO_2-10 g catalyst is lower than that of the pure α-MnO_2-18 g sample. For the mixed catalysts in 0.1 M KOH, no clear trend can be noticed.

The overpotential of the pure electrode with/without Nafion and of the carbon powder XC-72 is higher in 0.1 M KOH than in 8 M KOH (Figure 68) as also observed for the catalysts. The voltammogram of the electrode coated with Nafion shows a steeper increase in current density compared to the pure electrode but the overpotential is the same. Additionally, the voltammograms of XC-72 with Nafion look similar to those of the pure electrode coated with Nafion. The overpotential of the catalysts is approx. 800 mV lower than that of the pure electrode with/without Nafion and of the carbon powder XC-72 also coated with Nafion (Figure 69).

The best catalyst performance for OER in this work is obtained with the mixed $NiCo_2O_4$/α-MnO_2-10 g (1:1 double) sample in 8 M KOH as electrolyte.

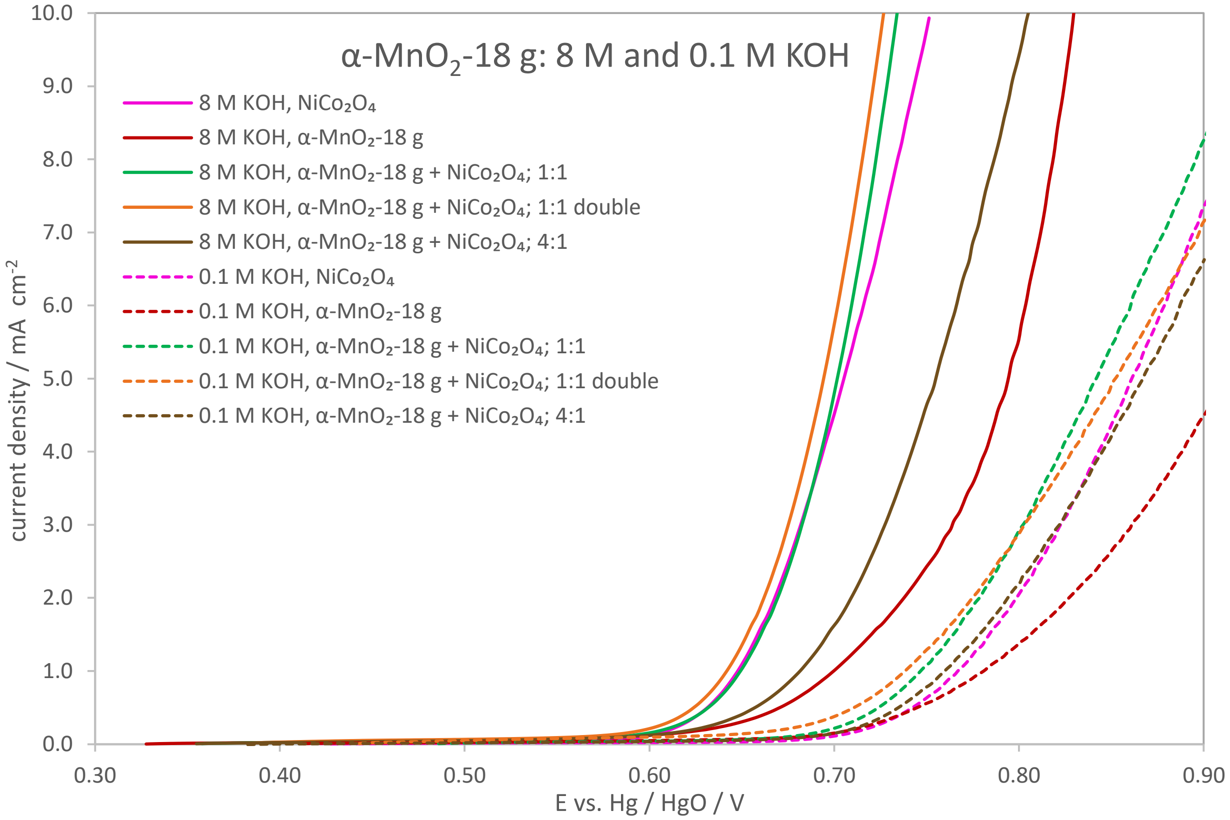

Figure 64: OER voltammograms of $NiCo_2O_4$, α-MnO_2-18 g and mixed catalysts in N_2 saturated 0.1 M and 8 M KOH at RT with a rotation rate ω of 1600 rpm (5th sweep) and a scan rate v of 5 mV s^{-1}.

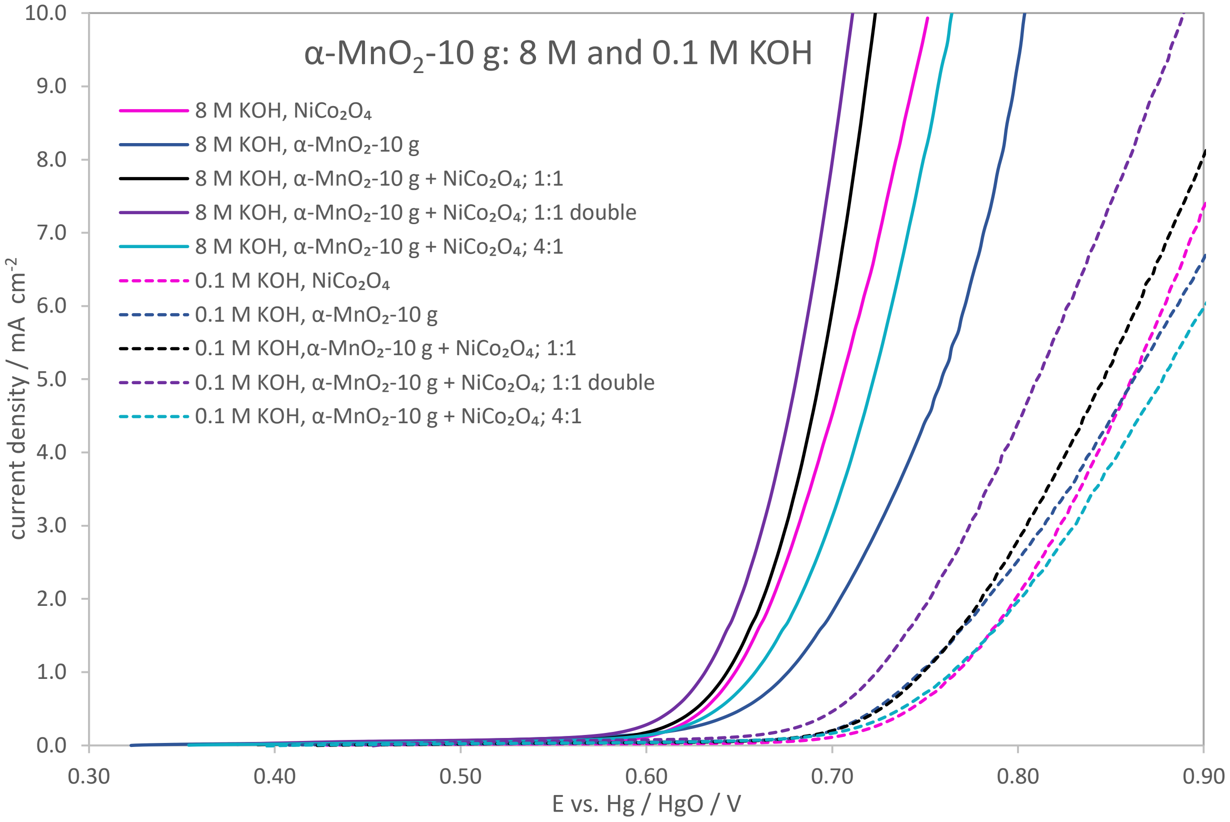

Figure 65: OER voltammograms of $NiCo_2O_4$, α-MnO_2-10 g and mixed catalysts in N_2 saturated 0.1 M and 8 M KOH at RT with a rotation rate ω of 1600 rpm (5th sweep) and a scan rate v of 5 mV s^{-1}.

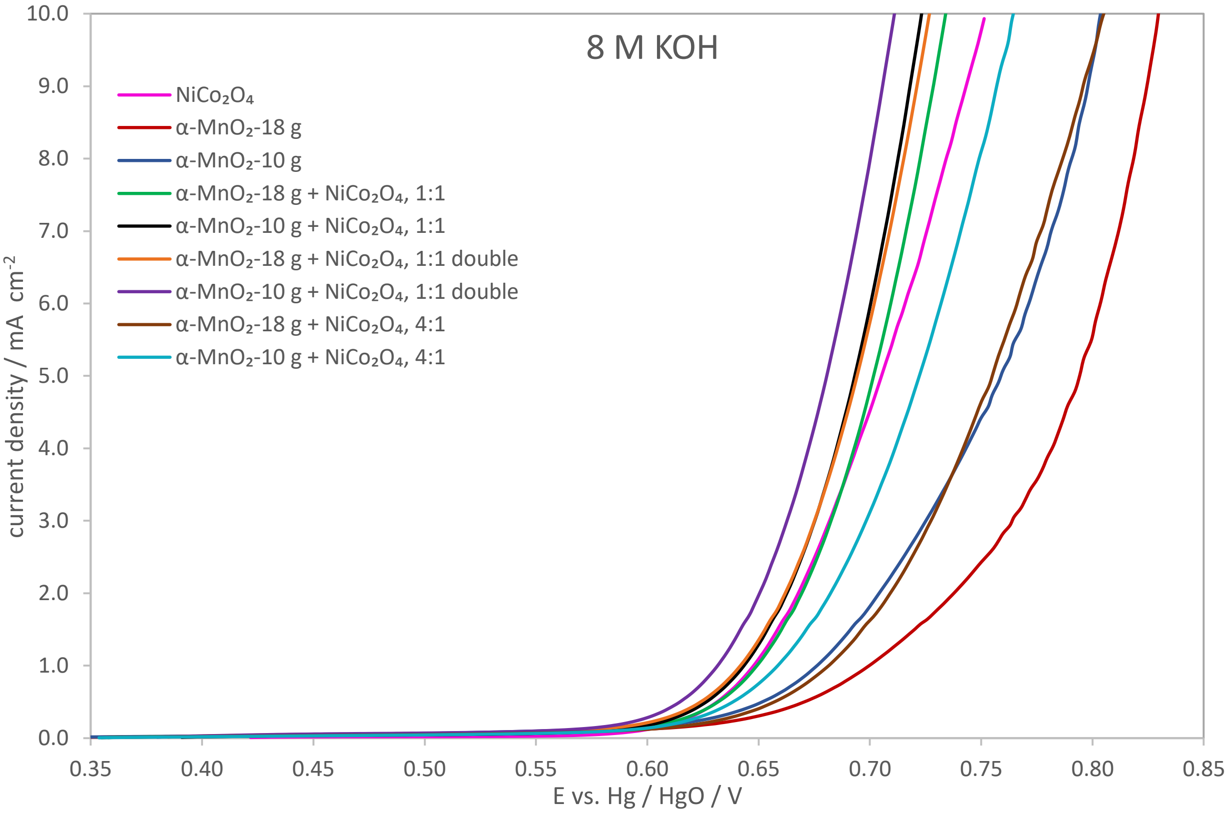

Figure 66: OER voltammograms of $NiCo_2O_4$, α-MnO_2 samples and mixed catalysts in N_2 saturated 8 M KOH at RT with a rotation rate ω of 1600 rpm (5th sweep) and a scan rate v of 5 mV s^{-1}.

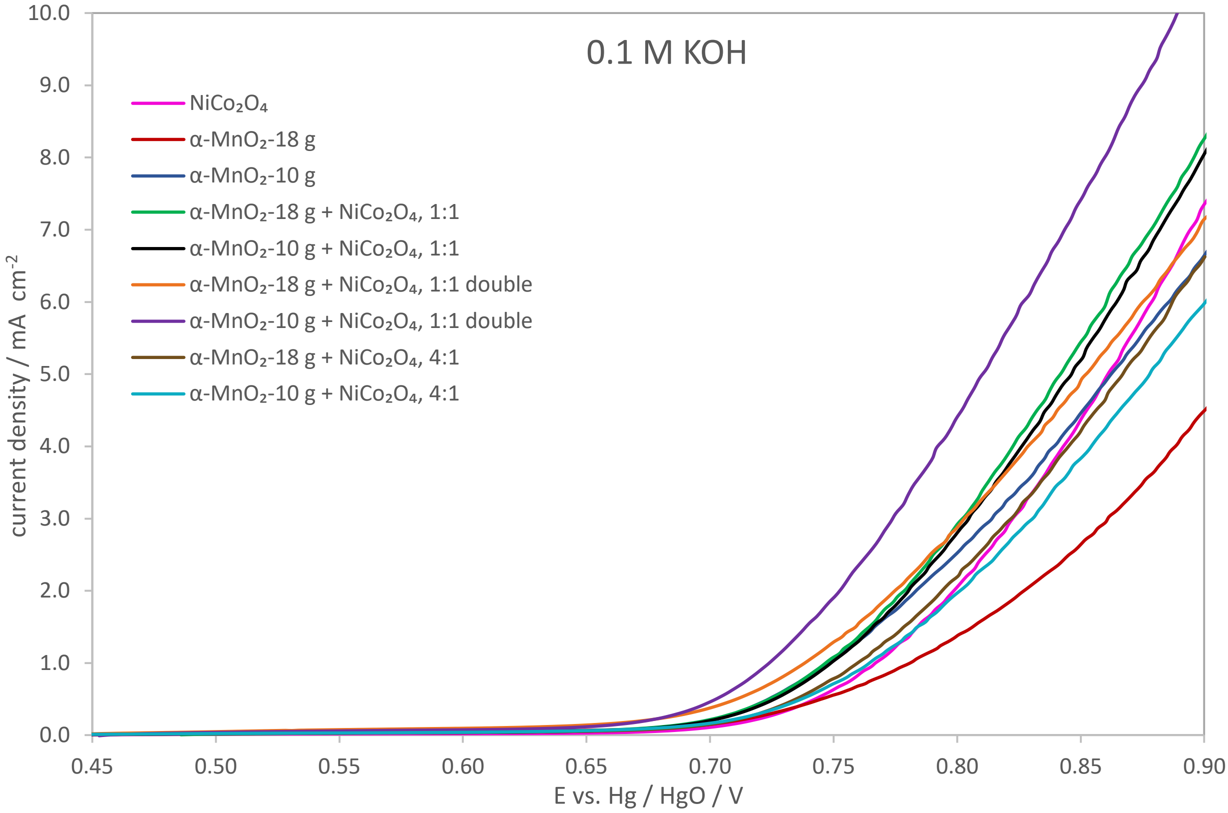

Figure 67: OER voltammograms of $NiCo_2O_4$, α-MnO_2 samples and mixed catalysts in N_2 saturated 0.1 M KOH at RT with a rotation rate ω of 1600 rpm (5th sweep) and a scan rate v of 5 mV s^{-1}.

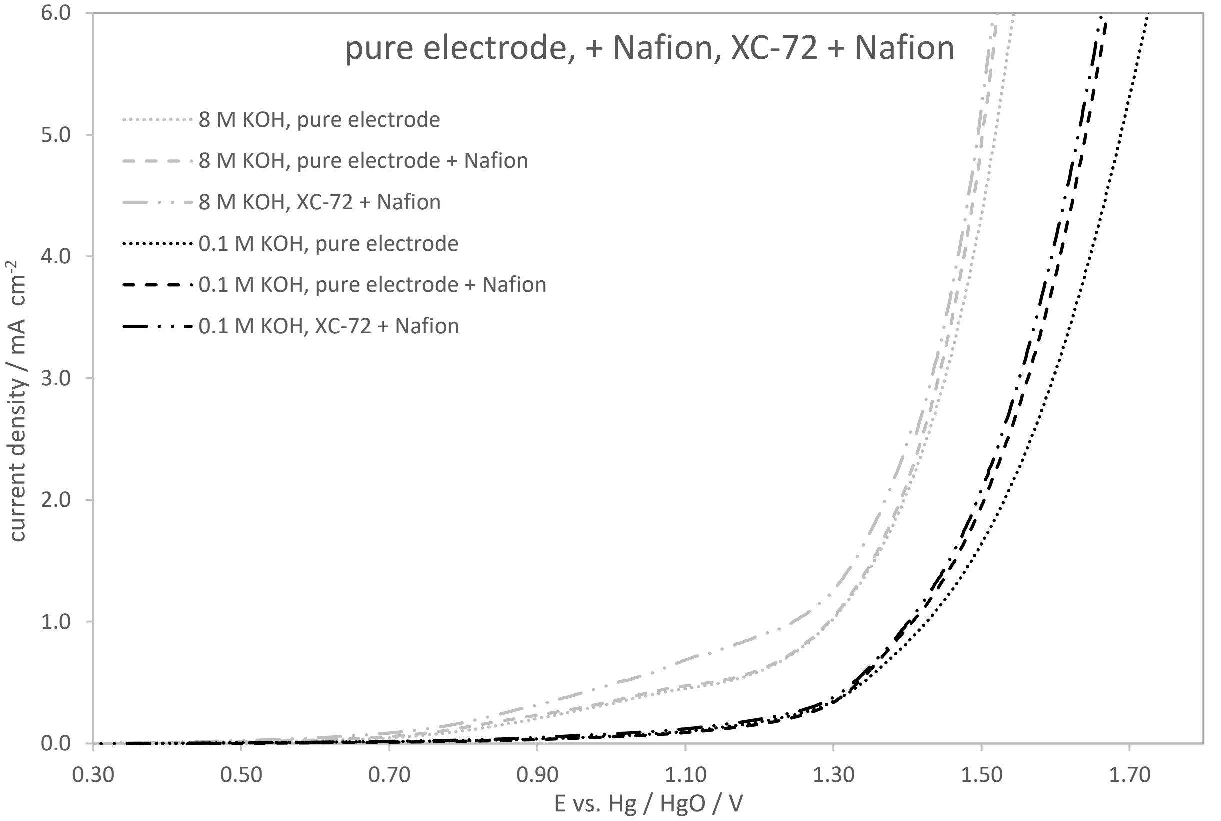

Figure 68: OER voltammograms of the pure electrode with/without Nafion layer and of carbon powder Vulcan XC-72 with Nafion layer in N_2 saturated 0.1 M and 8 M KOH at RT with a rotation rate ω of 1600 rpm (3rd sweep) and a scan rate v of 5 mV s^{-1}.

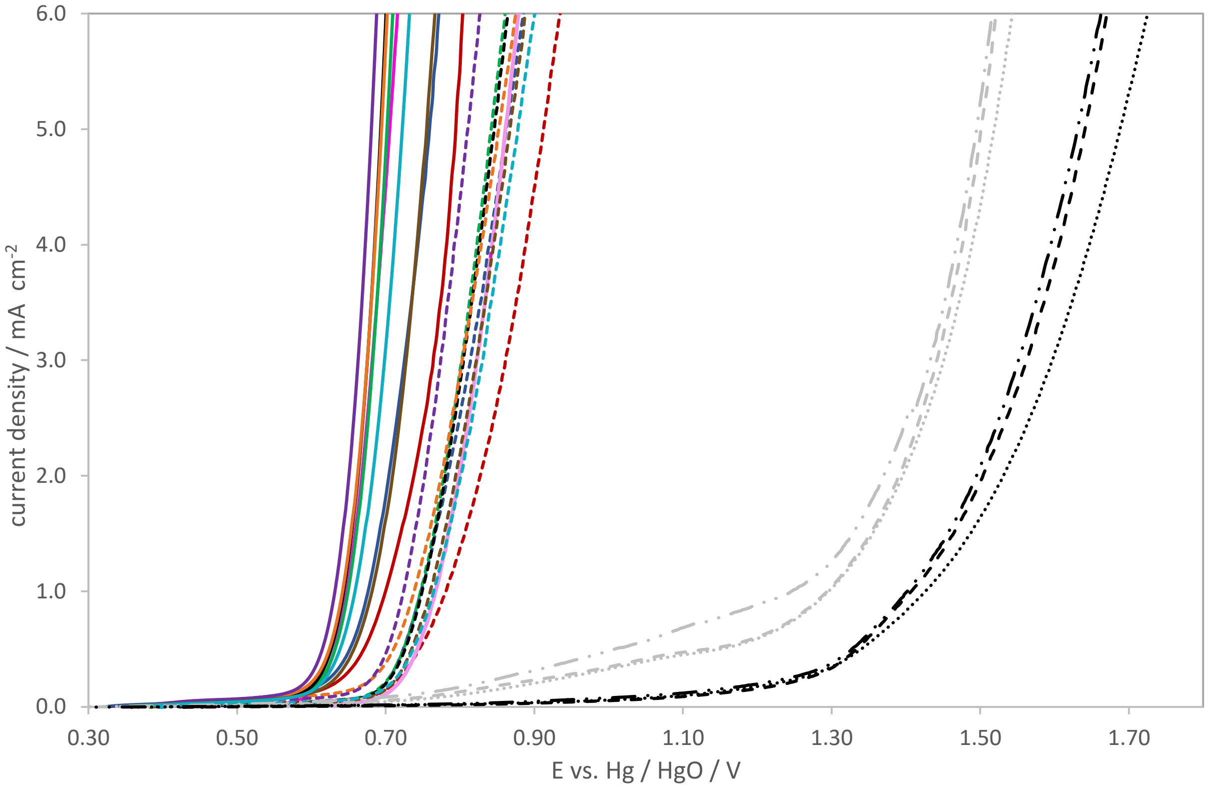

Figure 69: Comparison of the OER voltammograms of the pure electrode with/without Nafion layer and of carbon powder Vulcan XC-72 with Nafion layer and of all catalysts in N_2 saturated 0.1 M and 8 M KOH at RT with a rotation rate ω of 1600 rpm (5th and 3rd sweep) and a scan rate v of 5 mV s^{-1}.

4.2.3 Oxygen reduction reaction

4.2.3.1 ORR in 0.1 M KOH

For the investigation of the catalytic activity of the different catalyst samples concerning oxygen reduction reaction (ORR) in 0.1 M KOH, the associated voltammograms are illustrated in Figure 70 to Figure 83. The performance of the pure electrode with/without Nafion and the carbon powder XC-72 (also with Nafion) is examined for the comparison with the catalysts. As it can be seen in Figure 70, the pure glassy carbon electrode and the Nafion coated electrode exhibit almost equal current density of approx. -1.4 mA cm^{-2} and the addition of Nafion leads to a slightly decreased overpotential. The activity of the carbon powder is about 1 mA cm^{-2} higher compared to the pure electrode and an approx. 50 mV lower overpotential could be determined. Figure 71 shows the comparison of the catalysts with the pure electrode with/without Nafion and the carbon powder XC-72 with Nafion. It can be seen that the current density of the pure α-MnO_2 samples and of the mixed catalysts is more than twice as high and the overpotential is much lower (~200 mV) compared to the pure electrode with/without Nafion. In comparison with the carbon powder XC-72 with Nafion, the current density of the pure and mixed MnO_2 catalysts is about 0.5 – 1 mA cm^{-2} higher and the overpotential is ~150 mV lower. The performance of the pure $NiCo_2O_4$ spinel is not significantly enhanced compared to the pure electrode with/without Nafion and the current density is about 1 mA cm^{-2} lower than that of the carbon powder with Nafion. The catalysts containing α-MnO_2-18 g provide better performances than those using the α-MnO_2-10 g sample. This result correlates with the phenomena that higher specific surface area leads to higher catalytic activity for ORR due to the fact that more active sides for the oxygen adsorption are available [13]. It also has to be mentioned that the first sweep (1600 rpm_1) of the samples including α-MnO_2 always deviates from the following curves. A reduction peak at approx. -0.4 V is noticed (Figure 72) that can be attributed to the reduction of α-MnO_2 to MnOOH or Mn_2O_3 [12]. Furthermore, the current density decreases from the first to the fifth sweep, as described by Benhangi et al. [85]. This results from the conversion of the α-MnO_2 to less active species like MnOOH or Mn_3O_4 [13]. Mainar et al. [14] also mentioned a few other reasons for the current density shift like oxidation of the carbon added to the manganese dioxide catalysts to enhance conductivity. Figure 73 and Figure 74 show that even though the combination of α-MnO_2 with $NiCo_2O_4$ leads to slightly decreased current densities compared to the pure α-MnO_2, the mixed catalysts significantly increase the electrocatalytic activity in comparison to the pure $NiCo_2O_4$ spinel. The voltammograms of all catalysts at different rotation rates are illustrated in Figure 75 to Figure 83. All samples follow the trend of increasing current density with increasing rotation rate that can be explained by a faster oxygen transport to the electrode surface by applying higher rotation rates [31].

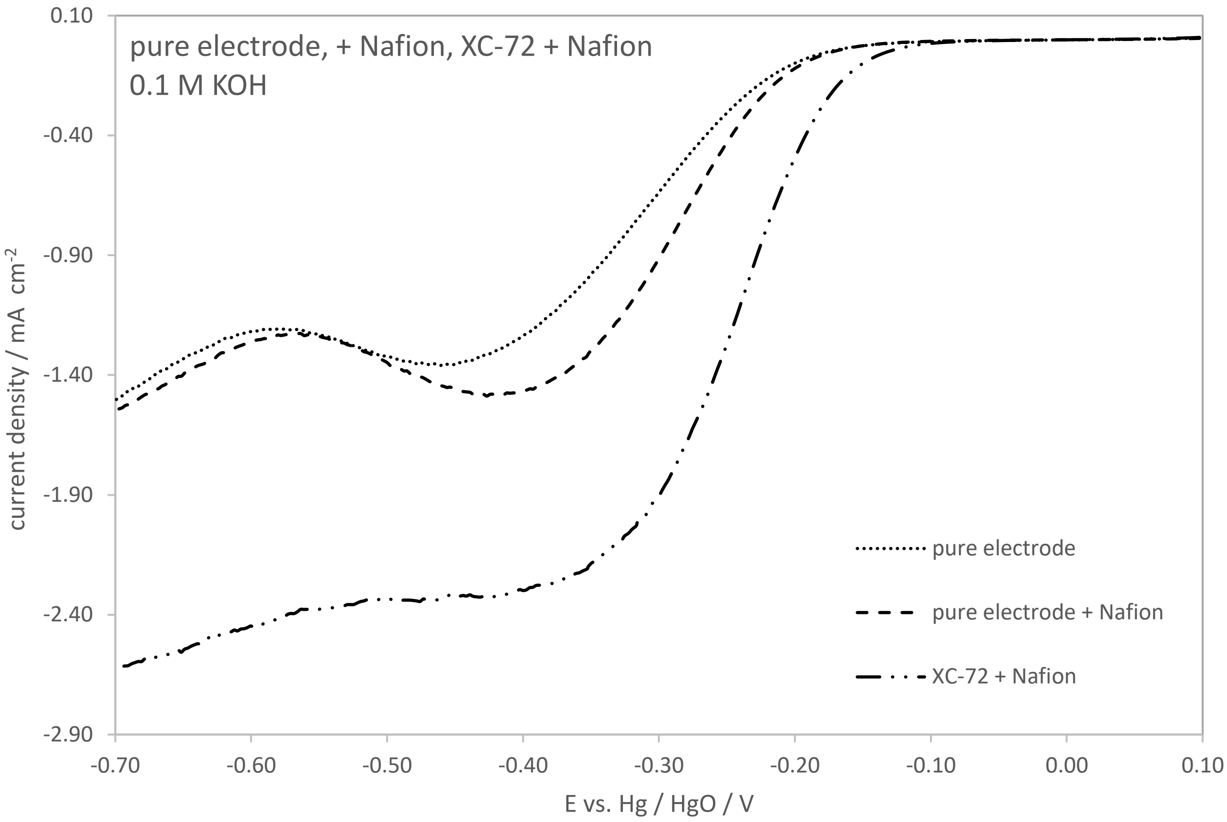

Figure 70: ORR voltammograms of the pure electrode with/without Nafion layer and of carbon powder Vulcan XC-72 with Nafion layer in O_2 saturated 0.1 M KOH at RT with a rotation rate ω of 1600 rpm (3rd sweep) and a scan rate v of 5 mV s^{-1}.

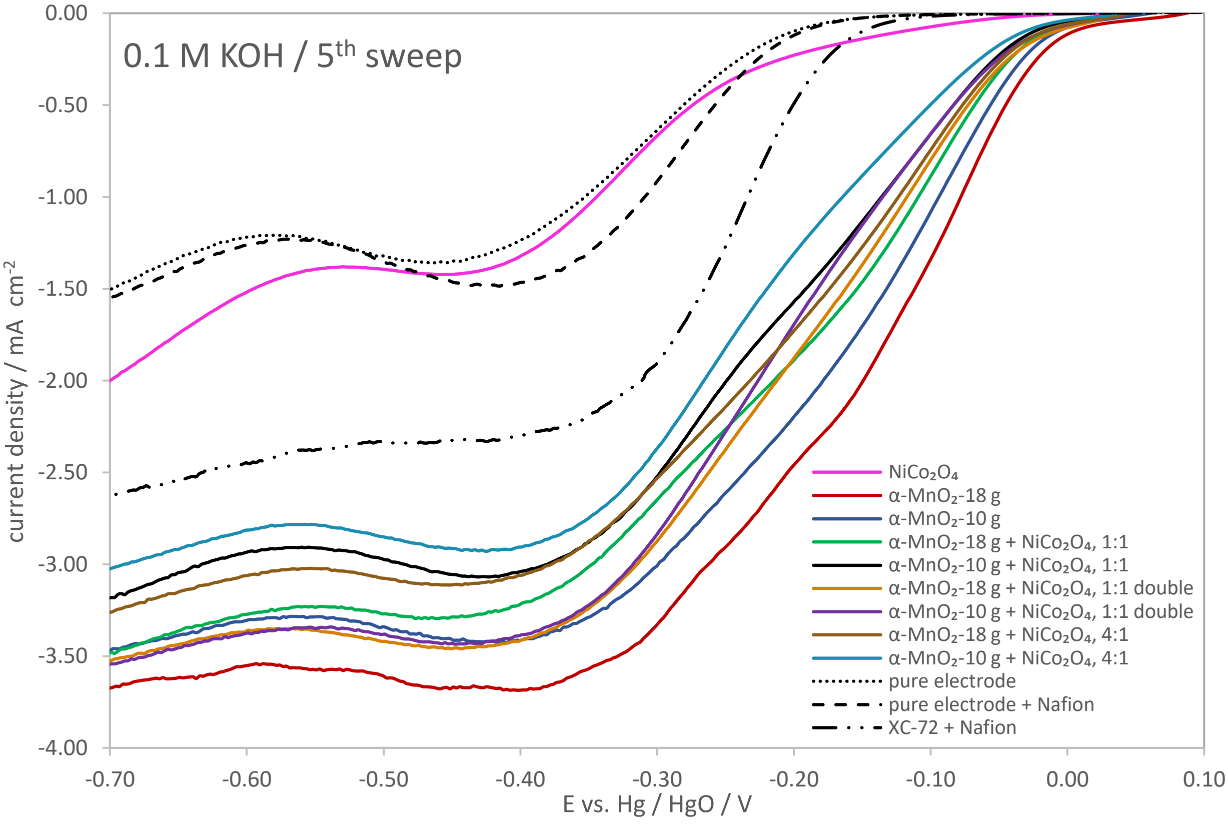

Figure 71: ORR voltammograms of $NiCo_2O_4$, α-MnO_2 samples and the mixed catalysts (5th sweep) compared to the pure electrode with/without Nafion layer and the carbon powder Vulcan XC-72 with Nafion (3rd sweep) in O_2 saturated 0.1 M KOH at RT with a rotation rate ω of 1600 rpm and a scan rate v of 5 mV s^{-1}.

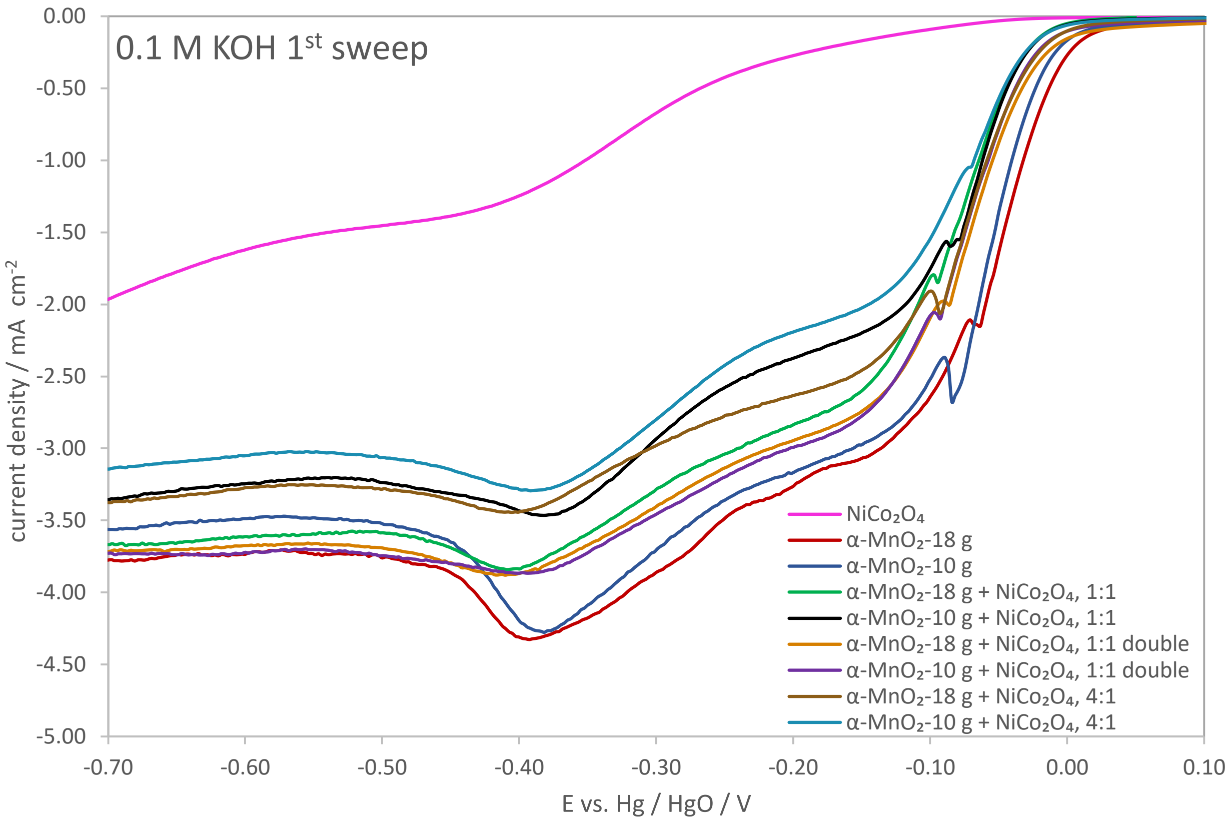

Figure 72: ORR voltammograms of $NiCo_2O_4$, α-MnO_2 samples and the mixed catalysts in O_2 saturated 0.1 M KOH at RT with a rotation rate ω of 1600 rpm (1st sweep) and a scan rate v of 5 mV s^{-1}.

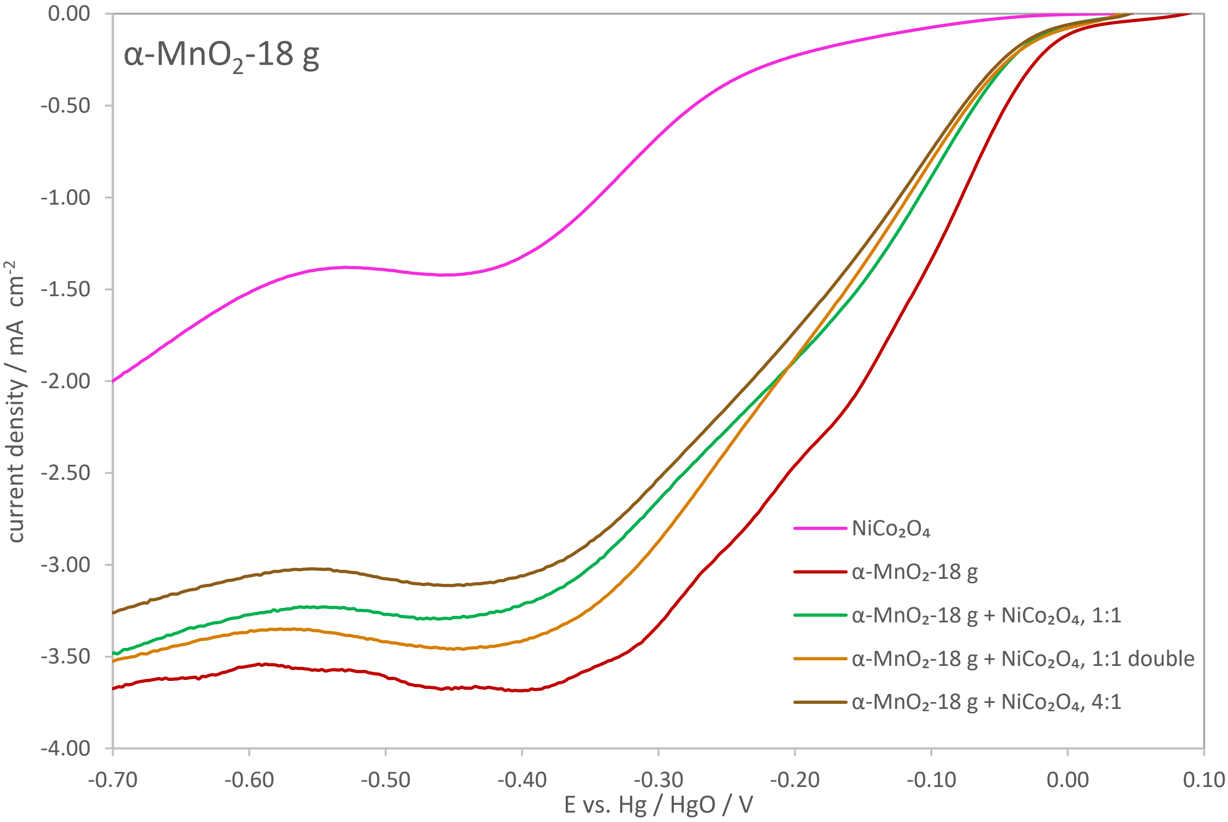

Figure 73: ORR voltammograms of $NiCo_2O_4$, α-MnO_2-18 g and the mixed catalysts in O_2 saturated 0.1 M KOH at RT with a rotation rate ω of 1600 rpm (5th sweep) and a scan rate v of 5 mV s^{-1}.

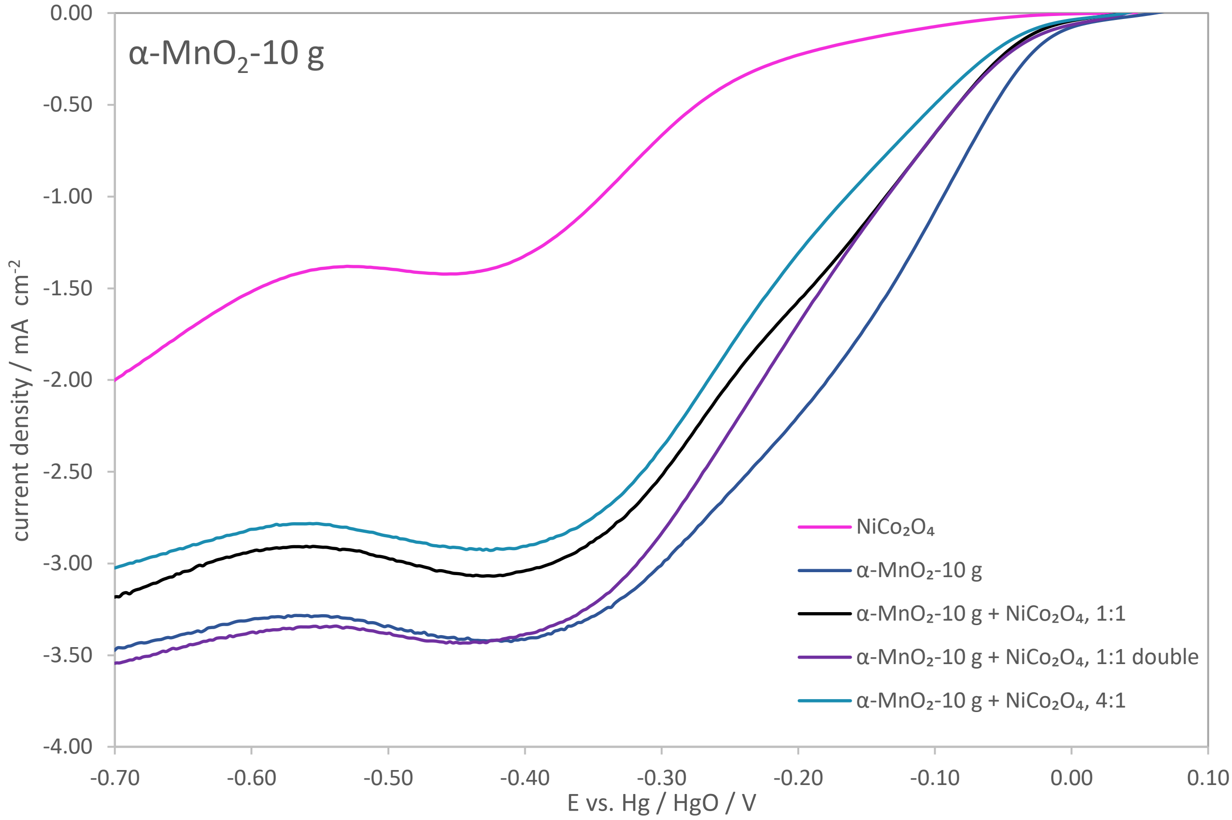

Figure 74: ORR voltammograms of $NiCo_2O_4$, α-MnO_2-10 g and the mixed catalysts in O_2 saturated 0.1 M KOH at RT with a rotation rate ω of 1600 rpm (5th sweep) and a scan rate v of 5 mV s^{-1}.

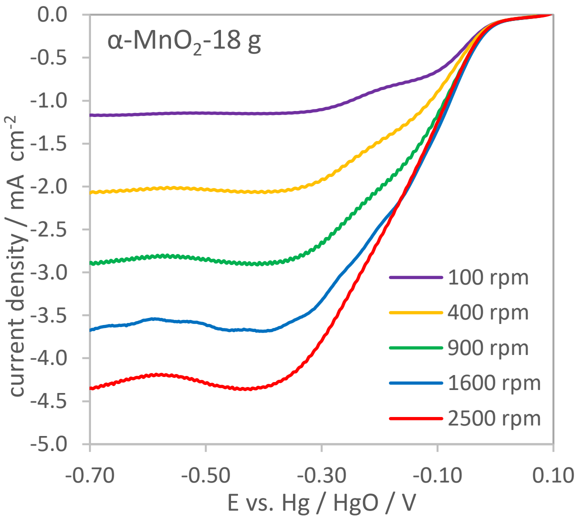

Figure 75: ORR voltammograms of α-MnO_2-18 g in O_2 saturated 0.1 M KOH at different rotation rates ω and a scan rate v of 5 mV s^{-1}.

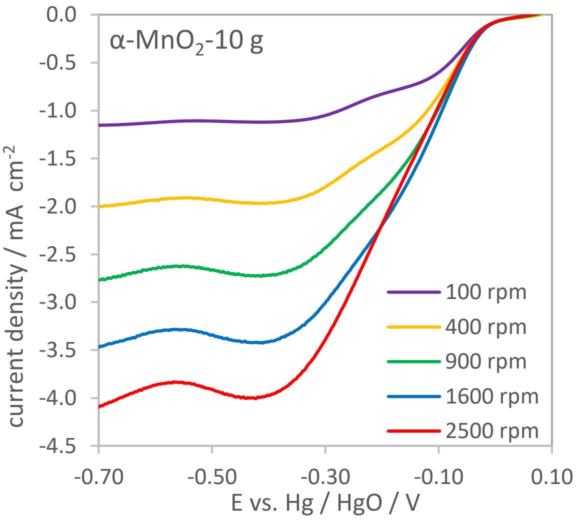

Figure 76: ORR voltammograms of α-MnO_2-10 g in O_2 saturated 0.1 M KOH at different rotation rates ω and a scan rate v of 5 mV s^{-1}.

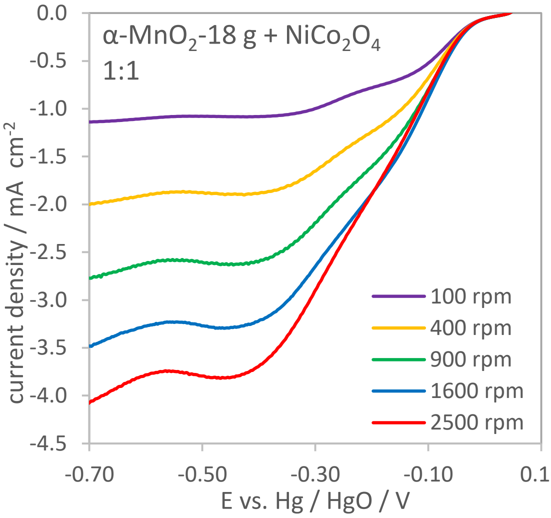

Figure 77: ORR voltammograms of α-MnO$_2$-18 g + NiCo$_2$O$_4$ (1:1) in O$_2$ saturated 0.1 M KOH at different rotation rates ω and a scan rate v of 5 mV s^{-1}.

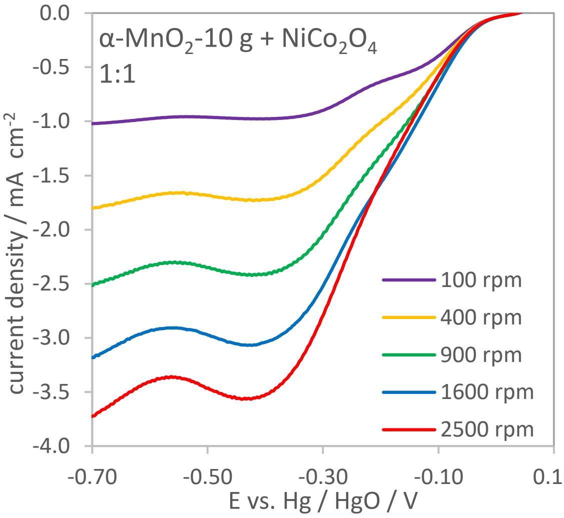

Figure 78: ORR voltammograms of α-MnO$_2$-10 g + NiCo$_2$O$_4$ (1:1) in O$_2$ saturated 0.1 M KOH at different rotation rates ω and a scan rate v of 5 mV s^{-1}.

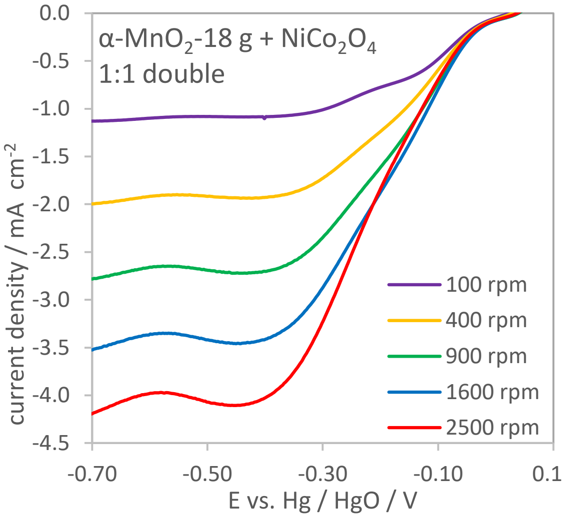

Figure 79: ORR voltammograms of α-MnO$_2$-18 g + NiCo$_2$O$_4$ (1:1 double) in O$_2$ saturated 0.1 M KOH at different rotation rates ω and a scan rate v of 5 mV s^{-1}.

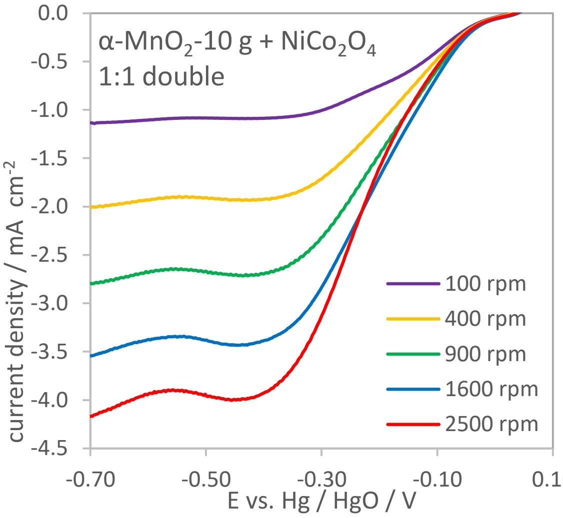

Figure 80: ORR voltammograms of α-MnO$_2$-10 g + NiCo$_2$O$_4$ (1:1 double) in O$_2$ saturated 0.1 M KOH at different rotation rates ω and a scan rate v of 5 mV s^{-1}.

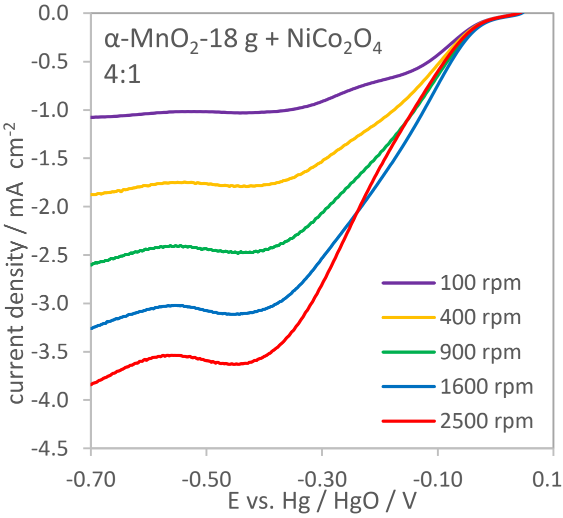

Figure 81: ORR voltammograms of α-MnO$_2$-18 g + NiCo$_2$O$_4$ (4:1) in O$_2$ saturated 0.1 M KOH at different rotation rates ω and a scan rate v of 5 mV s^{-1}.

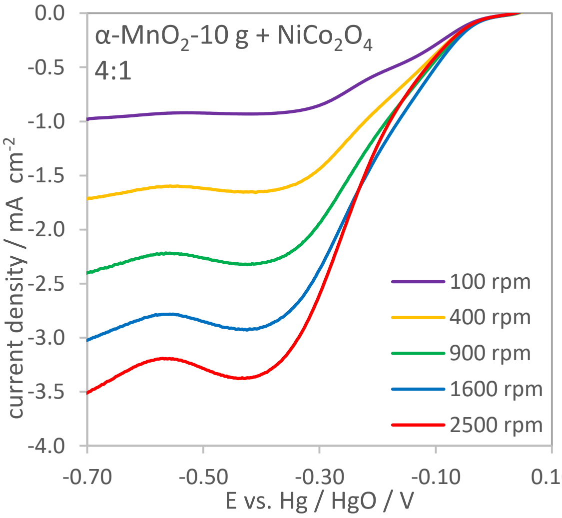

Figure 82: ORR voltammograms of α-MnO$_2$-10 g + NiCo$_2$O$_4$ (4:1) in O$_2$ saturated 0.1 M KOH at different rotation rates ω and a scan rate v of 5 mV s^{-1}.

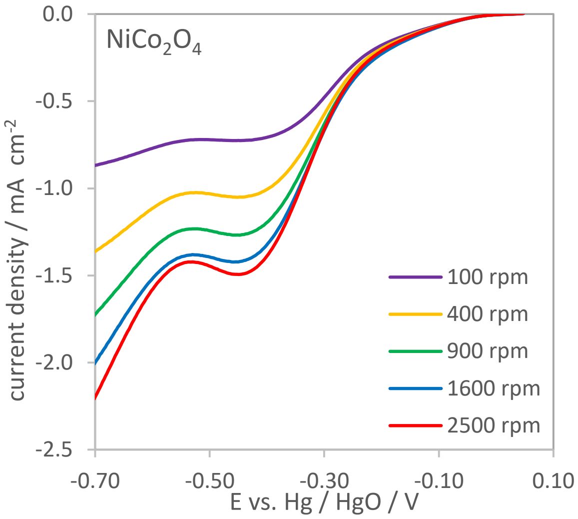

Figure 83: ORR voltammograms of $NiCo_2O_4$ in O_2 saturated 0.1 M KOH at different rotation rates ω and a scan rate v of 5 mV s^{-1}.

4.2.3.2 ORR in 8 M KOH

Zinc-air battery systems are generally operated in a highly concentrated potassium hydroxide solution and therefore, the oxygen reduction reaction (ORR) is also carried out in 8 M KOH (Figure 84 to Figure 94). In Figure 84, the ORR voltammograms of the pure electrode with/without Nafion and of XC-72 with Nafion can be seen. Almost equal current density and overpotential is observed for the pure electrode with and without Nafion. The XC-72 sample results a slightly higher current density and a slightly reduced overpotential, as already observed for the 0.1 M KOH solution. All curves show a reduction peak at approx. -0.4 V that is attributed to reactions of the glassy carbon electrode [84]. The voltammogram of XC-72 illustrates an additional peak at around -0.1 V indicating some kind of carbon reduction. Figure 85 to Figure 87 show the voltammograms (five sweeps) of the pure α-MnO_2-18 g, the pure $NiCo_2O_4$ and the mixed α-MnO_2-18 g/$NiCo_2O_4$ (4:1) catalyst. The first sweep of the voltammograms of the α-MnO_2 catalysts deviates from the following ones, as already described for the 0.1 M KOH electrolyte solution. Additionally, the current density drastically decreases from the first to the second sweep. The current density of the pure $NiCo_2O_4$ spinel is quite constant after the 2nd sweep whereas in the case of the pure MnO_2 and mixed catalysts it is slightly reduced with each sweep. As seen in Figure 88, the current density of the mixed catalyst between cycles five and ten still decreases with increasing cycle number, what is also observed for the pure α-MnO_2 (not shown here). This can also be explained by the fact that the pronounced reduction peaks in the first sweep indicate the formation of manganese oxide species like Mn_3O_4 presenting a much lower catalytic activity and inactivating the material. Another reason could be that in high concentrated KOH solutions, soluble Mn^{3+} form complexes like $[Mn(OH)_4]^-$. Gyenge and Drillet [69] described that these complexes can influence the hydroxide peroxide decomposition taking place during the ORR [12][85][86]. The comparison of the pure and mixed catalysts with the pure electrode with/without Nafion and with XC-72 with Nafion is shown in Figure 89 and Figure 90. In the first sweep (Figure 89), the pure α-MnO_2 and mixed catalysts exhibit a much higher current density compared to the pure $NiCo_2O_4$, the pure electrode with/without Nafion and XC-72 with Nafion. The current density of the mixed catalysts increases in the following order: 4:1 < 1:1 < 1:1 double, as already observed in 0.1 M KOH. A comparison of the mixed catalysts with the pure α-MnO_2 is difficult because of various reduction peaks. In the fifth sweep (Figure 90), the pure catalysts exhibit slightly higher current densities compared to the pure electrode and the carbon powder. The current density of $NiCo_2O_4$ is slightly higher compared to the α-MnO_2 samples. Additionally, the overpotential of α-MnO_2 is much higher (~250 mV) compared to the pure electrode and to the spinel. Mixing α-MnO_2 and $NiCo_2O_4$ leads to more stable catalysts. The overpotential of the mixed catalysts is nearly as high as that of the pure α-MnO_2, but the current density is significantly enhanced compared to both individual catalysts. The current density of the pure α-MnO_2-18 g and the mixed α-MnO_2-18 g/$NiCo_2O_4$ 1:1 double sample is higher compared to that of the corresponding pure and mixed α-MnO_2-10 g sample and vice versa for the 1:1 and 4:1 samples. The current density of the mixed catalysts increases with the total α-MnO_2 amount: 1:1 < 4:1 < 1:1 double (Figure 91 and Figure 92). Additionally, voltammograms of the mixed catalysts are recorded at different rotation rates in the following order: 1600, 900, 400 and 2500 rpm. As can be seen in Figure 93, the 2500 rpm curve shows the same current density as the 1600 rpm curve that may be attributed to the low stability of the α-MnO_2 catalyst. Therefore, no further investigations are performed at different rotation rates in 8 M KOH. In contrast to this, the current density of the pure $NiCo_2O_4$ spinel increases with increasing rotation rate (Figure 94).

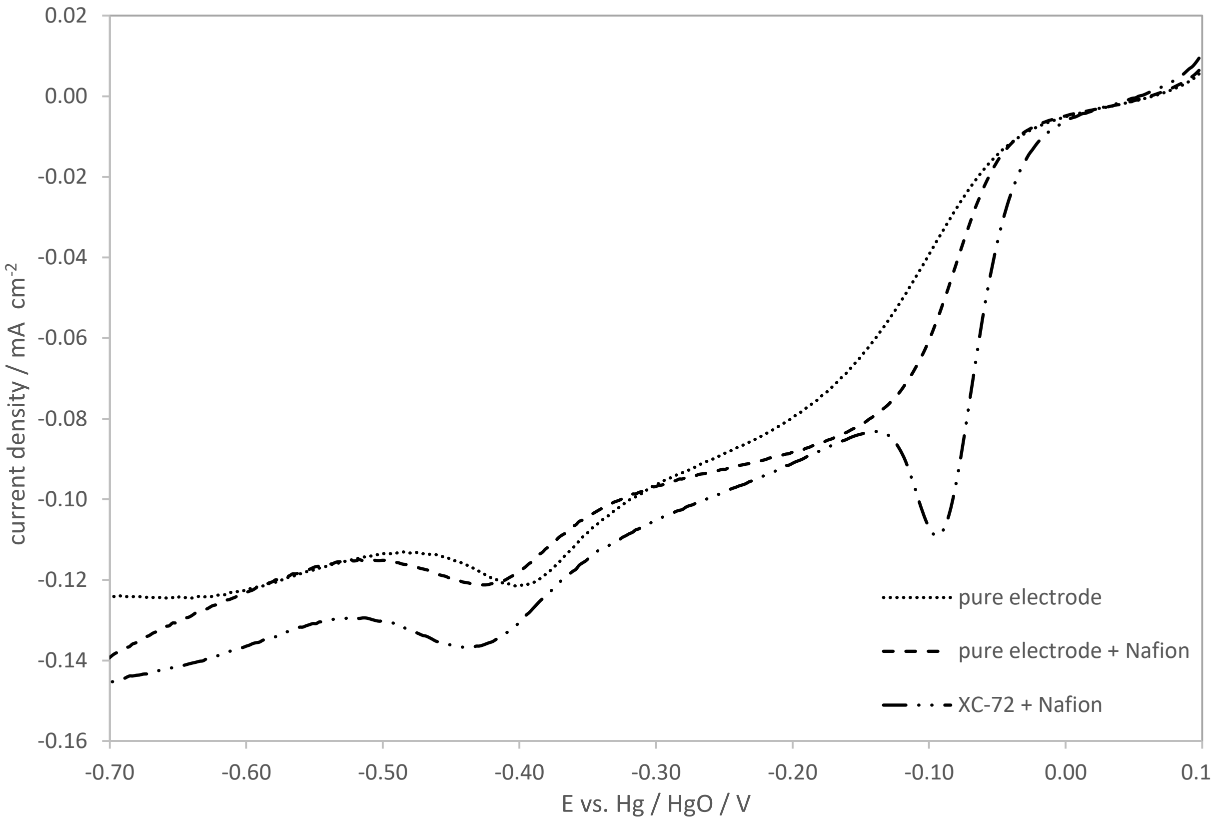

Figure 84: ORR voltammograms of the pure electrode with/without Nafion and of Vulcan XC-72 with Nafion layer in O_2 saturated 8 M KOH at RT with a rotation rate ω of 1600 rpm (3^{rd} sweep) and a scan rate v of 5 mV s^{-1}.

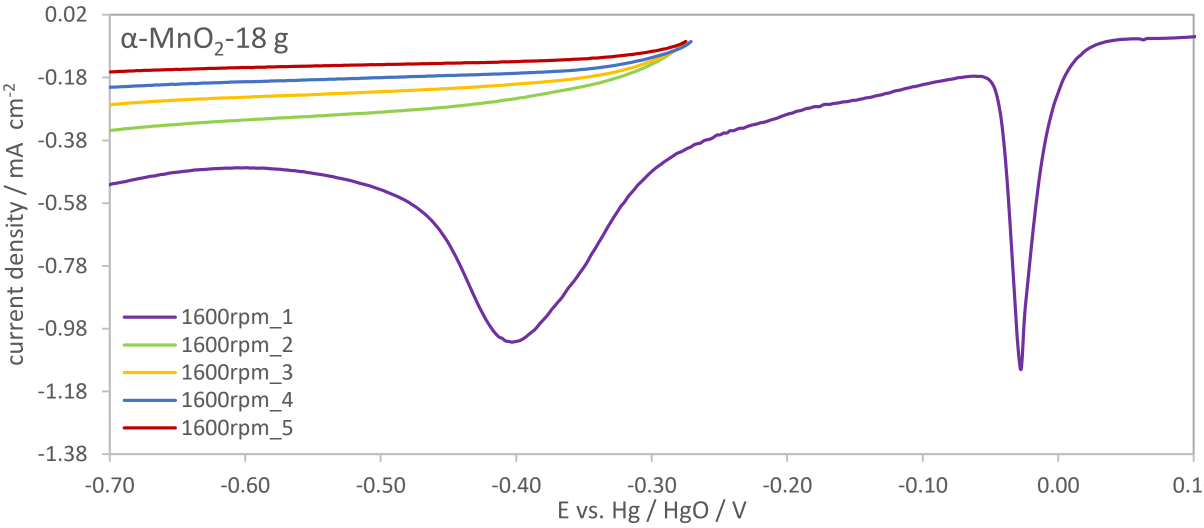

Figure 85: ORR voltammograms of α-MnO_2 in O_2 saturated 8 M KOH at RT with a rotation rate ω of 1600 rpm (5 sweeps) and a scan rate v of 5 mV s^{-1}.

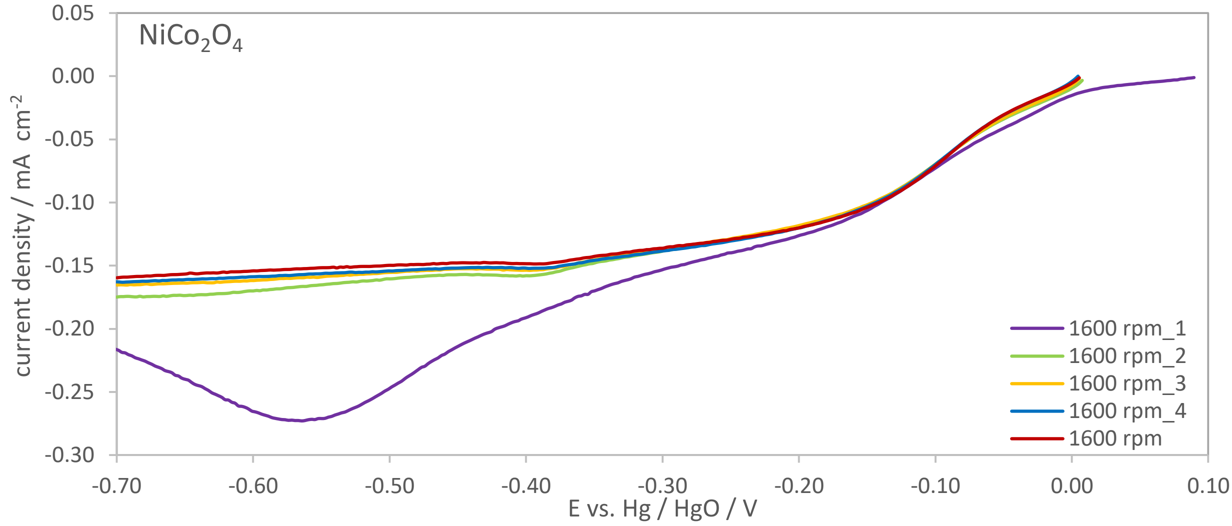

Figure 86: ORR voltammograms of $NiCo_2O_4$ in O_2 saturated 8 M KOH at RT with a rotation rate ω of 1600 rpm (5 sweeps) and a scan rate v of 5 mV s^{-1}.

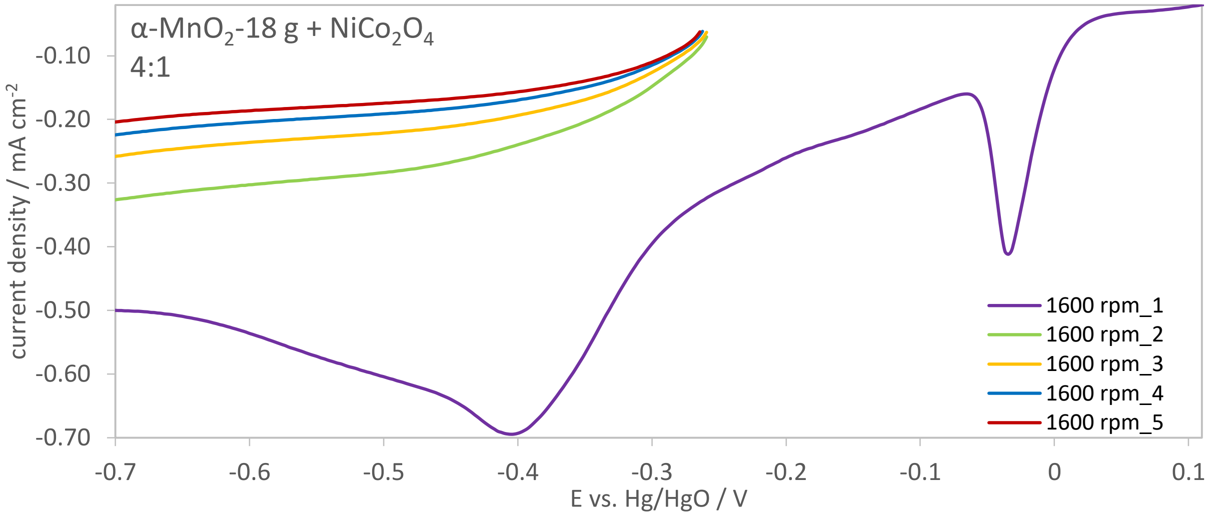

Figure 87: ORR voltammograms of the mixed catalyst in O_2 saturated 8 M KOH at RT with a rotation rate ω of 1600 rpm (5 sweep) and a scan rate v of 5 mV s^{-1}.

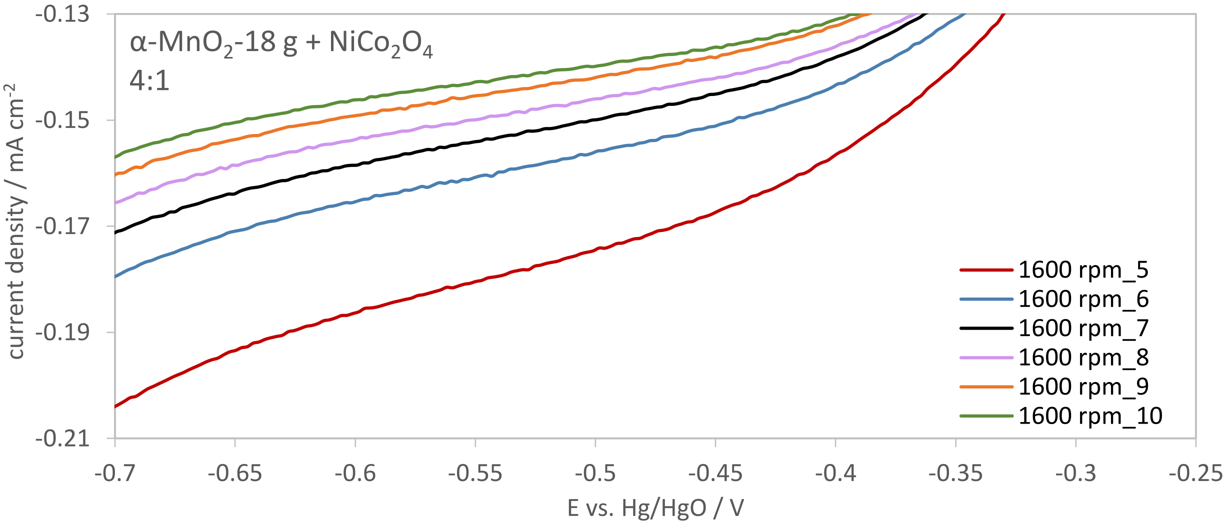

Figure 88: ORR voltammograms of the mixed catalyst in O_2 saturated 8 M KOH at RT with a rotation rate ω of 1600 rpm (5th – 10th sweep) and a scan rate v of 5 mV s^{-1}.

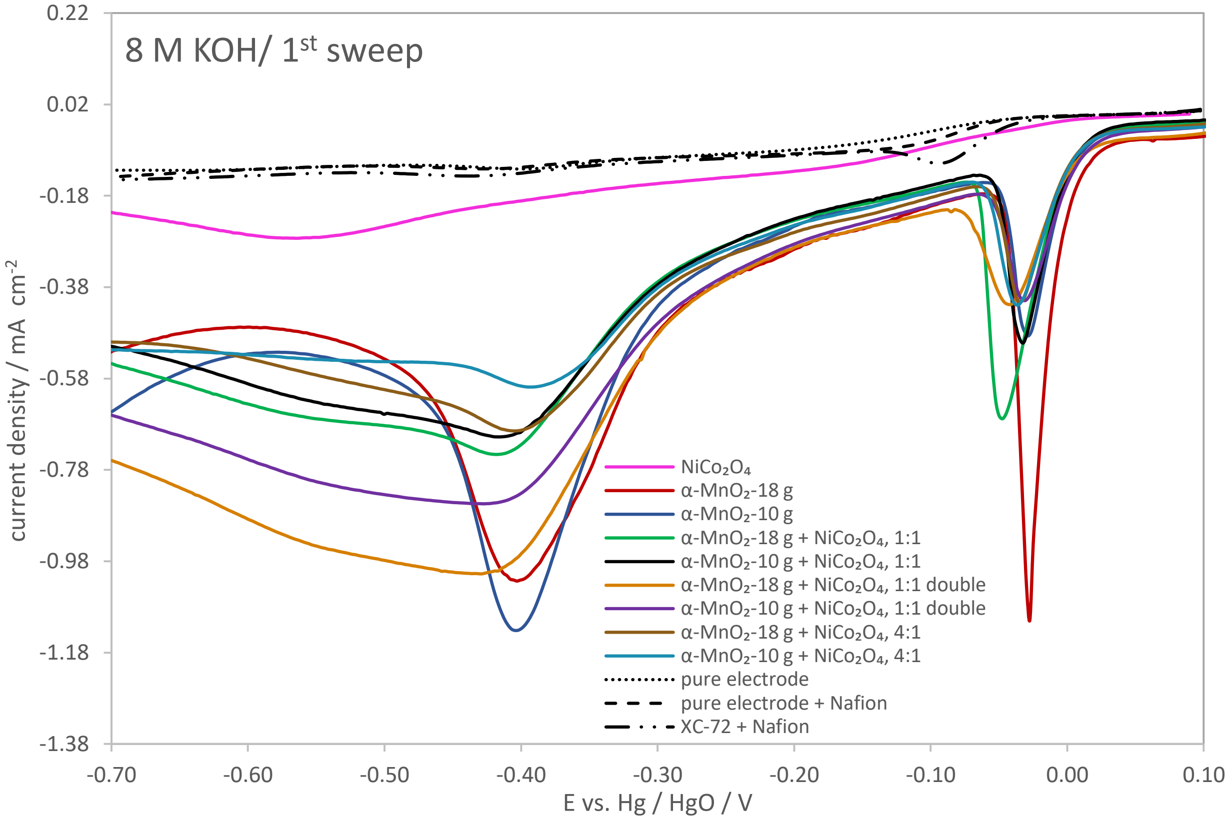

Figure 89: ORR voltammograms of $NiCo_2O_4$, α-MnO_2 samples and the mixed catalysts (1st sweep) compared to the pure electrode with/without Nafion layer and the carbon powder Vulcan XC-72 with Nafion (3rd sweep) in O_2 saturated 8 M KOH at RT with a rotation rate ω of 1600 rpm and a scan rate v of 5 mV s^{-1}.

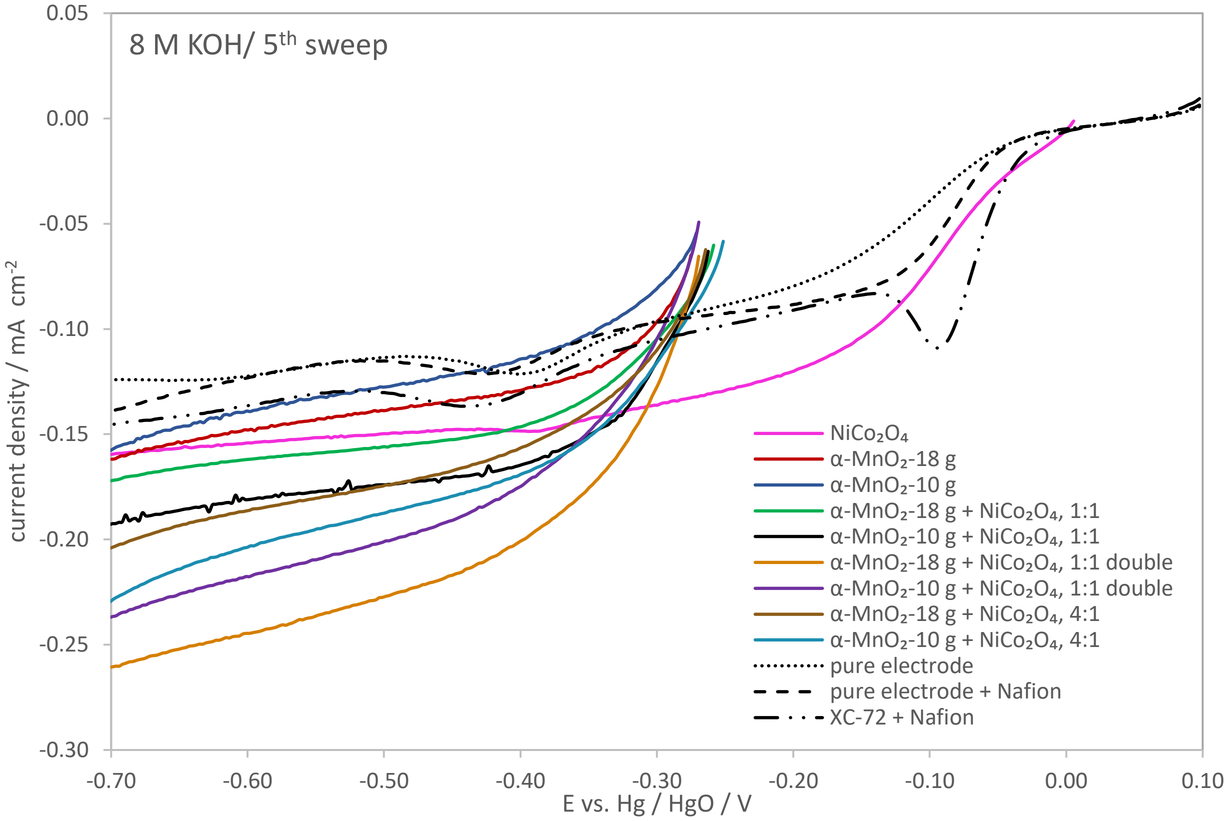

Figure 90: ORR voltammograms of $NiCo_2O_4$, α-MnO_2 samples and the mixed catalysts (5th sweep) compared to the pure electrode with/without Nafion layer and the carbon powder Vulcan XC-72 with Nafion (3rd sweep) in O_2 saturated 8 M KOH at RT with a rotation rate ω of 1600 rpm and a scan rate v of 5 mV s^{-1}.

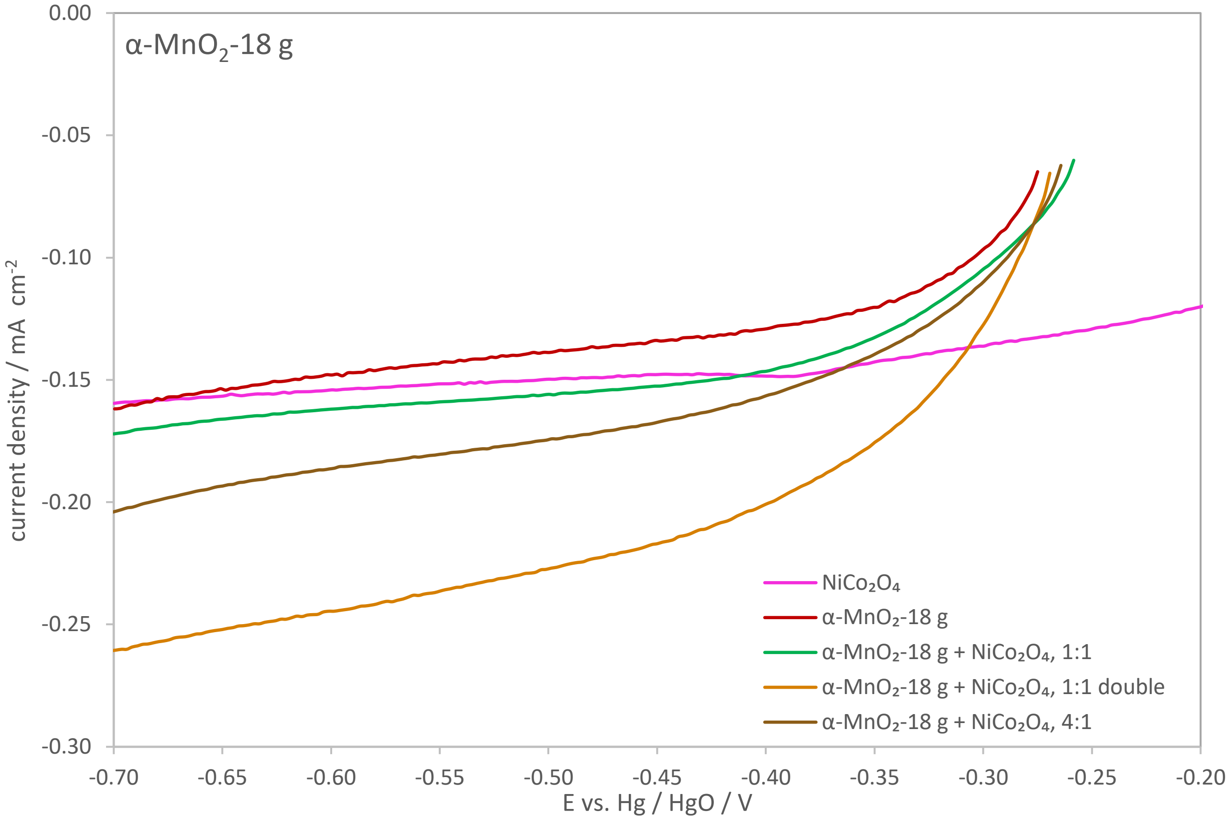

Figure 91: ORR voltammograms of $NiCo_2O_4$, α-MnO_2-18 g and the mixed catalysts in O_2 saturated 8 M KOH at RT with a rotation rate ω of 1600 rpm (5th sweep) and a scan rate v of 5 mV s^{-1}.

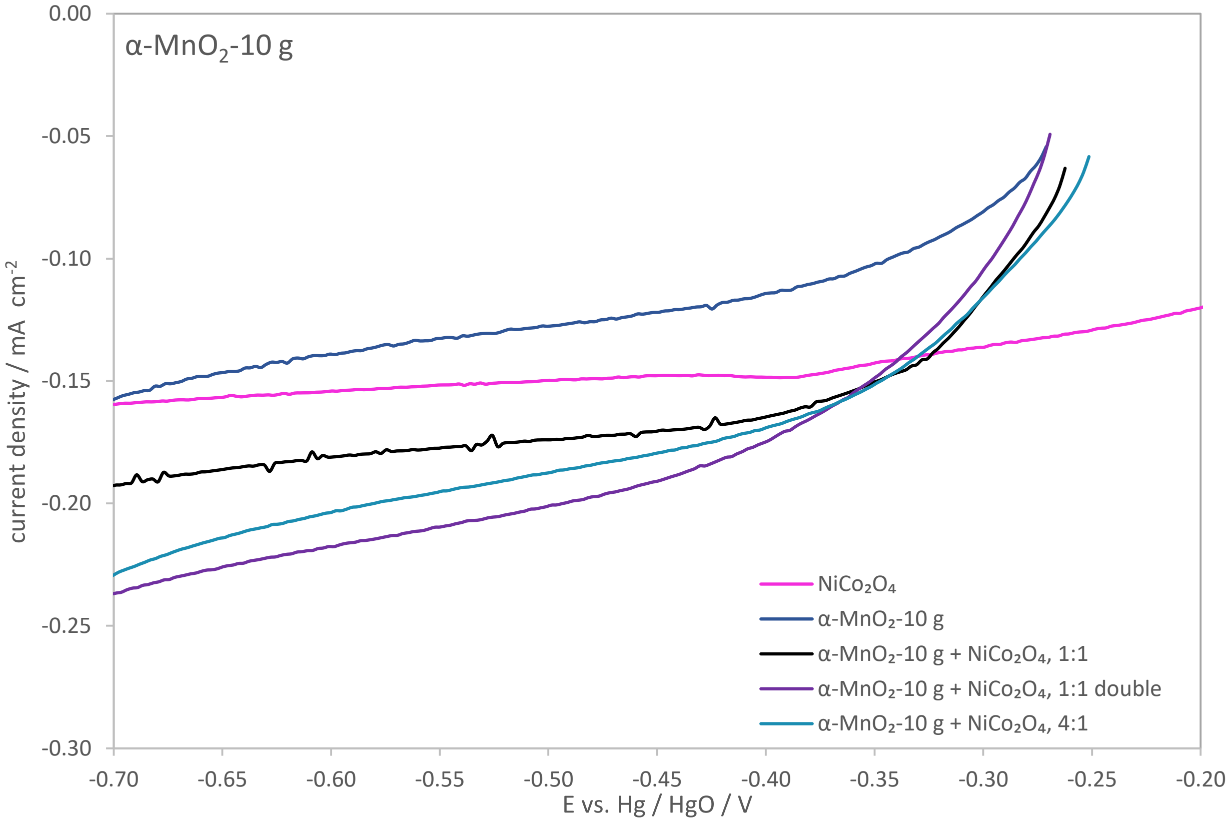

Figure 92: ORR voltammograms of $NiCo_2O_4$, α-MnO_2-10 g and the mixed catalysts in O_2 saturated 8 M KOH at RT with a rotation rate ω of 1600 rpm (5th sweep) and a scan rate v of 5 mV s^{-1}.

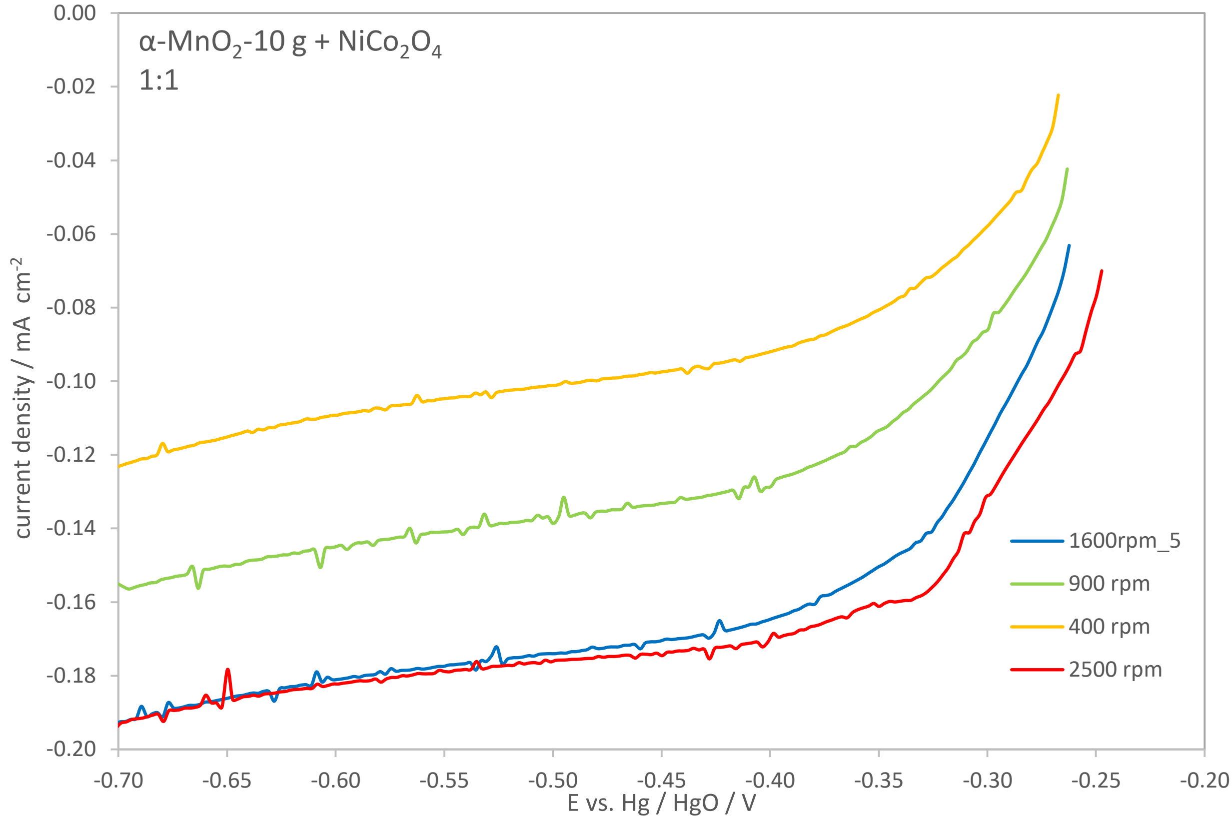

Figure 93: ORR voltammograms of mixed catalyst in O_2 saturated 8 M KOH at different rotation rates ω and a scan rate v of 5 mV s^{-1}.

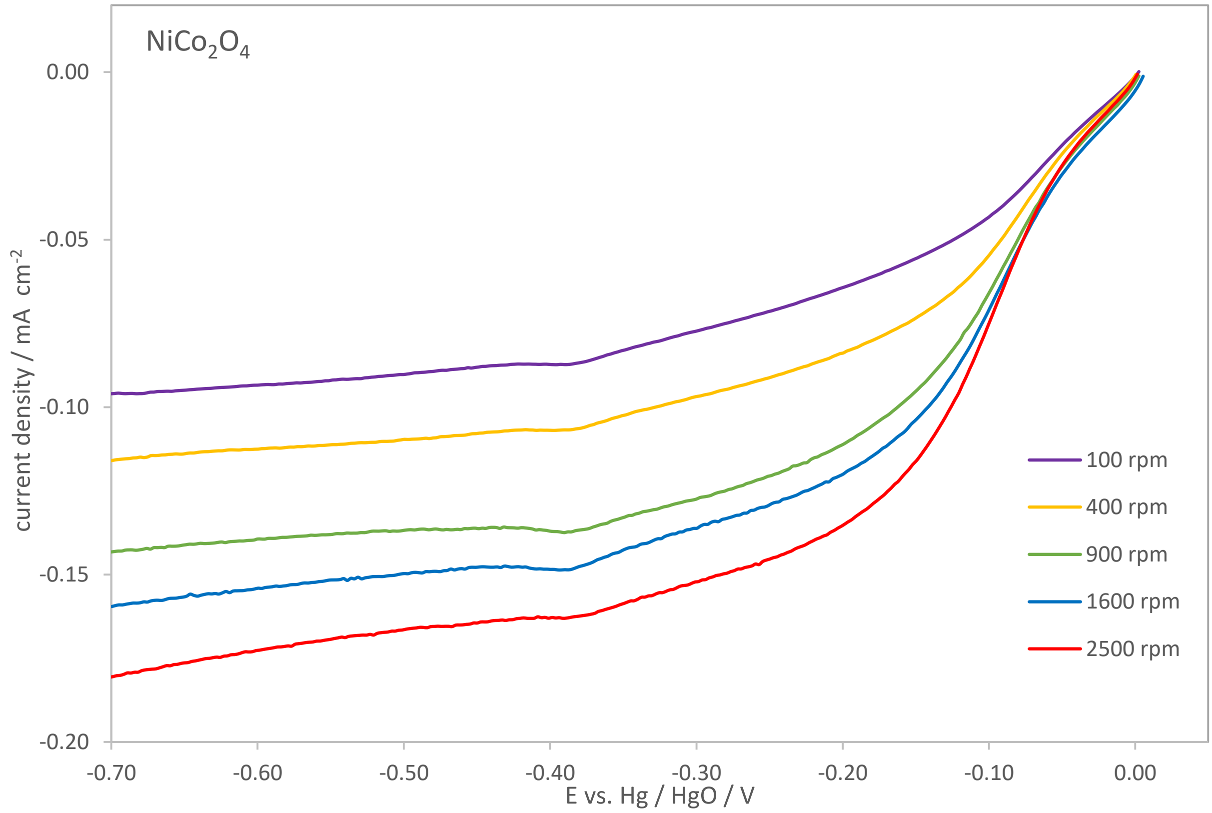

Figure 94: ORR voltammograms of $NiCo_2O_4$ in O_2 saturated 8 M KOH at different rotation rates ω and a scan rate v of 5 mV s^{-1}.

4.2.3.3 Comparison of ORR in 0.1 M and 8 M KOH

Figure 95 illustrates the comparison of the pure electrode with/without Nafion and XC-72 coated with Nafion in 8 M and 0.1 M KOH. In Figure 96, the pure and mixed catalysts are compared in both electrolyte solutions. As can be seen, all materials indicate a higher current density in 0.1 M KOH than in 8 M KOH due to higher solubility of oxygen (0.1 M KOH: ~1.1 x 10^{-6} mol/L; 8 M KOH: ~1.0 x 10^{-7} mol/L) in diluted electrolyte [87–89].

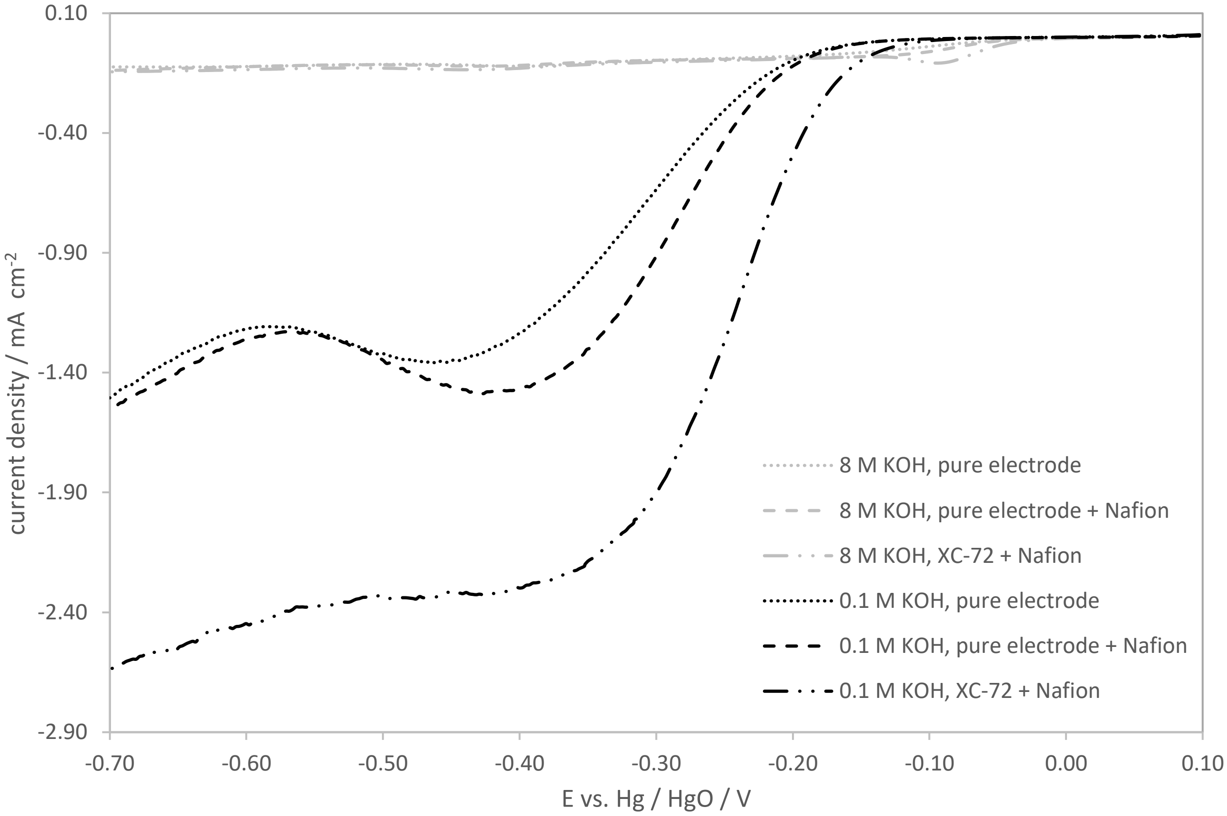

Figure 95: ORR voltammograms of the pure electrode with/without Nafion and of Vulcan XC-72 + Nafion in O_2 saturated 0.1 M and 8 M KOH at RT with a rotation rate ω of 1600 rpm (3^{rd} sweep) and a scan rate v of 5 mV s^{-1}.

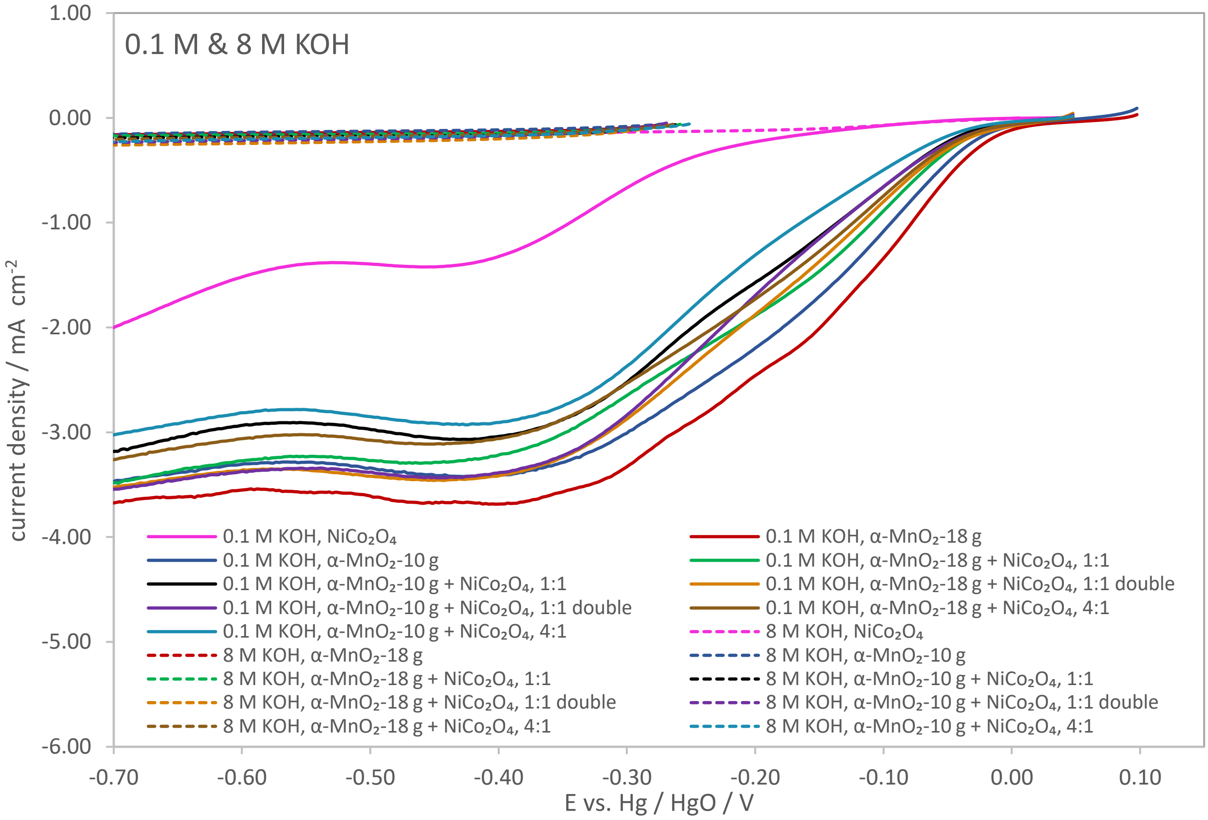

Figure 96: ORR voltammograms of $NiCo_2O_4$, α-MnO_2 samples and the mixed catalysts in O_2 saturated 0.1 M and 8 M KOH at RT with a rotation rate ω of 1600 rpm (5th sweep) and a scan rate v of 5 mV s^{-1}.

4.2.4 Levich analysis

The Levich plots of α-MnO_2-18 g, α-MnO_2-10 g, the mixed α-MnO_2/$NiCo_2O_4$ catalysts and $NiCo_2O_4$ are shown in Figure 97 to Figure 105. The limiting current density of the ORR voltammograms at -0.45 V is plotted against the square root of the rotation speed. Straight lines with an intercept not equal to zero (diffusion and kinetic controlled process) are obtained and linearity is proofed by means of R^2. The Levich equation (chapter 2.6.3) can be utilized for all samples to calculate the number of electrons n transferred during the oxygen reduction reaction using the parameters given in chapter 3.3.3. Theoretically, a number of 4 electrons should be exchanged during the reduction of oxygen as described in chapter 2.2.4. As it can be seen in Table 8, the number of electrons in this work is getting smaller with higher rotating speed. This is because of the intermediate H_2O_2 produced during the $2e^-$ pathway, which does not always react completely to the end product and therefore, electron numbers below 4 are obtained. With higher rotation speed more and more H_2O_2 is torn off the electrode and the numbers of final n are getting smaller and smaller [12]. The $NiCo_2O_4$ spinel shows in general a lower value of exchanged electrons in comparison to α-MnO_2, whereas the results for the mixed catalysts lie in between these two. The pure and mixed α-MnO_2-10 g samples display lower n values than the 18 g samples. In general, a higher number of transferred electrons indicates a better catalytic activity towards ORR (α-MnO_2 > α-MnO_2/$NiCo_2O_4$ 1:1 double > α-MnO_2/$NiCo_2O_4$ 1:1 > α-MnO_2/$NiCo_2O_4$ 4:1 > $NiCo_2O_4$) [31]. The comparison of the Levich plots of all samples can be seen in Figure 106 and Figure 107. The pure and mixed α-MnO_2 samples exhibit a slightly different slope and a nearly equal intercept value with the y-axis. In contrast, the $NiCo_2O_4$ line is much more flat and its intercept value is slightly higher than that of the pure and mixed α-MnO_2 catalysts.

Table 8: Electron-transfer number n via Levich-equation.

Catalyst	**100 rpm**	**400 rpm**	**900 rpm**	**1600 rpm**	**2500 rpm**
$NiCo_2O_4$	2.29	1.65	1.33	1.12	0.94
α - MnO_2-18 g	3.61	3.22	3.02	2.89	2.74
α - MnO_2-10 g	3.52	3.08	2.84	2.67	2.51
18 g + $NiCo_2O_4$; 1:1	3.39	2.97	2.74	2.58	2.39
10 g + $NiCo_2O_4$; 1:1	3.05	2.70	2.52	2.40	2.24
18 g + $NiCo_2O_4$; 1:1 double	3.43	3.03	2.85	2.72	2.58
10 g + $NiCo_2O_4$; 1:1 double	3.43	3.03	2.84	2.69	2.51
18 g + $NiCo_2O_4$; 4:1	3.24	2.81	2.59	2.44	2.28
10 g + $NiCo_2O_4$; 4:1	2.92	2.59	2.42	2.29	2.12

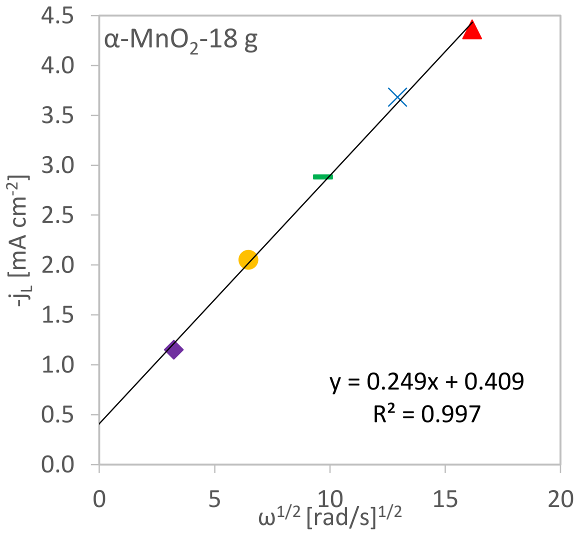

Figure 97: Levich-Plot of α-MnO_2-18 g in 0.1 M KOH at RT.

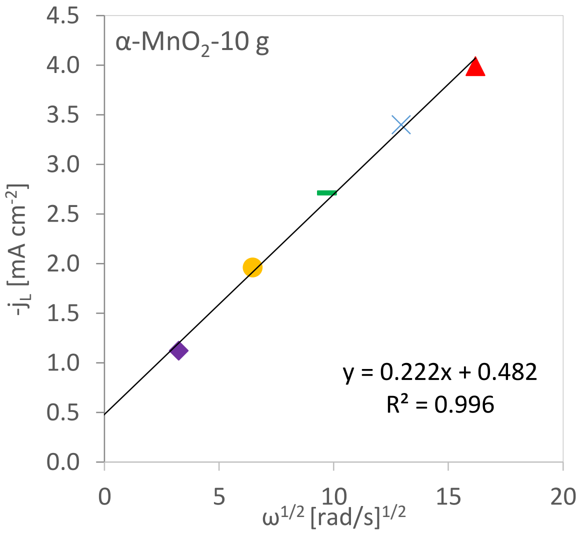

Figure 98: Levich-Plot of α-MnO_2-10 g in 0.1 M KOH at RT.

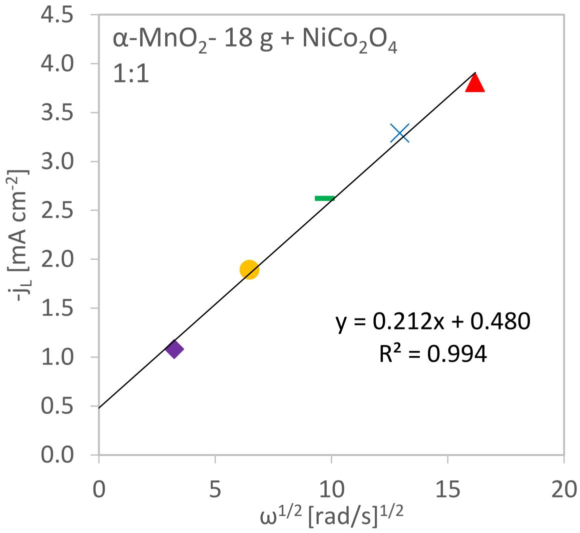

Figure 99: Levich-Plot of α-MnO_2-18 g + $NiCo_2O_4$ (1:1) in 0.1 M KOH at RT.

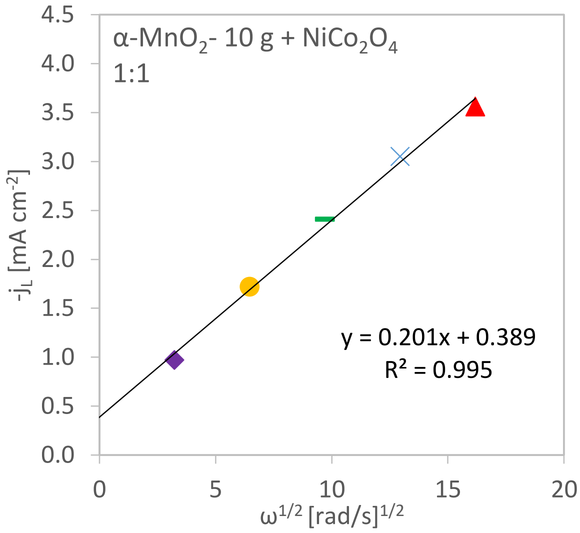

Figure 100: Levich-Plot of α-MnO_2-10 g + $NiCo_2O_4$ (1:1) in 0.1 M KOH at RT.

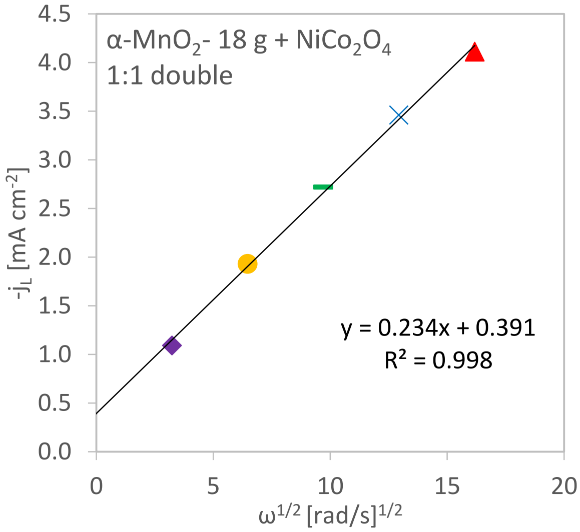

Figure 101: Levich-Plot of α-MnO_2-18 g + $NiCo_2O_4$ (1:1 double) in 0.1 M KOH at RT.

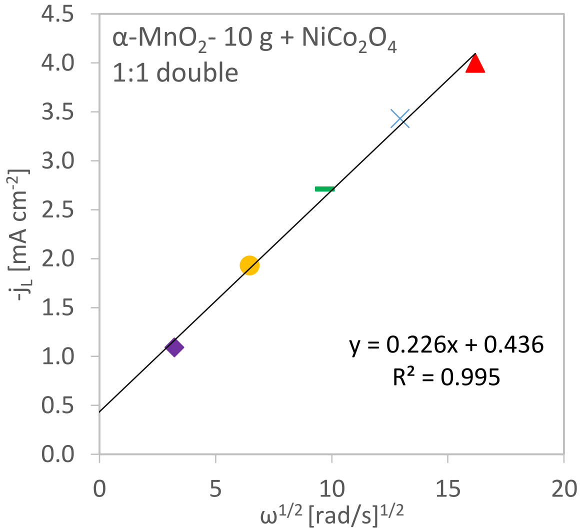

Figure 102: Levich-Plot of α-MnO_2-10 g + $NiCo_2O_4$ (1:1 double) in 0.1 M KOH at RT.

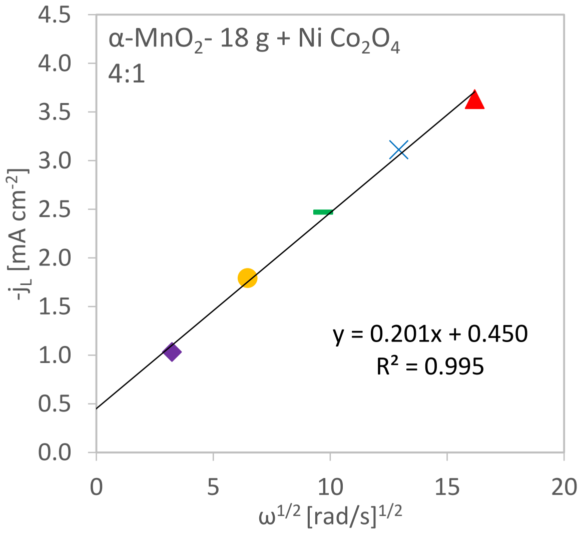

Figure 103: Levich-Plot of α-MnO_2-18 g + $NiCo_2O_4$ (4:1) in 0.1 M KOH at RT.

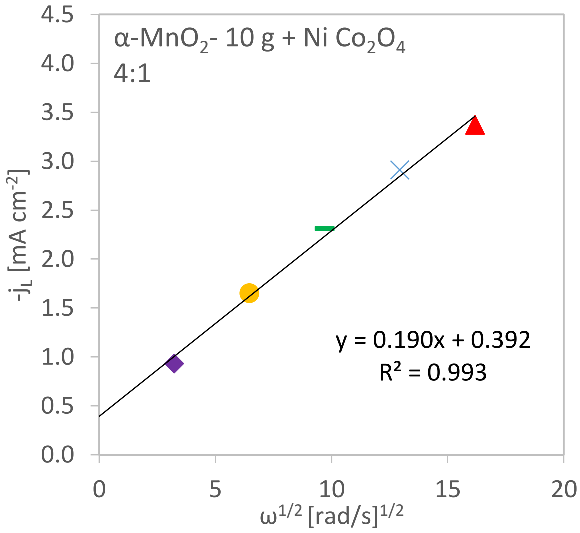

Figure 104: Levich-Plot of α-MnO_2-10 g + $NiCo_2O_4$ (4:1) in 0.1 M KOH at RT.

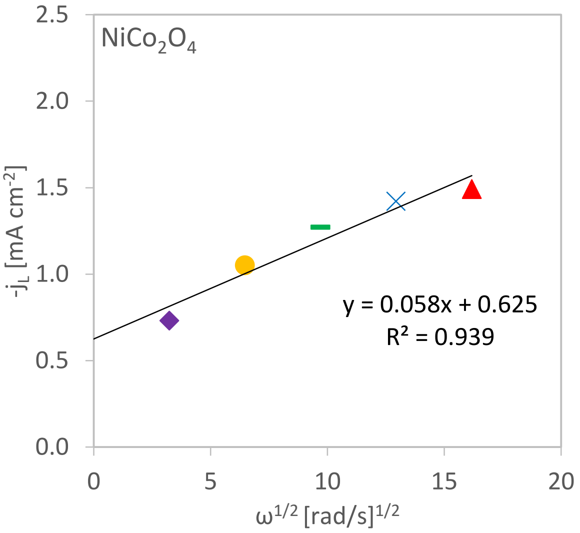

Figure 105: Levich-Plot of $NiCo_2O_4$ in 0.1 M KOH at RT.

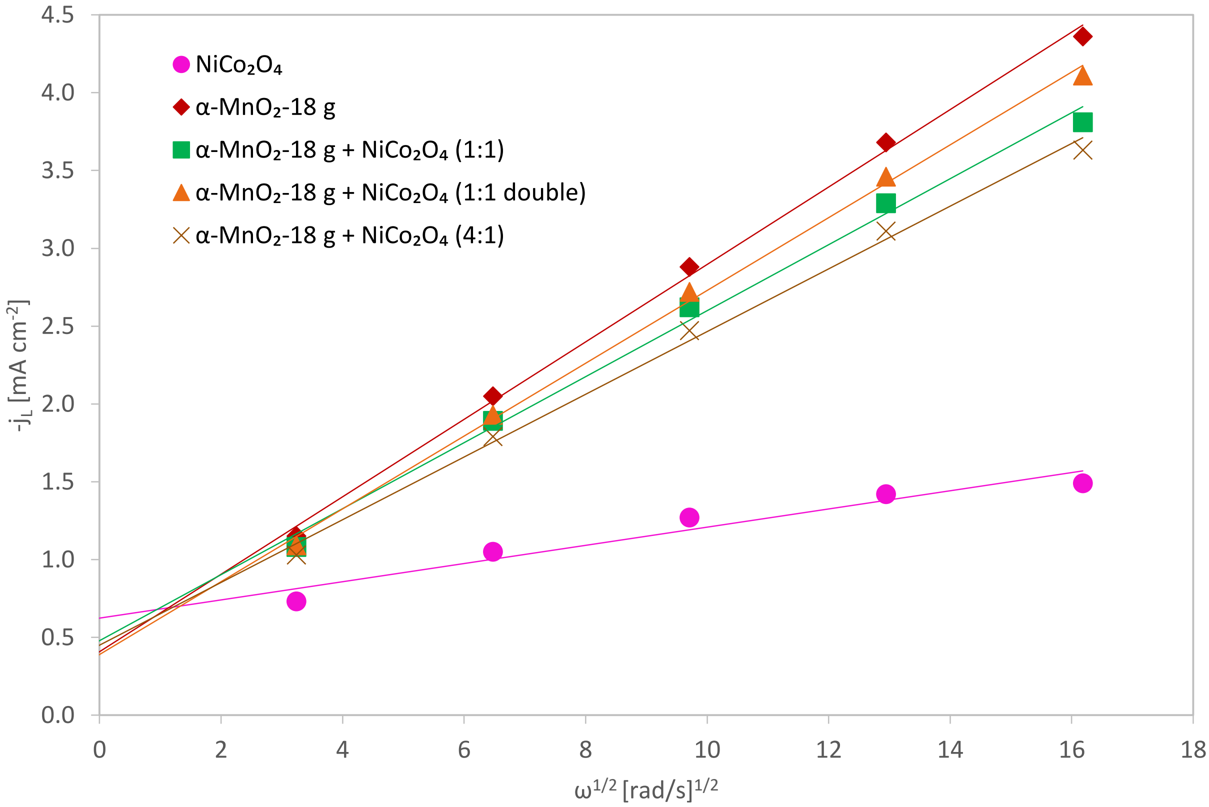

Figure 106: Levich-Plot of $NiCo_2O_4$, α-MnO_2-18 g and the mixed catalysts in 0.1 M KOH at RT.

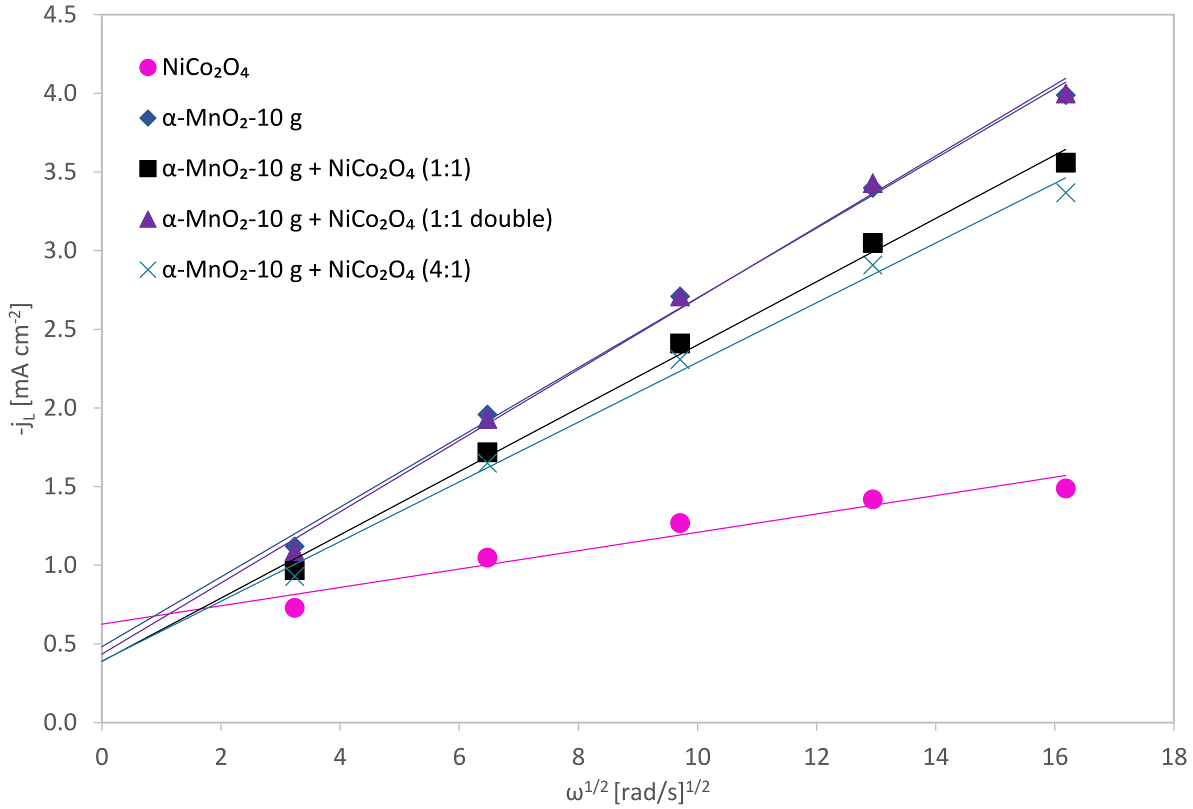

Figure 107: Levich-Plot of $NiCo_2O_4$, α-MnO_2-10 g and the mixed catalysts in 0.1 M KOH at RT.

4.2.5 Koutecky-Levich analysis

Figure 108 to Figure 118 illustrate the Koutecky-Levich plots of each catalyst as well as their comparison. The reciprocal limiting current density of the ORR voltammograms at -0.45 V is plotted against the reciprocal square root of the rotation speed. Straight lines with an intercept not equal to zero are obtained similar to the Levich plots. The number of transferred electrons n during the reduction of oxygen is calculated via the slope according to equation (37) and (38). The results are shown in Table 9, and the n values is between 3.2 and 3.9. The $NiCo_2O_4$ shows a slightly lower n value in comparison to α-MnO_2. The results for the mixed catalysts lie in between these two, with the exception of the mixed 1:1 and 4:1 10 g sample. The transferred electron number of these mixed catalysts is slightly lower compared to the pure $NiCo_2O_4$. The fact that the curves do not intercept zero indicates that the process is kinetically limited. Figure 117 and Figure 118 shows that $NiCo_2O_4$ displays the highest intercept value and therefore, it is more kinetically limited than the samples containing α-MnO_2, which exhibit comparable intercept values.

Table 9: Electron-transfer-number n via slope.

Catalyst	**slope**	**n**
$NiCo_2O_4$	2.849	3,57
α - MnO_2-18 g	2.581	3.94
α - MnO_2-10 g	2.588	3.93
18 g + $NiCo_2O_4$; 1:1	2.681	3,79
10 g + $NiCo_2O_4$; 1:1	3.031	3.35
18 g + $NiCo_2O_4$; 1:1 double	2.717	3.74
10 g + $NiCo_2O_4$; 1:1 double	2.698	3.72
18 g + $NiCo_2O_4$; 4:1	2.803	3.63
10 g + $NiCo_2O_4$; 4:1	3.151	3.23

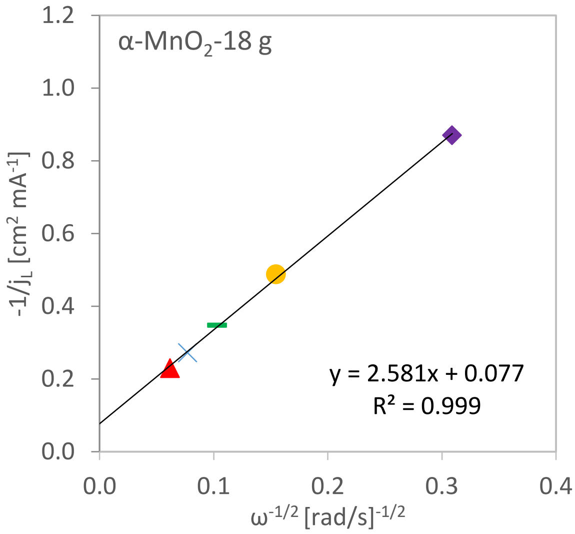

Figure 108: Koutecky-Levich-Plot of α-MnO_2-18 g in 0.1 M KOH at RT.

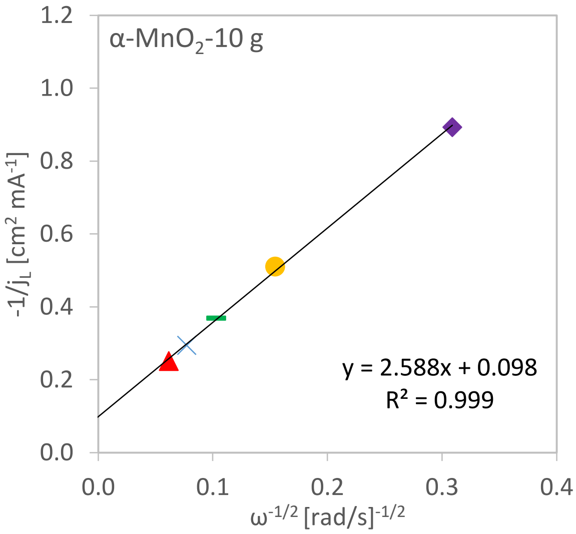

Figure 109: Koutecky-Levich-Plot of α-MnO_2-10 g in 0.1 M KOH at RT.

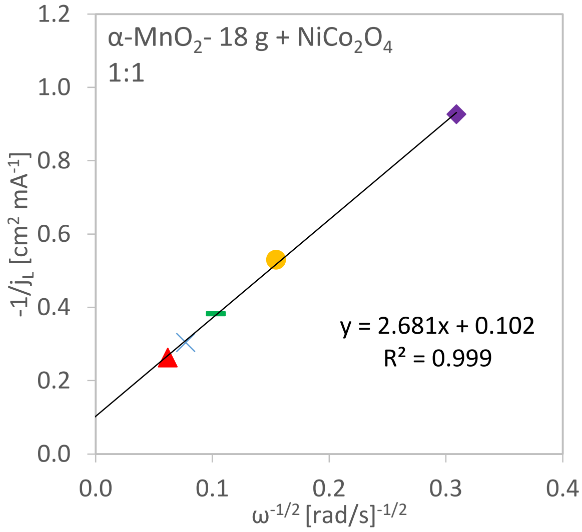

Figure 110: Koutecky-Levich-Plot of α-MnO_2-18 g + $NiCo_2O_4$ (1:1) in 0.1 M KOH at RT.

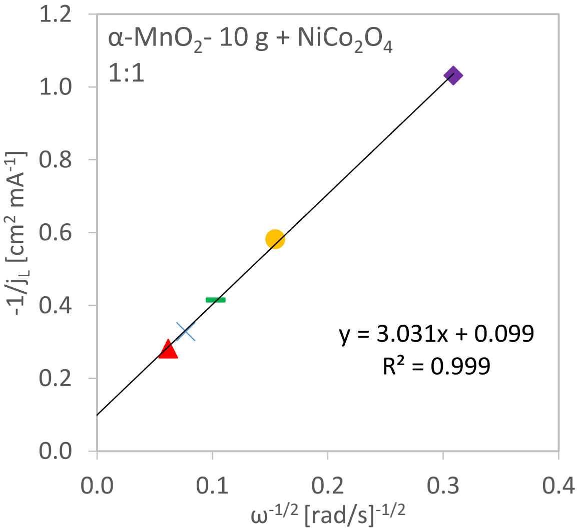

Figure 111: Koutecky-Levich-Plot of α-MnO_2-10 g + $NiCo_2O_4$ (1:1) in 0.1 M KOH at RT.

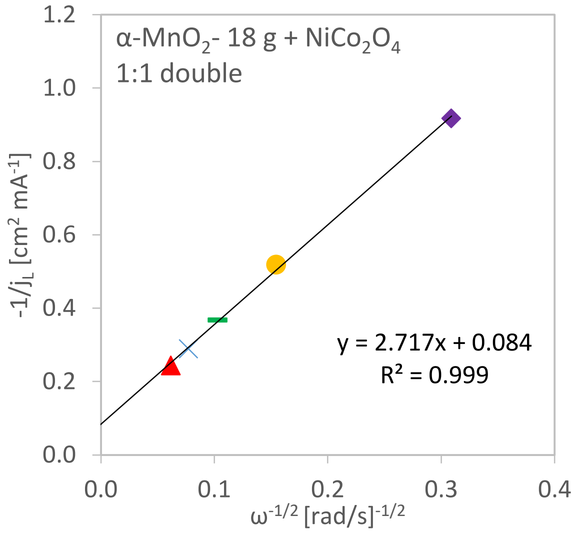

Figure 112: Koutecky-Levich-Plot of α-MnO_2-18 g + $NiCo_2O_4$ (1:1 double) in 0.1 M KOH at RT.

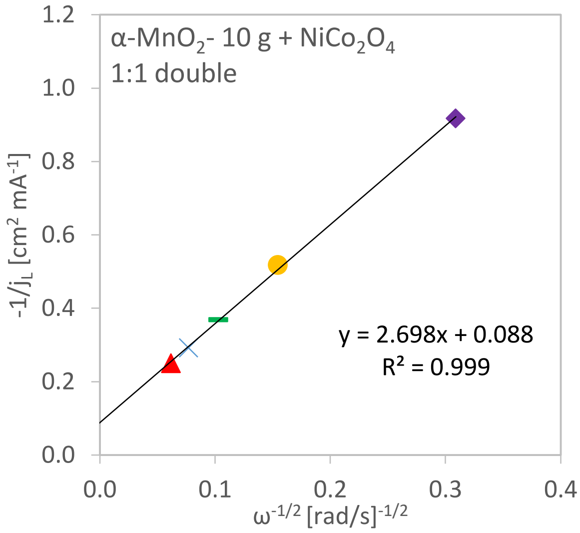

Figure 113: Koutecky-Levich-Plot of α-MnO_2-10 g + $NiCo_2O_4$ (1:1 double) in 0.1 M KOH at RT.

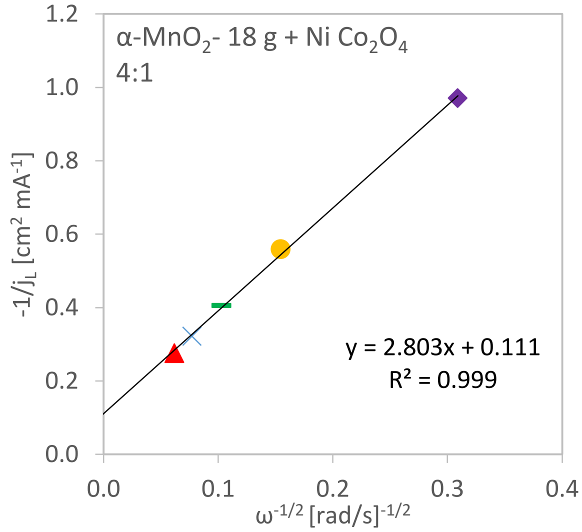

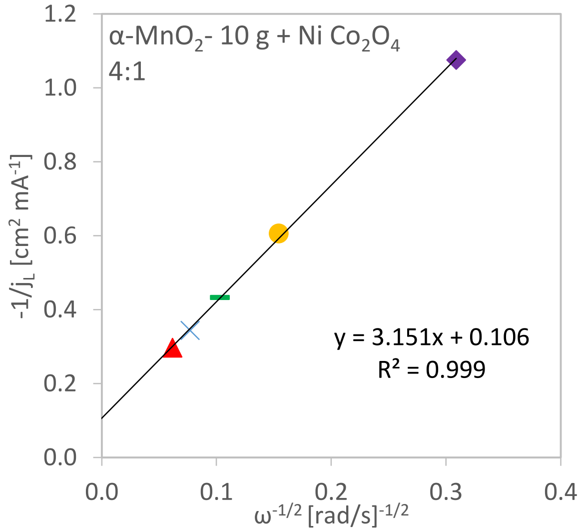

Figure 114: Koutecky-Levich-Plot of α-MnO_2-18 g + $NiCo_2O_4$ (4:1) in 0.1 M KOH at RT.

Figure 115: Koutecky-Levich-Plot of α-MnO_2-10 g + $NiCo_2O_4$ (4:1) in 0.1 M KOH at RT.

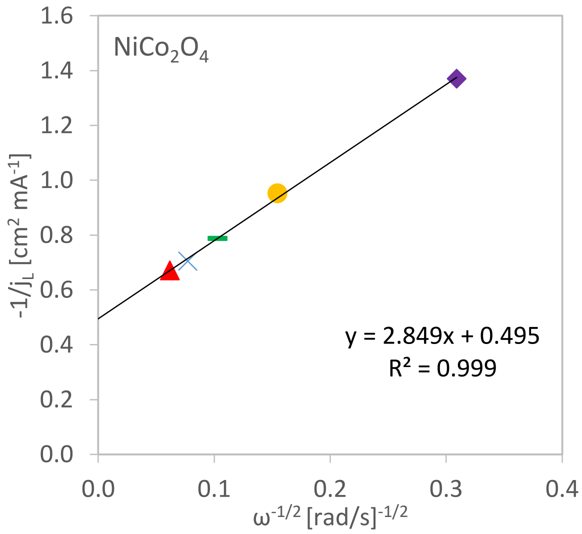

Figure 116: Koutecky-Levich-Plot of $NiCo_2O_4$ in 0.1 M KOH at RT.

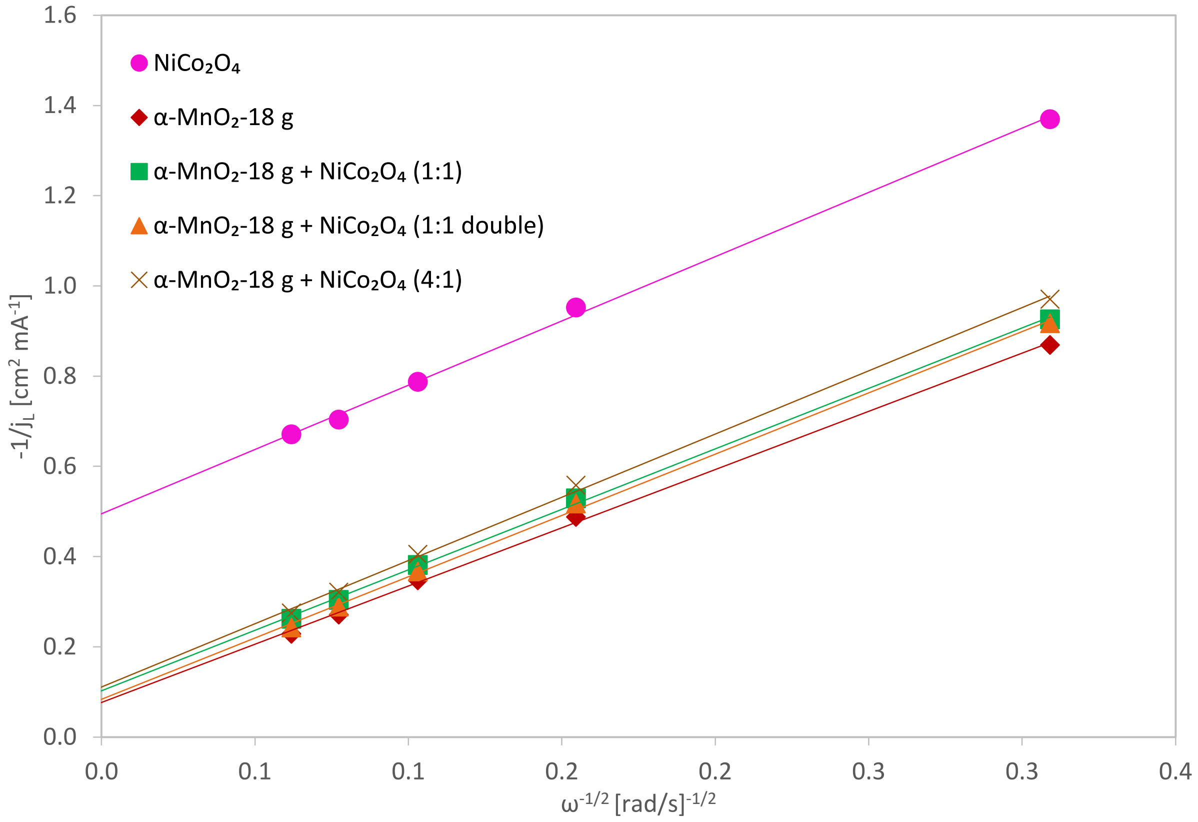

Figure 117: Koutecky-Levich-Plot of $NiCo_2O_4$, α-MnO_2-18 g and the mixed catalysts in 0.1 M KOH at RT.

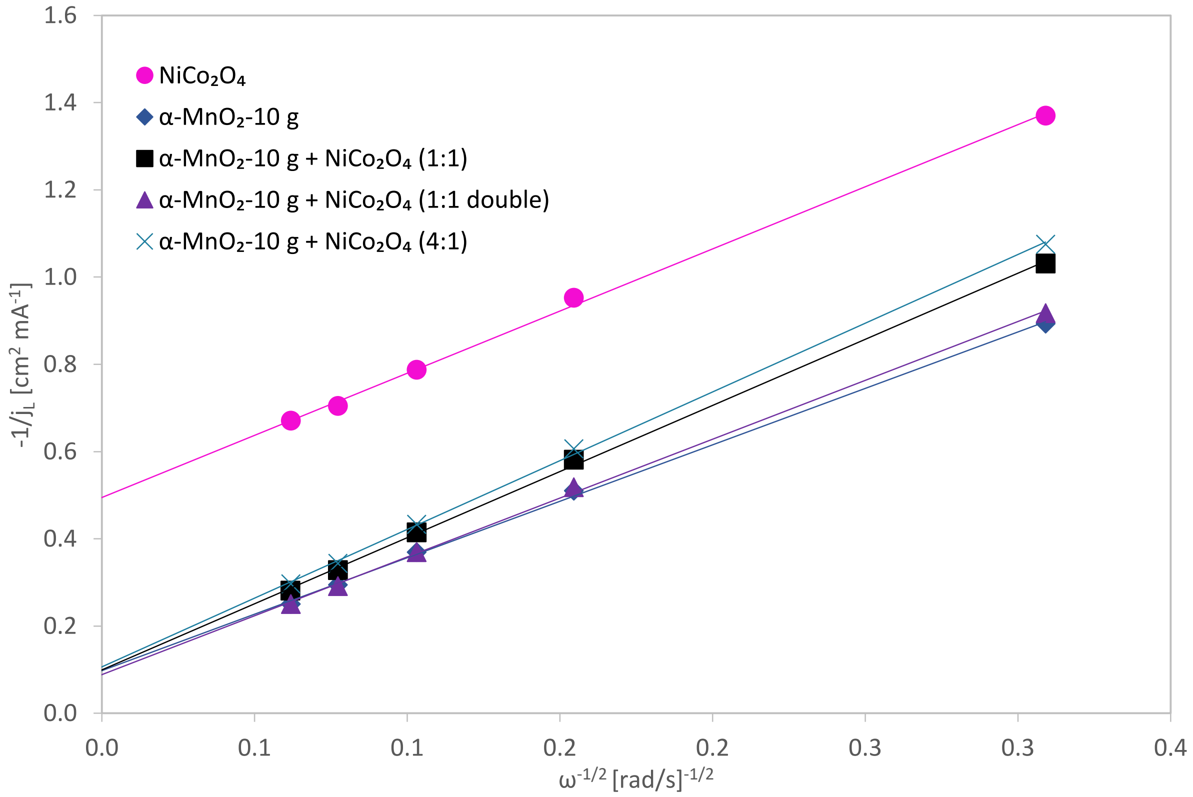

Figure 118: Koutecky-Levich-Plot of $NiCo_2O_4$, α-MnO_2-10 g and the mixed catalysts in 0.1 M KOH at RT.

5 Conclusion

Two different α-MnO_2 samples are for the first time combined with a $NiCo_2O_4$ spinel in different ratios to develop a promising bifunctional catalyst for the air electrode of secondary zinc-air batteries. The electrochemical properties of the pure and mixed samples are examined via cyclic voltammetry (CV), oxygen evolution (OER) and oxygen reduction reaction (ORR) experiments. The measurements are performed in 0.1 M and 8 M KOH using a rotating disc working electrode (RDE) that is covered with the catalyst. The physicochemical properties of the manganese oxides are analysed by XRD, SEM/EDX and BET measurements. The water content is determined by thermal treatment of the samples.

The α-MnO_2 samples are synthesized via acid digestion of Mn_2O_3. Ball-milled electrolytic manganese dioxide (EMD) is heat-treated to obtain Mn_2O_3 that is further converted into two different alpha manganese dioxide types, based on the best working catalyst for OER and ORR in literature (α-MnO_2-10 g and α-MnO_2-18 g). Sulphuric acid and a certain temperature are used for the formation of the α-MnO_2 phase. A $NiCo_2O_4$ spinel sample, synthesized in previous studies, is utilized in this work. It is prepared via hydroxide precipitation method, where nickel and cobalt nitrate hexahydrate salts are dissolved in deionized water, precipitated with sodium hydroxide and calcined.

Rietveld refinement of the XRD patterns shows phase-pure Mn_2O_3 and α-MnO_2 samples and a mixture of γ-MnO_2 and ε-MnO_2 for EMD. The crystallite size of both products is approx. 18 nm. The SEM images of EMD demonstrate much smaller particles after milling. While EMD presents a flaky and porous morphology, Mn_2O_3 has a reef-like surface shape. The α-MnO_2 powders can be categorized as nanorods. EDX measurements confirmed the presence of manganese, oxygen and a small amount of sulphur that is due to sample synthesis. The BET results are in good agreement with literature. The specific surface area and pore volume is drastically reduced after the sintering process of EMD and those of the α-MnO_2 samples are higher than that of Mn_2O_3 and EMD. The 18 g sample displays higher surface area than the 10 g sample, whereas the value of the $NiCo_2O_4$ spinel is slightly smaller. The physically adsorbed water content of α-MnO_2-10 g is twice as high as for α-MnO_2-18 g. The chemically bond water content is nearly the same for both samples. In general, higher

BET-surface area indicates a higher amount of physically adsorbed water. The contrary results in this work can be traced back to desorption during the drying steps.

The CVs of the individual α-MnO_2 and $NiCo_2O_4$ catalysts show several manganese, cobalt and nickel reduction and oxidation peaks. The mixed catalysts display a combination of the oxidation and reduction peaks of the pure α-MnO_2 and $NiCo_2O_4$. In general, the peak current density of the mixed samples increases in the following order: 4:1 < 1:1 < 1:1 double, with the only exception of the mixed α-MnO_2-10 g catalyst in 8 M KOH. In addition, the current density range of the pure $NiCo_2O_4$ spinel is much lower compared to the α-MnO_2 samples. Furthermore, the peak current density is slightly higher in 8 M KOH than in 0.1 M KOH. The catalysts show significantly higher current densities compared to the pure electrode and the one coated with XC-72. Long term stability experiments (100 cycles) result that the peak current density of the pure α-MnO_2 decreases with increasing cycle number indicating low stability. In the case of the pure $NiCo_2O_4$, the reduction peak at ~0.2 V and the oxidation peak at ~0.45 V increase until the 10th cycle. Afterwards, the peak current density slightly decreases and the oxidation peak is shifted anodically. In contrast, the oxidation peak at ~0.25 V continuously decreases with increasing cycle number. The peak current density of the mixed catalysts increases until the 30th cycle and afterwards it decreases.

Considering the OER results, the catalysts exhibit lower overpotential in 8 M KOH than in 0.1 M KOH what can be explained by the higher conductivity and higher OH^- concentration. The overpotential of the catalysts is significantly lower (~800 mV) than that of the pure electrode and the carbon powder XC-72. In 8 M KOH, the results of the pure and mixed α-MnO_2-10 g samples are better than those of the catalysts containing the 18 g sample in the same ratio. The overpotential of $NiCo_2O_4$ is lower than that of the α-MnO_2 samples. The mixed catalysts show improved performance compared to the individual catalysts and the activity increases with the total $NiCo_2O_4$ amount: 4:1 < 1:1 < 1:1 double. In 0.1 M KOH, no clear trend can be noticed.

For the ORR, the catalysts indicate a higher limiting current density in 0.1 M KOH than in 8 M KOH due to higher solubility of oxygen in diluted electrolyte. In 0.1 M KOH, the performance of the pure $NiCo_2O_4$ spinel is not significantly enhanced compared to the pure electrode and the current density is even lower than that of the carbon powder.

The overpotential of $NiCo_2O_4$ is significantly higher (~200 mV) and the limiting current density is only approx. half of that of the pure and mixed α-MnO_2 catalysts. Even though the combination of α-MnO_2 with $NiCo_2O_4$ leads to a slightly decreased current density and slightly higher overpotential compared to the pure α-MnO_2, it significantly increases the electrocatalytic activity in comparison to the pure $NiCo_2O_4$ (α-MnO_2 > 1:1 double > 1:1 > 4:1 >> $NiCo_2O_4$). Additionally, the catalysts containing α-MnO_2-18 g provide better performances than those using the α-MnO_2-10 g sample correlating with a higher specific surface area. The limiting current density of all samples increases with increasing rotation rate that can be explained by a faster oxygen transport to the electrode surface. In 8 M KOH, the catalysts are less stable and the current density decreases with each sweep due to the formation of electrochemical inactive manganese oxides like Mn_3O_4. The current density of the pure α-MnO_2 samples in the fifth sweep is only slightly higher and the overpotential is much higher (~250 mV) compared to the pure electrode and the carbon powder XC-72. The pure $NiCo_2O_4$ spinel exhibits a slightly higher current density and much lower overpotential compared to pure α-MnO_2. The combination of both catalysts further increases the current density depending on the total α-MnO_2 amount: 1:1 < 4:1 < 1:1 double. The overpotential of the mixed catalysts is nearly as high as that of the pure α-MnO_2.

The Levich and Koutecky-Levich plots indicate kinetically limited processes. The Koutecky-Levich analysis yields a number of transferred electrons between 3.2 and 3.9 in the following order: $NiCo_2O_4$ < α-MnO_2/$NiCo_2O_4$ < α-MnO_2, with the exception of the mixed 10 g sample (1:1 and 4:1) presenting the lowest n values.

6 References

[1] Y. Li, M. Gong, Y. Liang, J. Feng, J.E. Kim, H. Wang, G. Hong, B. Zhang, H. Dai, Advanced zinc-air batteries based on high-performance hybrid electrocatalysts, Nat. Commun. 4 (2013) 1805–1807.

[2] A.R. Mainar, O. Leonet, M. Bengoechea, I. Boyano, I. de Meatza, A. Kvasha, A. Guerfi, J.A. Blázquez, Alkaline aqueous electrolytes for secondary zinc-air batteries: an overview, Int. J. Energy Res. 40 (2016) 1032–1049.

[3] M.A. Rahman, X. Wang, C. Wen, High Energy Density Metal-Air Batteries: A Review, J. Electrochem. Soc. 160 (2013) A1759–A1771.

[4] J. Fu, Z.P. Cano, M.G. Park, A. Yu, M. Fowler, Z. Chen, Electrically Rechargeable Zinc–Air Batteries: Progress, Challenges, and Perspectives, Adv. Mater. 29 (2017) 1–34.

[5] V. Caramia, B. Bozzini, Materials science aspects of zinc-air batteries: a review, Mater. Renew. Sustain. Energy. 3 (2014) 1–12.

[6] Z.-L. Wang, D. Xu, J.-J. Xu, X.-B. Zhang, Oxygen electrocatalysts in metal-air batteries: From aqueous to nonaqueous electrolytes, Chem. Soc. Rev. 43 (2014) 7746–7786.

[7] M.S. Guney, Y. Tepe, Classification and assessment of energy storage systems, Renew. Sustain. Energy Rev. 75 (2017) 1187–1197.

[8] C. Liu, F. Li, L.-P. Ma, H.-M. Cheng, Advanced Materials for Energy Storage, Adv. Energy Mater. 22 (2010) E28–E62.

[9] P. Pei, K. Wang, Z. Ma, Technologies for extending zinc-air battery's cyclelife: A review, Appl. Energy. 128 (2014) 315–324.

[10] S. Müller, F. Holzer, O. Haas, Optimized zinc electrode for the rechargeable zinc-air battery, J. Appl. Electrochem. 28 (1998) 895–898.

[11] D.U. Lee, J.-Y. Choi, K. Feng, H.W. Park, Z. Chen, Advanced extremely durable 3D bifunctional air electrodes for rechargeable zinc-air batteries, Adv. Energy Mater. 4 (2014) 1–5.

[12] R.B. Valim, M.C. Santos, M.R.V. Lanza, S.A.S. Machado, F.H.B. Lima, M.L. Calegaro, Oxygen reduction reaction catalyzed by ε-MnO2: Influence of the crystalline structure on the reaction mechanism, Electrochim. Acta. 85 (2012) 423–431.

[13] P.-C. Li, C.-C. Hu, H. Noda, H. Habazaki, Synthesis and characterization of carbon black/manganese oxide air cathodes for zinc-air batteries: Effects of the crystalline structure of manganese oxides, J. Power Sources. 298 (2015) 102–113.

[14] A.R. Mainar, L.C. Colmenares, O. Leonet, F. Alcaide, J.J. Iruin, S. Weinberger, V. Hacker, E. Iruin, I. Urdanpilleta, J.A. Blazquez, Manganese oxide catalysts for secondary zinc air batteries: from electrocatalytic activity to bifunctional air electrode performance, Electrochim. Acta. 217 (2016) 80–91.

[15] B. Krenn, Bifunctional NiCo2O4-spinel as catalyst for rechargeable zinc-air redox flow batteries in alkaline and neutral media, Graz University of Technology, 2017.

[16] A.R. Mainar, E. Iruin, L.C. Colmenares, A. Kvasha, I. de Meatza, M. Bengoechea, O. Leonet, I. Boyano, Z. Zhang, J.A. Blazquez, An overview of progress in electrolytes for secondary zinc-air batteries and other storage systems based on zinc, J. Energy Storage. 15 (2018) 304–328.

[17] Y. Li, J. Lu, Metal-Air Batteries: Will They Be the Future Electrochemical Energy Storage Device of Choice?, ACS Energy Lett. 2 (2017) 1370–1377.

[18] J.-S. Lee, S.T. Kim, R. Cao, N.-S. Choi, M. Liu, K.T. Lee, J. Cho, Metal-air batteries with high energy density: Li-air versus Zn-air, Adv. Energy Mater. 1 (2011) 34–50.

[19] F. Cheng, J. Chen, Metal-air batteries: From oxygen reduction electrochemistry to cathode catalysts, Chem. Soc. Rev. 41 (2012) 2172–2192.

[20] D. Linden, T.B. Reddy, eds., Linden’s Handbook of batteries, 4th ed., McGraw-Hill, New York, 2011.

[21] Y. Li, H. Dai, Recent advances in zinc-air batteries, Chem. Soc. Rev. 43 (2014) 5257–5275.

[22] O. Haas, J. Van Wesemeal, Zinc-air: Electrical Recharge, in: Jürgen Garche et al., Encycl. Electrochem. Power Sources. 4 (2009) 384–392.

[23] M. Prabu, K. Ketpang, S. Shanmugam, Hierarchical nanostructured NiCo2O4 as an efficient bifunctional non-precious metal catalyst for rechargeable zinc-air batteries, R. Soc. Chem. Nanoscale. 6 (2014) 3173–3181.

[24] Inorganic Crystal Structure Database (ICSD) des FIZ Karlsruhe, (2018). https://icsd.fiz-karlsruhe.de/ (accessed May 2, 2018).

[25] K.E. Sickafus, J.M. Wills, N.W. Grimes, Structure of Spinel, J. Am. Ceram. Soc. 82 (1999) 3279–3292.

[26] J.-G. Kim, D.L. Pugmire, D. Battaglia, M.A. Langell, Analysis of the NiCo2O4 spinel surface with Auger and X-ray photoelectron spectroscopy, Appl. Surf. Sci. 165 (2000) 70–84.

[27] E.J. Verwey, P.W. Haayman, Physical properties and cation arrangement of oxides with spinel structures I. Cation Arrangement in Spinels, J. Chem. Phys. 15 (1947) 174–180.

[28] M. Binnewies, M. Finze, M. Jäckel, P. Schmidt, H. Willner, G. Rayner-Canham, Allgemeine und Anorganische Chemie, 3rd ed., Springer Spektrum, Berlin, Heidelberg, 2016.

[29] S.Y. Tsai, C.T. Ni, K.Z. Fung, Characterization of infrared transmittance in mixed transition metal oxides for solar cells application, Ceram. Int. 43 (2017) S460–S463.

[30] Y. Noda, K. Ohno, S. Nakamura, Momentum-dependent band spin splitting in semiconducting MnO2: A density functional calculation, Phys. Chem. Chem. Phys. 18 (2016) 13294–13303.

[31] F. Cheng, Y. Su, J. Liang, Z. Tao, J. Chen, MnO2-based nanostructures as catalysts for electrochemical oxygen reduction in alkaline media, Chem. Mater. 22 (2010) 898–905.

[32] B. Yin, S. Zhang, H. Jiang, F. Qu, X. Wu, Phase-controlled synthesis of polymorphic MnO2 structures for electrochemical energy storage, J. Mater. Chem. A. 3 (2015) 5722–5729.

[33] Y. Tang, S. Zheng, Y. Xu, X. Xiao, H. Xue, H. Pang, Advanced batteries based on manganese dioxide and its composites, Energy Storage Mater. 12 (2018) 284–309.

[34] X. Wang, Y. Li, Rational synthesis of alpha-MnO2 single-crystal nanorods, Chem. Commun. (2002) 764–765.

[35] W. Wei, X. Cui, W. Chen, D.G. Ivey, Manganese oxide-based materials as electrochemical supercapacitor electrodes, Chem. Soc. Rev. 40 (2011) 1697–1721.

[36] Y. Duan, H. Jing, Z. Liu, S. Li, G. Ma, Controlled synthesis and electromagnetic performance of hollow microstructures assembled of tetragonal MnO2 nano-columns, J. Appl. Phys. 111 (2012) 1–8.

[37] P. Ruetschi, Cation Vacancies in MnO2 and Their Influence on Electrochemical Reactivity, J. Electrochem. Soc. 135 (1988) 2663–2669.

[38] D.K. Walanda, G.A. Lawrance, S.W. Donne, Hydrothermal MnO2: Synthesis, structure, morphology and discharge performance, J. Power Sources. 139 (2005) 325–341.

[39] D.K. Walanda, Kinetics and morphology transformation of manganese oxide in acid electrolyte, Proceeding Int. Semin. Chem. (2008) 180–184.

[40] D.K. Walanda, G.A. Lawrance, S.W. Donne, Kinetics of Mn2O3 digestion in H2SO4 solutions, J. Solid State Chem. 182 (2009) 1336–1342.

[41] W. Massa, Kristallstrukturbestimmung, 8th ed., Springer Spektrum, Wiesbaden, 2015.

[42] R.E. Dinnebier, S.J.L. Billinge, Powder diffraction: Theory and practice, RSC Publishing, Cambridge, 2008.

[43] G. Hübschen, I. Altpeter, R. Tschunky, H.-G. Hermann, eds., Materials and Characterization Using Nondestructive Evaluation (NDE), Woodhead Publishing, Cambridge, 2016.

[44] S. V. Dorozhkin, Amorphous Calcium Orthophosphates: Nature, Chemistry and Biomedical Applications, Int. J. Mater. Chem. 2 (2012) 19–46.

[45] V.S. Ramachandram, J.J. Beaudoin, eds., Handbook of analytical techniques in concrete science and technology; Principles, Techniques and Applications, William Andrew Publishing/Noyes Publications, New York, 2001.

[46] M. de A. Pereira-da-Silva, F.A. Ferri, Chapter 1: Scanning Electron Microscopy, in: O.J. Novais de Oliveira, M. Ferreira, F. de Lima Leite, A.L. Da Róz (Eds.), Nanocharacterization Tech., William Andrew Publishing, 2017: pp. 1–35.

[47] S. Henning, R. Adhikari, Chapter 1: Scanning Electron Microscopy, ESEM, and X-ray Microanalysis, in: T. Sabu, T. Raju, Z.K. Ajesh, M. K. Raghvendra (Eds.), Microsc. Methods Nanomater. Charact., Elsevier, 2017: pp. 1–30.

[48] Y.X. Zhang, S. Zhu, M. Dong, C.P. Liu, Z.Q. Wen, Hydrothermally tailoring low-dimensional MnOx nanostructure and their high electrochemical performance, Int. J. Electrochem. Sci. 8 (2013) 2407–2416.

[49] M. Naderi, Chapter 14: Surface Area : Brunauer – Emmett – Teller (BET), in: S. Tarleton, Prog. Filtr. Sep., Academic Press, Oxford, 2015: pp. 585–608.

[50] K.S.W. Sing, D.H. Everett, R.A.W. Haul, L. Moscou, R.A. Pierotti, J. Rouquerol, T. Siemieniewska, Reporting physisorption data for gas/solid systems with special reference to the determination of surface area and porosity, Pure Appl. Chem. 57 (1985) 603–619.

[51] S. Brunauer, P.H. Emmett, E. Teller, Adsorption of Gases in Multimolecular Layers, J. Am. Chem. Soc. 60 (1938) 309–319.

[52] M. Thommes, K. Kaneko, A. V. Neimark, J.P. Olivier, F. Rodriguez-Reinoso, J. Rouquerol, K.S.W. Sing, Physisorption of gases, with special reference to the evaluation of surface area and pore size distribution (IUPAC Technical Report), Pure Appl. Chem. 87 (2015) 1051–1069.

[53] S. Storck, H. Bretinger, W.F. Maier, Characterization of micro- and mesoporous solids by physisorption methods and pore-size analysis, Appl. Catal. A Gen. 174 (1998) 137–146.

[54] J. Rouquerol, D. Avnir, C.W. Fairbridge, D.H. Everett, J.H. Haynes, N. Pernicone, J.D.F. Ramsay, K.S.W. Sing, K.K. Unger, Recommendations for the characterization of porous solids, Pure Appl. Chem. 66 (1994) 1739–1758.

[55] E.P. Barrett, L.G. Joyner, P.P. Halenda, The Determination of Pore Volume and Area Distributions in Porous Substances. I. Computations from Nitrogen Isotherms, J. Am. Chem. Soc. 73 (1951) 373–380.

[56] Belsorp, User's Manual (BELMasterTM/BELsimTM) Ver.2.3.1, Chapter 18: BJH plot, 2014.

[57] P. Ruetschi, Cation-Vacancy Model for Mn02, J. Electrochem. Soc. 131 (1984) 2737–2744.

[58] S.B. Kanungo, Physicochemical properties of MnO2 and MnO2-CuO and their relationship with the catalytic activity for H2O2 decomposition and CO oxidation, J. Catal. 58 (1979) 419–435.

[59] C. de A. Dias, H. de Santana, M.A.L. Nobre, M.C. Lopes, The relation between structural features and electrochemical activity of MnO2 nanoparticles synthesized from a polyol-made Mn3O4 precursor, J. Solid State Electrochem. 17 (2013) 1967–1976.

[60] P. Ruetschi, Influence of Cation Vacancies on the Electrode Potential of MnO2, J. Solid State Electrochem. 135 (1988) 2658–2663.

[61] Southampton Electrochemistry Group, Instrumental Methods in Electrochemistry, Woodhead Publishing, Cambridge, 2001.

[62] N. Elgrishi, K.J. Rountree, B.D. McCarthy, E.S. Rountree, T.T. Eisenhart, J.L. Dempsey, A Practical Beginner's Guide to Cyclic Voltammetry, J. Chem. Educ. (2017) A-J.

[63] J. Wang, Analytical Electrochemistry, 3rd ed., Wiley-VCH, New Jersey, 2006.

[64] A.J. Bard, L.R. Faulkner, Electrochemical Methods: Fundamentals and Applications, 2nd ed., Wiley-VCH, 2001.

[65] S.-J. Lee, S. Pyun, S.-K. Lee, S.-J.L. Kang, Fundamentals of Rotating Disc and Ring-Disc Electrode Techniques and their Applications to Study the Oxygen Reduction Mechanism at Pt/C Electrode for Fuel Cells, Isr. J. Chem. 48 (2008) 215–228.

[66] J. Nikolic, E. Expósito, J. Iniesta, J. González-García, V. Montiel, Theoretical Concepts and Applications of a Rotating Disk Electrode, J. Chem. Educ. 77 (2000) 1191–1194.

[67] Pine Reasearch Instrumentation, Modulated Speed Rotator (MSR) User Guide, (2013) 126–140.

[68] C. Dua, Q. Tana, G. Yina, J. Zhang, Rotating Disk Electrode Method, in: Rotating Electrode Methods Oxyg. Reduct. Electrocatal., Elsevier B.V., 2014: pp. 171–198.

[69] E.L. Gyenge, J.-F. Drillet, The Electrochemical Behavior and Catalytic Activity for Oxygen Reduction of MnO2⁄C–Toray Gas Diffusion Electrodes, J. Electrochem. Soc. 159 (2012) F23–F34.

[70] S.R.S. Prabaharan, T. Nathan, M. Cloke, Electrode properties of Mn2O3 nanospheres synthesized by combined sonochemical/solvothermal method for use in electrochemical capacitors, J. Nanomater. 2008 (2008) 1–8.

[71] Y. Park, S. Woo Lee, K.H. Kim, B.K. Min, A. Kumar Nayak, D. Pradhan, Y. Sohn, Understanding hydrothermal transformation from Mn2O3 particles to Na0.55Mn2O4·1.5H2O nanosheets, nanobelts, and single crystalline ultra-long Na4Mn9O18 nanowires, Sci. Rep. 5 (2015) 1–11.

[72] F. Wang, H. Dai, J. Deng, G. Bai, K. Ji, Y. Liu, Manganese oxides with rod-, wire-, tube-, and flower-like morphologies: Highly effective catalysts for the removal of toluene, Environ. Sci. Technol. 46 (2012) 4034–4041.

[73] K. Selvakumar, S.M. Senthil Kumar, R. Thangamuthu, K. Ganesan, P. Murugan, P. Rajput, S.N. Jha, D. Bhattacharyya, Physiochemical Investigation of Shape-Designed MnO2 Nanostructures and Their Influence on Oxygen Reduction Reaction Activity in Alkaline Solution, J. Phys. Chem. C. 119 (2015) 6604–6618.

[74] Y. Meng, W. Song, H. Huang, Z. Ren, S.-Y. Chen, S.L. Suib, Structure–Property Relationship of Bifunctional MnO2 Nanostructures: Highly Efficient, Ultra-Stable Electrochemical Water Oxidation and Oxygen Reduction Reaction Catalysts Identified in Alkaline Media, J. Am. Chem. Soc. 136 (2014) 11452–11464.

[75] S. Devaraj, N. Munichandraiah, Effect of crystallographic structure of MnO2 on its electrochemical capacitance properties, J. Phys. Chem. C. 112 (2008) 4406–4417.

[76] F.H.B. Lima, M.L. Calegaro, E.A. Ticianelli, Electrocatalytic activity of manganese oxides prepared by thermal decomposition for oxygen reduction, Electrochim. Acta. 52 (2007) 3732–3738.

[77] F.H.B. Lima, M.L. Calegaro, E.A. Ticianelli, Investigations of the catalytic properties of manganese oxides for the oxygen reduction reaction in alkaline media, J. Electroanal. Chem. 590 (2006) 152–160.

[78] M.L. Calegaro, F.H.B. Lima, E.A. Ticianelli, Oxygen reduction reaction on nanosized manganese oxide particles dispersed on carbon in alkaline solutions, J. Power Sources. 158 (2006) 735–739.

[79] J. Mcbreen, The Electrochemistry of beta-Mn02 and gamma-MnO2 in alkaline electrolyte, Electrochim. Acta. 20 (1975) 221–225.

[80] P. Rasiyah, A.C.C. Tseung, A Mechanistic Study of Oxygen Evolution on NiCo2O4, J. Electrochem. Soc. 129 (1982) 1724–1727.

[81] J. Haenen, W. Visscher, E. Barendrecht, O2 Evolution on Nickel-Cobalt Alloys, Electrochim. Acta. 31 (1986) 1541–1551.

[82] E. Castro, C.A. Gervasi, Electrodeposited Ni–Co-oxide electrodes:characterization and kinetics of the oxygen evolution reaction, Int. J. Hydrogen Energy. 25 (2000) 1163–1170.

[83] A.C. Tavares, M.A.M. Cartaxo, M.I. da S.P. Á, F.M. Costa, Electrochemical study of spinel oxide systems with nominal compositions Ni1-xCuxCo2O4and NiCo2-yCuyO4, J. Solid State Electrochem. 5 (2001) 57–67.

[84] F. Si, Y. Zhang, L. Yan, J. Zhu, M. Xiao, C. Liu, W. Xing, J. Zhang, Electrochemical Oxygen Reduction Reaction, in: Rotating Electrode Methods Oxyg. Reduct. Electrocatal., Elsevier B.V., 2014: pp. 133–170.

[85] P.H. Benhangi, A. Alfantazi, E. Gyenge, Manganese Dioxide-based bifunctional oxygen reduction/evolution electrocatalysts: Effect of perovskite doping and potassium ion insertion, Electrochim. Acta. 123 (2014) 42–50.

[86] H. Malankar, S.S. Umare, K. Singh, M. Sharma, Chemical composition and discharge characteristics of γ-MnO2 prepared using manganese ore, J. Solid State Electrochem. 14 (2010) 71–82.

[87] W. Jin, H. Du, S. Zheng, H. Xu, Y. Zhang, Comparison of the oxygen reduction reaction between NaOH and KOH solutions on a Pt electrode: The electrolyte-dependent effect, J. Phys. Chem. B. 114 (2010) 6542–6548.

[88] J. Qiao, L. Xu, L. Ding, P. Shi, L. Zhang, R. Baker, J. Zhang, Effect of KOH concentration on the oxygen reduction kinetics catalyzed by heat-treated co-pyridine/C electrocatalysts, Int. J. Electrochem. Sci. 8 (2013) 1189–1208.

[89] W.-Y. Yan, S.-L. Zheng, W. Jin, Z. Peng, S.-N. Wang, H. Du, Y. Zhang, The influence of KOH concentration, oxygen partial pressure and temperature on the oxygen reduction reaction at Pt electrodes, J. Electroanal. Chem. 741 (2015) 100–108.

7 Chemicals

Sulphuric acid (H_2SO_4)
≥ 95 % p.a.
Carl Roth GmbH & Co. KG
Art.-Nr.: 4623.1; CAS-Nr.: 7664-93-9

Ethanol (EtOH)
96 % denaturated with 1 % MEK
VWR Chemicals
Art-Nr.: 84106.360; CAS-Nr.: 64-17-5

Propanol-2 (Isopropanol)
≥ 99.8 % p.a.
Chem-Lab NV
Art-Nr.: CL00.0906.2500; CAS-Nr.: 67-63-0

Potassium Hydroxide (KOH)
≥ 85 % p.a.
Carl Roth GmbH & Co. KG
Art-Nr.: 6781.5; CAS-Nr.: 1310-58-3

Nafion®, perfluorinated resin, aqueous dispersion
10 wt% in H_2O
Aldrich Chemistry
Art.-Nr.: 527114-25ML; CAS-Nr.: 31175-20-9

Carbon Black (VXC72R)
CARBOT
CAS-Nr.: 1333-86-4

Electrolytic manganese dioxide (EMD)
Tosoh Corp., Japan

8 List of symbols and abbreviations

AE	Auger electrons
BJH	Barret-Joyner-Halenda
BET	Brunauer-Emmett-Teller
BSE	Backscattered electrons
CNT	Carbon nanotubes
CV	Cyclic voltammetry
EDX	Energy dispersive X-ray spectroscopy
EMD	Electrolytic mananese dioxide
fcc	Face centered cubic
GC	Glassy carbon
GDL	Gas diffusion layer
Hg/HgO	Mercury/Mercury oxide electrode
H_2O_{St}	Structural water
H_2O_{Su}	Surface water
ICSD	Inorganic Crystal Structure Database
IR	Infrared
IUPAC	International Union of Pure and Applied Chemistry
LSV	Linear sweep voltammetry
n	Transferred electrons
OER	Oxygen evolution reaction
ORR	Oxygen reduction reaction
PE	Polyethylene, primary electrons
PP	Polypropylene
PVC	Polyvinylchloride
RDE	Rotating disc electrode
REM	Rasterelektronenmikroskopie
RHE	Reversible hydrogen electrode
RT	Room temperature
RPM	Resolutions per minute
SE	Secondary electrons
SEM	Scanning electron microscopy
SSA	Specific surface area
STP	Standard temperature and pressure
ΔV	Overpotential
XRD	X-ray diffraction

9 List of figures

10 List of tables